RICE UNIVERSITY

Synthesis and Characterization of Two Component Alloy Nanoparticles

by

Salomeh Tabatabaei

A THESIS SUBMITTED
IN PARTIAL FULFILLMENT OF THE
REQUIRMENTS FOR THE DEGREE

Doctor of Philosophy

APPROVED, THESIS COMMITTEE:

PULICKEL M. AJAYAN
BENJAMIN M. AND MARY GREENWOOD ANDERSON
PROFESSOR IN ENGINEERING

PEDRO J. ALVAREZ
GEORGE R. BROWN PROFESSOR OF ENGINEERING
CIVIL AND ENVIRONMENTAL ENGINEERING

ENRIQUE V. BARERRA
PROFESSOR IN MATERIAL SCIENCE

YILDIZ BAYAZITOGLU
HARRY S. CAMERON CHAIR
PROFESSOR IN MECHANICAL ENGINEERING

HOUSTON, TEXAS
JUNE 2010

ABSTRACT

Synthesis and Characterization of Two Component Alloy Nanoparticles

By

Salomeh Tabatabaei

Alloying is an old trick used to produce new materials by synergistically combining at least two components. New developments in nanoscience have enabled new degrees of freedom, such as size, solubility and concentration of the alloying element to be utilized in the design of the physical properties of alloy nanoparticles (ANPs). ANPs as multi-functional materials have applications in catalysis, biomedical technologies and electronics. Phase diagrams of ANPs are very little known and may not represent that of bulk picture, furthermore, ANPs with different crystallite orientation and compositions could remain far from equilibrium. Here, we studied the synthesis and stability of Au-Sn and Ag-Ni ANPs with chemical reduction method at room temperature.

Due to the large difference in the redox potentials of Au and Sn, co-reduction is not a reproducible method. However, two step successive reductions was found to be more reliable to generate Au-Sn ANPs which consists of forming clusters in the first step (either without capping agent or with weakly coordinated surfactant molecules) and then undergoing a second reduction step in the presence of another metal salt. Our observation also showed that capping agents (Cetrimonium bromide or (CTAB)) and Polyacrylic acid (PAA)) play a key role in the alloying process and shorter length capping agent (PAA)

may facilitate the diffusion of individual components and thus enabling better alloying. Different molar ratios of Sn and Au precursors were used to study the effect of alloying elements on the melting point and the crystalline structures and melting points were determined by various microscopy and spectroscopy techniques and differential scanning calorimetry (DSC). A significant depression (up to150^{o}C) in the melting transition was observed for the Au-Sn ANPs compared to the bulk eutectic point (T_m= 280°C) due to the size and shape effect. Au-Sn ANPs offer a unique set of advantages as lead-free solder material which can reflow at lower temperatures leading to lower thermal stresses in adjacent electronic components during the manufacturing process, offering better thermal and mechanical properties suitable for high temperature electronic applications.

The second system studied here is Ag-Ni ANPs and electron microscopy and spectroscopy confirm the formation of $Ag_{0.5}Ni_{0.5}$ ANPs with cubic structure, stable up to125°C. Atomic size and crystalline structure have less effect on the alloy formation process at the nanoscale; therefore, metals with limited solubility in bulk could form solid solutions at the nanoscale. Ag and Ni are immiscible in both solid and liquid states due to the large lattice mismatch and thermodynamically, the formation of core-shell structures is favoured. The effect of capping agents on the alloying was also studied here. Polyvinyl alcohol (PVA) with shorter length shows Ag-Ni ANPs with higher content of Ni compared to sodium citrate; the systems lead to the formation of Ag, Ag_2O_2 and $Ag_{0.5}Ni_{0.5}$ ANPs. The study of multi-component nanoparticle systems could shed light into the various parameters that affect stability of structure and phases, which could be quite distinct from their bulk counterparts.

AKNOLEGMENTS

I would like to express my sincere gratitude to my advisor, Prof. Pulickel Ajayan for his friendship, guidance, inspiration and financial support throughout the course of this research. He always encouraged me to work hard and at the same time balance it with my life; also gave me the freedom to direct my progress. I would also like to extend my gratitude to Prof. Yildiz Bayazitoglu, Prof. Alvarz, and Prof. Enrique Barerra for serving on my Ph.D. committee as well as providing important instructions and recommendations. I very appreciate the helps from the faculty and staff members in department of Mechanical Engineering and Materials Science, Shared Authority Equipment and Smalley Institute.

My special thanks go to my fellow co-workers Dr. Haleh Ardebili and Dr. Ashvani Kumar who have been working with me on my research projects, providing me invaluable suggestions and helps. Also, Haleh always has advised me to be ready for professional life. I also received discussions and helps from Dr. Robert Vajtai, Dr. Peter Loos. I would like to acknowledge Dr. Wenhua Guo for their helps on the high resolution transmission electron microscopy training and image analysis and Richard Crouse for especial helps in X-Ray Diffraction characterization.

Finally, I would like to thank my friends and family for their continuous support and encouragement throughout my education especially my mother that without her support coming this long was not possible.

Table of Contents

List of Tables and Figures

Tables

Figures

Chapter1

1.1 Introduction

1.1.1 Clusters and Nanoparticles (NPs)

Nanoparticles or clusters are aggregates of a few or many millions of atoms or molecules in the size range of few to several nanometers and have attracted considerable attentions from both scientific and technological point of views in recent years[1]. Clusters often exhibit structures and properties which are significantly different from those of the corresponding bulk materials and can be studied in different media such as gas phase, colloidal suspension and isolated matrix. Nanoparticles generally consist of 10^2 to 10^4 atoms with a large fraction situated at or near an external interface (i.e. particle surface) or internal interface (i.e. near grain boundaries in heterogeneous phases). The surface atoms have broken bonds and are in a high-energy state compared to the inner atoms[2].

Table 1.1: Shows nanoparticle diameters and the corresponding number of total and surface atoms[2].

Particle diameter	Number of total atoms	Number of surface atoms	Ratio of surface atoms
10 nm	30000	6000	20
5 nm	4000	1600	40
2 nm	250	200	80
1 nm	30	~29	~99

The surface atoms make significant contributions to the properties of NPs via the 'surface effect'. When the particle size becomes comparable to the wavelength of electrons, the energy state of the electrons can be changed leading to changes in physical properties such as magnetic susceptibility, nuclear magnetic resonance, electron spin resonance, heat capacity, optical and infrared absorption etc. This is generally considered 'the quantum size effect'[3]. When particle size decreases, structure in the bulk and nanoscale could differ. For example, the stable structure of indium undergoes a change from body centered tetragonal (bct) in bulk to face-centered cubic (fcc) as particle size is reduced to several nanometers. It is also extensively (both theory and experiment) observed that phase transition temperatures (e.g. the melting temperature) are significantly reduced with the reduction of particle size.

1.1.2 Importance of alloys and alloying at the nanoscale

Alloys played a central role among other materials in early human history when it was recognized that many desired properties can be created by mixing elements deliberately. Very soon alloys were used for the production of tools and weapons essential for the survival of humankind. Although the production of alloys goes back to ancient times, the scientific study of alloys only started in the 19th century. The development of metallic alloys began in east in China, Indonesia, Thailand, Vietnam and east India. The extensive study of alloy was conducted by crystallography, elasticity, electrochemistry and metallography parallel to the advances in experimental methods. To know more about property of alloys, it is necessary to have detailed understanding of their crystal structure, since the properties of alloys depend on their structures. The idea of studying the

crystallinity of alloys was growing in 18 and 19th century and M. Von-Laue in 1912 used X-Ray to identify the crystal structure of alloys (W. H. Bragg immediately used X-Rays for systematic study of all the crystal structures). J. W. Gibbs applied thermodynamics to the phase equilibria of alloys and introduced the concept of phase diagram as the beginning of modern alloy physics. G. Tammann studied phase diagram systematically and initiated the study of binary phase diagrams. Pfeiler et al defined alloy as a class of materials which are mixtures of two or more elements where at least one of them is a metal. In this case the range of metallic properties can be significantly extended by mixing them together.

In the single phase case the alloying element can distribute over the crystal lattice sites of host element and yield a solid solution; (either substitution or interstitial), or it can forms different phases showing up as particles in a matrix. The physical and chemical properties of the solid solutions depend on the chemical composition and arrangements of atoms (atomic structure) and size of the structure in one, two or three dimension. The properties of multi-phase alloys are also determined by the way the second phase particles distribute in a matrix. In many alloy systems specific properties can be further enhanced due to the synergistic effects of multiple phases and compounds. Currently, we are facing tremendous progress in materials development and design of advance materials, driven by technical needs in all fields such as electronics, catalysis and biology. Designing the physical properties of alloys in the bulk is possible by carefully selecting the elements and their concentrations.

The study of alloy nanoparticles (ANPs) is quite challenging, because the determination variables such as temperature (T), particle size (D) and precise composition

simultaneously and over a wide range can be quite challenging. Although in recent years much attention has been paid to ANPs as candidates for new functional materials, and their studies have progressed due to advances in instrumentation, for example Transmission Electron Microscopy (TEM). Recently, nanocrystalline and amorphous alloys have attracted attention, because of improved properties compared to conventional alloys. As previously mentioned proper selection of elements and composition is the key to the design of alloys at micro and nanoscale.

1.2 Configurations and structure of ANPs

The stable thermodynamic configurations (morphologies) of ANPs depend on the relative contributions of surface energy (or interfacial energy) to the total Gibbs free energy of ANPs[4] and other processing related issues (e.g. kinetics). Core-shell structures are formed when elements, that are immiscible, have considerably different surface energies; for elements with the same magnitude of surface energies sub-cluster segregation or mixed patterns (with minimal amount of interface energy) are formed. On the other hand, in different methods of ANPs production (especially chemical method) surface energy of the element can be modified with surfactants, capping agents and solvents. Moreover, the phase diagrams of alloys provide rich information about mixing and segregation of the components[5]. Two phase ANPs are formed as individual particles using physical methods[6] when the composition falls into two phase region but this is rarely observed when synthesized using chemical methods. Formation of two phase particles below 6nm has not been observed due to the instability caused by the interface of two phases and both crystalline[7] and amorphous[8] structures have been reported for different systems.

Generally, prediction of thermodynamically favored configurations for binary systems by chemical methods is difficult due to the fact that kinetics of the reactions during formation may drive the final structure of the particles and the surfactant or solvent can modify the surface energy. In general four types of pattern are seen, as discussed below.

a) Core-shell structure

In the core-shell structure, the first element (A) aggregates in the core, and the other element (B) surrounds the core (as a shell in Figure 1a). Mixed pattern may be observed in the interface of the core and shell. Based on the phase diagram, core-shell structure is expected to form for immiscible systems (in both solid and liquid states) such as (Ag-Ni[9], Ag-Fe[10] and Ag-Co[11] alloys), but at the nanoscale core-shell structure of isomorphic (fully miscible) systems such as Ag-Pd[12] and Au-Ag[13,14,15,16] can form; to our knowledge core-shell structure for eutectic systems have not yet been reported. Core-shell structures can provide multi-functionality and these materials have been proposed for biological applications[75,76].

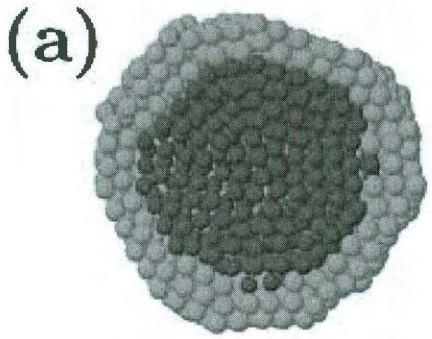

Figure1.1: schematic representation of core-shell structure[1].

b) Sub-cluster segregation

This type of pattern can be observed in two fashions: one, where A and B has an extended interface across the particle (Fig 2, left) and two, where the interface area is minimized in order to minimize the number of A-B bonds (Fig 2, right)[2]. Examples of such structures are shown below.

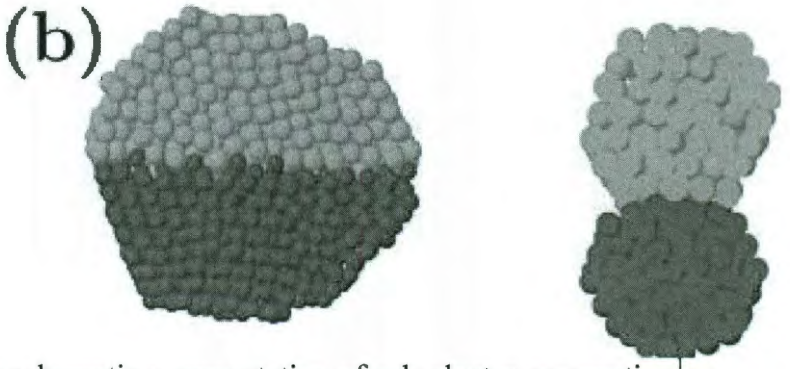

Figure1.2: schematic representation of sub-cluster segregation[1].

Figure 3 is the bright and dark field images of 50 nm $Al_{98}(Bi_x\ Cd_{1-x})$ formed by melt spinning method reported by Bunzel et al[17,18,19,20] (1b pattern); Hagege et al[21] had a similar observation for Pb-Cd inclusion in solid Al matrix.

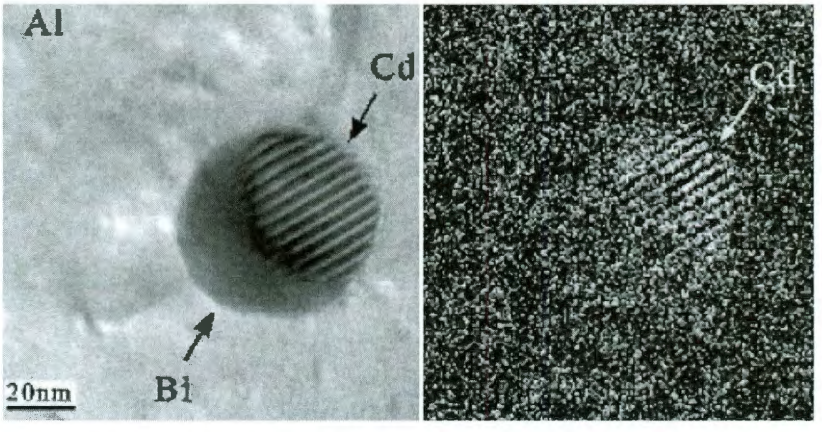

Figure1.3: Bright and dark field TEM image of 50nm Cd-Bi ANPs with sub-cluster segregation pattern embedded in Al grain[20].

Stable 12 nm In-Sn alloys near eutectic alloy compositions were also synthesized (also embedded in an Al matrix) by rapid solidification processing (Figure 4)[22]. Lee et al[23] used in situ TEM to study instability of 12 nm Sn-Bi ANPs composed of two phases with sub-cluster segregation pattern but such pattern wasn't observed for particles below 10 nm (Figure 5)[24]. It is worth noting that all the alloying elements of Bi-Cd, Sn-Bi and Pb-Cd are immiscible in the Al matrix.

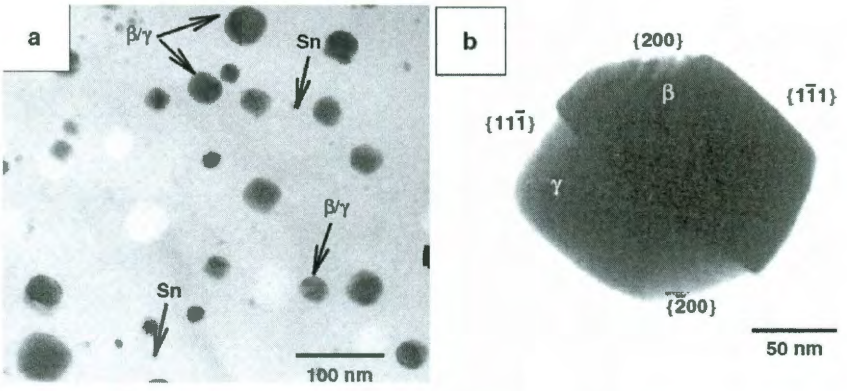

Figure1.4: (a) Sn-In ANPs was synthesized embedded in Al grain by rapid solidification method. (b) Showed the formation of two equilibrium phases of γ with ideal composition of $In_{0.2}Sn_{0.8}$ (hexagonal structure) and β single crystal with $In_{0.7}$ $Sn_{0.3}$ [22].

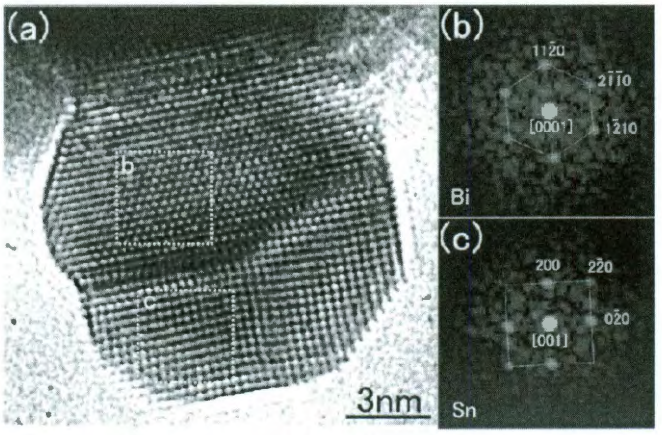

Figure1.5: HRTEM image of 12nm Sn-Bi ANPs contained two phases with sub-cluster segregation pattern. (b) and (c) is the Fourier- transformed patterns taken from frame b &c in Figure (a) confirmed that in part b and c two structures (two phases) exist [23].

Yasuda et al [5] studied particles- size dependence of phase stability and amorphous like phase transformation in Au-Sn ANPs. Figure 6 shows that for NPs above 10nm two phases of AuSn and Au_5Sn co-exist within individual particles.

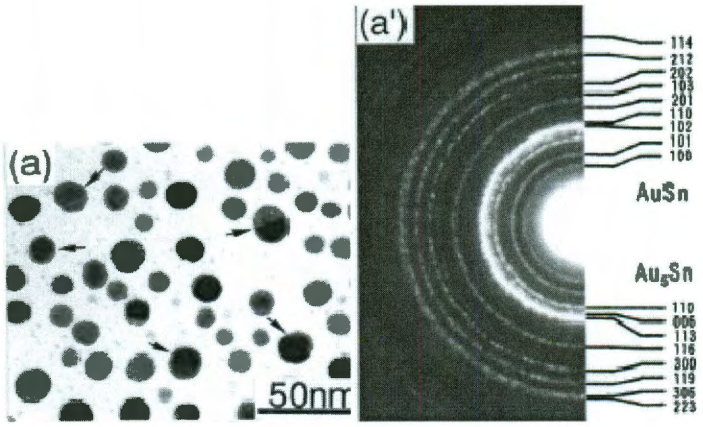

Figure1.6: (a) Bright Field Image (BFI) of 7-20nm Au-Sn alloy ANPs (a′) Selected Area Electron Diffraction (SAED) of (a) confirmed the formation of AuSn and Au_5Sn[5].

Janus particles and three-phase particles with sub-cluster segregation pattern have also been reported by microfluidic method[25] and electrohydrodynamic jetting[26]. In this regard a phase diagram for the particles, including a colloidal-poor (gas) and colloidal-rich (liquid) de-mixing region, has been developed[27].

Formation of sub-cluster segregation was also observed during synthesis using chemical methods. Dumbbell-like Au-Fe_3O_4 structure was synthesized by the decomposition of iron pentacarbonyl, $Fe(CO)_5$, over the surface of the Au NPs followed by oxidation[28].

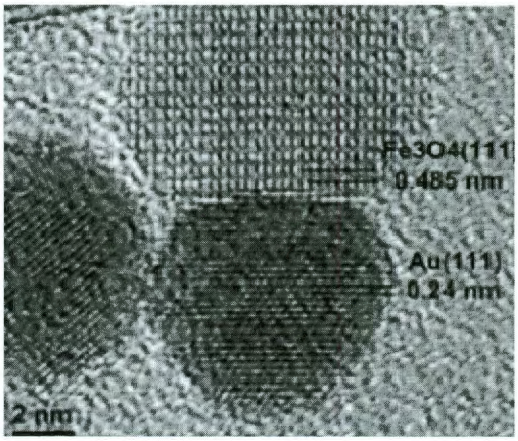

Figure1.7: HRTEM image of one Au-Fe_3O_4 particle with sub-cluster segregation pattern with less bonding for 8nm Au and 4 to 20 nm for Fe_3O_4[28].

Teranishi et al[29] reported that CoPd sulfide NPs were spontaneously formed. in sub-cluster segregation pattern in which one phase is cobalt sulfide (crystalline structure) and the other is palladium sulfide (amorphous structure).

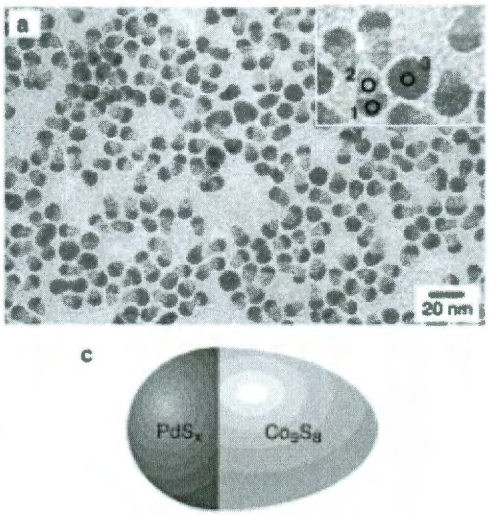

Figure1.8: TEM image of the anisotropically segregation of Pd and Co sulfide nanocorns which were generated by reducing the corresponding metal precursors with 1,2-hexadecanediol in the presence of various alkanethiols.[29].

Banin et al[30] studied the synthesis of asymmetric growth of Au on CdSe nanocrystal{s} quantum rods and dots creating multicomponent smart materials for diode applications.

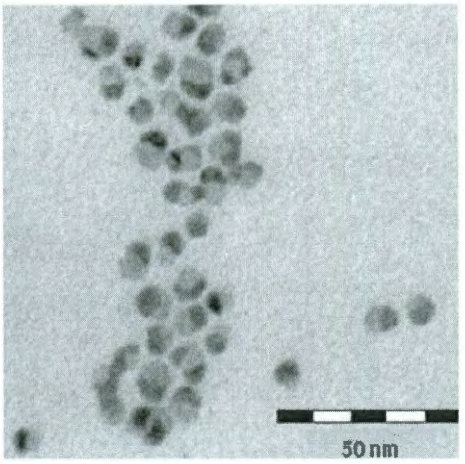

Figure1.9: TEM image of one sided gold tip grown on CdSe semiconductor nanocrystals with chemical method[30].

In all alloy systems mentioned above, existence of two phases in an individual particle were confirmed by electron diffraction (ED), HRTEM or from contrast of components in TEM images.

c) Mixed Systems

This is the most common structure seen in the alloy systems. Mixed alloy particles could have ordered structure (Fig 10a, less observed due to high energy of the system) or disordered structure (Fig 10b). Such structures have been observed for immiscible (Ag-Ni ANPs[31]), isomorphous (Ag-Pd[32], Ag-Au[33,34] ANPs) and eutectic systems (Pt-Sn[35] & Pb-Bi[36] , Ag-Cu [37]ANPs). Formations of ANPs have been reported for many systems and seem to occur more commonly than the core-shell and sub-cluster structures.

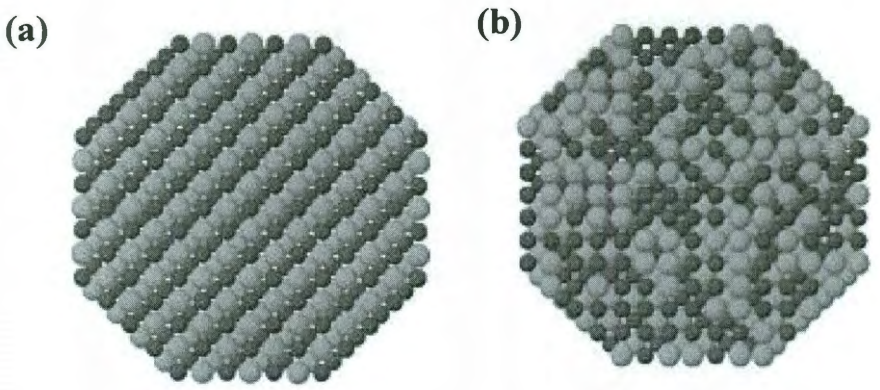

Figure 1.10: Schematic representation of (a) ordered and (b) random alloyed pattern[1].

d) Multi-shell structure

Multi-shell alloy structure may exist in the form of layered A-B-A or onion structure. The metallic bonding of such metastable structure was observed in the growth simulations of Cu-Ag, Ni-Ag, Pd-Ag[38] and Pd-Pt[39] clusters. Also, Drezek et al[40] recently presented computational study of the plasmonic properties of the Au-SiO_2-Au multi layer core-shell structure with the core offset from center. Yacamn et al[41] synthesized stable three layers of Pd-Au ANPs with Au as the inner layer, Pd as core and Pd-rich layer as the outer shell.

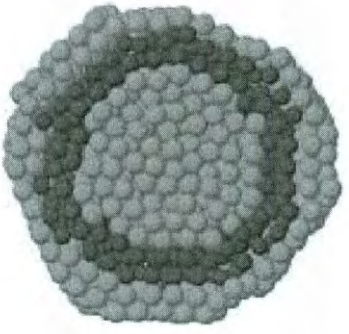

Figure1.11: Schematic representation of three shell patterns[1].

Au-Pb-Cd is another example where Pb and Cd ions were reduced by γ radiation on the surface of colloidal gold particles (190Å in diameter) in Ar atmosphere[42].

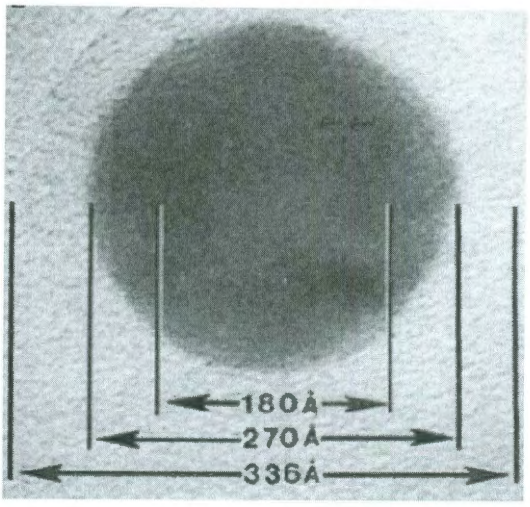

Figure 1.12: High resolution micrograph of particle with three layers. Au is located in the core indicated by two arrows; Pb and Cd are reduced on Au core, respectively[42].

e) Alloyed Core- Shell

De et al [43]generated alloyed core (Au-Pt)-shell(Pt) ANPs in glassy silica film by sol-gel method followed by heating up to 450° C in Ar/H_2 atmosphere. Increasing the amount of Pt led to the formation of a shell around the alloyed core. Despite the common theory that the element with lower surface energy (surface energy of Au= 1.39±0.07 (J/m^2) and Pt=2.28±0.8 (J/m^2)) [44] segregate to the surface, De et al's report suggests that there are other factors that plays important role in final structure of the ANPs. Henglein et al reported radiolytic formation of AuSn phase as a core and Au around it with γ radiation in aqueous solution. They suggested that variability of the original core element shape can affect the final ANPs structure[45].

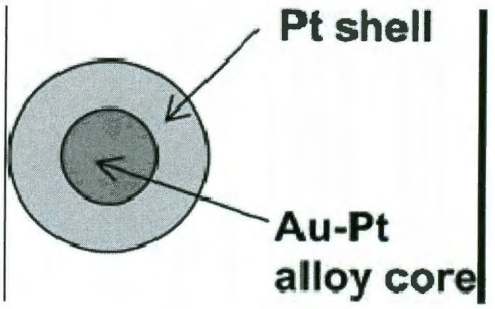

Figure1.13: schematic representation of Au-Pt alloyed core-shell pattern[43].

1.3 Possible structures

In general, geometrical shapeS of ANPs and NPs are determined by the composition and properties of the materials, or by the formation mechanism[46]. In this section we discuss the possible configurations for ANPs and NPs. Distinct structure was observed for transition metal NPs such as cubooctahedron, icosahedron and decahedron (Figure 14). Clusters within 150-200 atoms crystallize in icosahedron fashion which is not stable for larger clusters and transform to cuboctahedral as sub-structure of the FCC lattice.

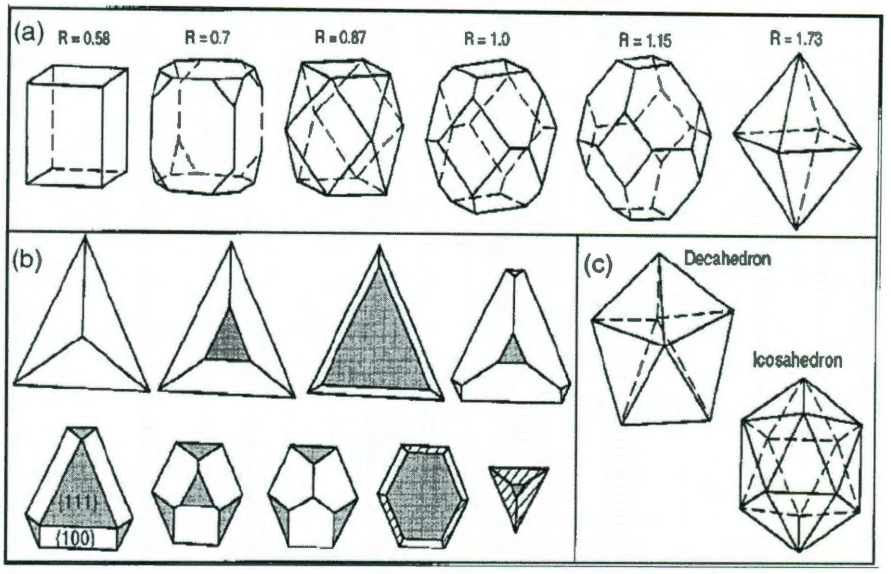

Figure 1.14: a) Geometric shape of cubooctahedral nanocrystal as a function of R (R is determined by growth rate in (100) direction to that of (111)).b) shape evolution of (111) plane based NPs when the ratio of 1/R plane increase c) Geometrical shapes of multi twinned decahedral and icosahedral clusters[44].

Noncrystalline structures can also form in icosahedra, decahedra, polytetrahedra, and polyicosaherda[1]. Noncrystalline structures generally may form in compact shapes with an efficient packing of atoms obtained at the expense of internal strain due to non-optimal interatomic distances in the structure. The strain energy is proportional to the cluster volume, so noncrystalline structures become unfavorable for large clusters[47]. Figure 15 shows the quantitative stability behavior of different types of clusters versus their size. When the size mismatch between atomic species is large, and small atoms can be accommodated inside the cluster to reduce the compressive strain, icosahedra, polytetrahedra, and polyicosahedra tend to be more favorable for nano-alloys. For pure copper clusters, the lowest energy structures are found to be based on icosahedral packing, while pure gold clusters tend to form less symmetrical (often amorphous) structures. In a number of cases, the replacement of a single gold atom by copper is found

to be sufficient to convert the structure to that of the more symmetrical copper cluster. The lowest energy clusters are generally more difficult to find for the bimetallic clusters than for the pure metallic clusters, due to the presence of homotops (related by permuting Cu and Au atoms), as well as geometrical isomers.[48]. Electronic shell may enhance the stability of specific structural motifs. Examples are found in Cu-Ag clusters (with 40 atoms), in which a specific core-shell polyicosahedral structure is stabilized due to electronic effects[49].

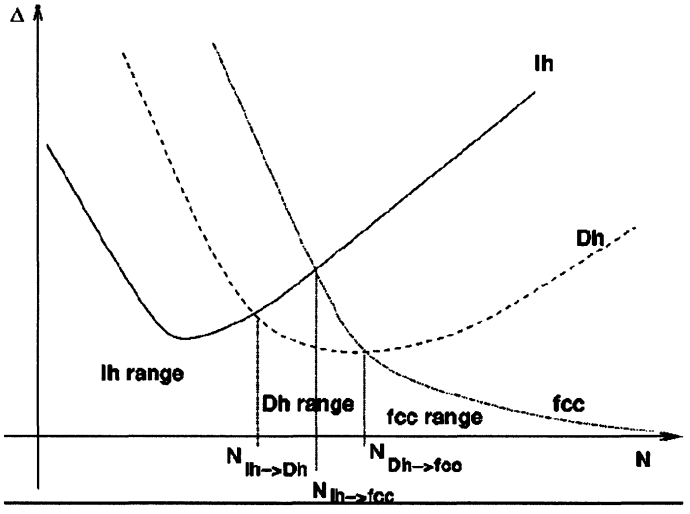

Figure 1.15: Numerical stability behavior of clusters versus number of atoms base on optimization of volume or surface energy contribution [47].

1.4 Factors influencing mixing and atomic ordering of ANPs

The degree of segregation, mixing and atomic ordering of alloy nanoparticles generally depend on the structure and property of the constituent materials. Parameters affecting the formation of bulk alloys are as follows.

- Atomic size: Hume Rothery pointed out that the solubility of two elements strongly depends on their atomic size. If the difference between atomic diameters

is higher than 15%, the solubility of elements is restricted and other factors won't be taken into account[50].

- Electronegativity: High electronegativity difference between two elements leads to the formation of a brittle intermetallic compound rather than the solid solution.
- Valance electron: A metal with higher valency is more prone to dissolve in a metal with lower valency[51].
- Crystalline structure: Formation of continuous solid solution is possible only when both elements have the same structure.

Elements are generally more soluble with their neighboring elements in the periodic table at both bulk and nano-scale. Comparison of parameters affecting the formation of alloys at both scales is quite difficult, because bulk alloys are formed by melting processes at high temperatures and ANPs form from both chemical and physical methods and each method has its own intrinsic characteristics. Ferrando et al. discussed the factors affecting mixing, segregation and ordering of ANPs.

- Relative strengths of A-A, A-B and B-B bonds: If A-B bonds are strongest among the other bonding, mixing is favored for this system; otherwise, formation of core at the center of the cluster is expected.
- Surface energy of both elements: The element with lower surface energy generally tends to segregate to the surface. The surface energy of elements can be modified by surfactants[52] or capping agents, for example instead of A_{shell} B_{core}, B_{shell} A_{core} (i.e. Pd-Ag[9]) can form with the addition of surfactant.
- Relative atomic sizes: Atom with smaller size tends to sterically confine to the core, especially where the core is under compression. Large lattice mismatch

leads to the formation of core-shell structure, but alloyed structure can be formed kinetically (e.g. Ag-Ni ANPs)[53].

- Strength of bonding to surface ligands: The element which has a strong bonding to ligand tends to pull out toward the surface to make the structure more stable.
- Specific electronic/magnetic effect: Certain size and compositions may be stabilized by electronic shell structure or electron spin interaction.
- Charge transfer: The electron transfer occurs from less electronegative element to more electronegative element. When the electronegativity of two elements are close to each other the bonding between them is more metallic[54,55].
- Self-diffusion coefficient: Experiments and calculations confirm that increase in self-diffusion coefficient (e.g. magnitude of 10^{-28} m^2s^{-1} for 2 nm sized Au particles and for bulk is 3.6×10^{-32} m^2s^{-1} at room temperature) leads to rapid alloying in the solid state at room temperature[56,57].
- Crystal structure may not have a strong influence on the formation of solid solution at nano-scale, because lattice structure of metal is softened and strain is relaxed much more easily than bulk[3].
- Formation of alloy at nano-scale is remarkably size dependent which has been observed in different alloy systems. For example vapor deposition of Cu on 4nm Au NPs resulted in alloying with Au at room temperature, since diffusion coefficient of materials is extremely higher than bulk. For 10nm Au NPs only formation of core-shell structure has been observed and for particles above 30nm no alloying has been seen [1,58]. Shibata et al[59] have studied the size dependent alloy formation of Ag coated Au NPs in aqueous solution.

1.5 Practical relevance of ANPs

ANPs have been utilized in a number of technologies and catalysis applications (catalytic convertor in automobile[60,61,62]and electrochemical reactions[63,64]), and their magnetic[65,66] and bio-medical properties have been extensively studied.

1.5.1 Catalysis

The purpose of alloying monometallic systems is to tune, modify and improve reactivity by the interaction of neighboring atoms due to synergistic effects. It is well known that d-character of the metals is related to their catalytic activity; though selection of proper transition metal can lead to higher catalytic activity. Most of transition and noble metallic catalysts are expensive; therefore, core-shell bimetallic clusters (cheaper element design as a core and precious metal with better catalysis activity as a shell) can be economical. Homogeneous catalysis in solution showed poor performance, however, heterogeneous catalysis in which the NPs were supported on substrates has reported due better performance[67]. As an example, bimetallic catalysts containing Pd such as Pd-(Sn[68], Au[69,70], Fe[71]) was reported be better for removing chlorinated compounds (especially chlorinated ethenes) from water which is a significant environmental problem in industrialized nations.

1.5.2 Biological applications

In the past decade there has been tremendous interest in the use of ANPs and nanostructures in bio-molecular diagnostics in biomedical applications such as bioconjugate, cellular labels and DNA/protein markers for disease[72]. Because of the tunability of bimetallic alloys (composition, ordering, shape and size[73]) they show

potential application in biodiagnostics. Zhang et al[74] reported core-shell structures (metallic, semiconductor, lanthanide and polymeric) for bioimaging, drug delivery and cell labeling. He also reported different types of methods such as radical polymerization, electrodeposition, sol-gel, reverse micelle, and mechanochemical methods to produce core-shell structure. Absorption band in visible region of Au NPs can be tuned by SiO_2 shell[75], and the thickness of the shell plays a critical role in the absorption shift. West et al [76]reported Au-SiO_2 shell for thermal therapy of tumors under magnetic resonance guidance. However, by adding another shell around the core-shell structure, it is possible to add extra functionality to the nanostructure. For example, novel FITC (anti-body capped by SiO_2) encapsulated particles with nanoscale ZnO surface layer can be used as smart nanostructure for particle tracking, cell imaging, antibacterial treatments and cancer therapy[77]. Recently, smart core-shell hydrogel was synthesized with Ag NPs core for cancer cell imaging and gel shell for pH regulated drug delivery[78].

References

[1] R. Ferrando, J. Jellinek, Nanoalloy: From theory to application of alloy clusters and nanoparticles, Chem. Rev., 108 2008, 845-910.
[2] W. Pfeiler, Alloy Physics, Wiley, 2007.
[3] W.P. Halperin, Quantum size effect on metal particles, Rev. Modern phys., 58, 1986, 533-607.
[4] J.-G.Lee, H. Mori, Solid/liquid two-phase structures in isolated nanometer-sized alloy particles, Phy. Rev. B, 70, 2004, 144105-1 to 5.
[5] M.Gaurdy, E. Cottancin, Size and composition dependence in the optical properties of mixed embedded clusters, Phys. Rev. B, 67, 2003, 155409-1 to 9.
[6] H. Yasuda, K. Mitsuishi, H. Mori, Particle-size dependence of phase stability and amorphous like phase formation in nanometer-sized Au-Sn alloy particles, Phy. Rev. B, 64, 2001, 094101-1.
[7] R. A. Morales- Luckie, v. Sanchez-Mendieta, One step aqueous synthesis of stoichiometric Fe-Cu nanoalloy, Mater. Lett., 62, 2008, 4195-4197.
[8] H. Mori, H. Yasuda, Alloy phase formation in nanometer- sized particles, Mat. Science & Eng. A, 312, 2001, 99-103.
[9] A. Kumar, C. Damle, Low temperature crystalline Ag–Ni alloy formation from silver and nickel nanoparticles entrapped in a fatty acid composite film, App. Phys. Lett. 79, 2001, 3314-3316.
[10] M. P. Andrews, Gas-phase "molecular alloys" of bulk immiscible elements: Fe, Ag, J. Phys. Chem., 96, 1992, 8233-82341.
[11] N. S. Sobal, M. Hilgendorff, Synthesis and structure of colloidal bimetallic nanocrystals: the non-alloying ystem Ag/Co, Nano Lett., 2, 2002, 621, 624.
[12] D. V. Goia, E. Matijevic, Preparation of monodispersed metal particles, New J. Chem., 22, 1998, 1203 – 1215.
[13] Z. Y. Li, J. Yuan, Direct image of core-shell in Ag-Au bimetallic nanoparticles, App. Phys. Lett, 87, 2005, 243103-1 to 3.
[14] J. H. Hodak, A. Henglein, Laser-Induced inter-diffusion in AuAg core-shell nanoparticles, J. Phys. Chem. B , 104, 2000, 11708-11718.
[15] I. Srnova´-Sÿ loufova´,B. Vlcˇkova, Bimetallic (Ag)Au Nanoparticles prepared by the seed growth method: two-dimensional assembling, characterization by Energy Dispersive X-ray Analysis, X-ray Photoelectron Spectroscopy, and Surface Enhanced Raman Spectroscopy, and proposed mechanism of growth, Langmuir, 20, 2004, 3407-3415.
[16] I. Srnov-loufov, F. Lednick, Core–Shell (Ag)Au bimetallic nanoparticles: analysis of transmission electron microscopy images, Langmuir, 16, 2000, 9928-9935.
[17] M. Herlach, Solidification and crystallization, Wiley, 2003.
[18] G. Wild, P. Bunzel, Phas eqilibria and phase diagrams of nanoscaled systems, Alloys and compounds, 434, 2007, 286-289.
[19] M. Herlach, Phase transformations in multicomponenet melts, Wiley, 2008.
[20] P. Bunzel, PhD Thesis, Saarland University, 2004.
[21] S. Hagege, U. Dahmen, Morphology, structure and thermal behavior of small eutectic Pb- Cd inclusions in aluminum, Phil. Mag. Lett., 76, 1996, 259-266.

[22] V. Bhattacharya, K. Chattopadhyay, Synthesis, transformation and superconductivity of dual phase In–Sn alloy nanoparticles embedded in an Al matrix, , Phil. Mag. Lett., 85, 2005, 577–585.
[23] J.-G. Lee, H. Mori, In situ HRTEM study on the structural instability of isolated nanometer-sized alloy nanoparticles in the Sn-Bi system, J. Electron Microscopy, 52, 2003, 57-62.
[24] J.-G.Lee, H. Mori, In-situ observation of alloy phase formation in nanometre-sized particles in the Sn-Bi system, Phil. Mag. Lett.,84, 2004, 2675-2686.
[25] Z. Nie, W. Li, Janus and Ternary particles generated by microfluidic synthesis: design, synthesis and self assembly, J. AM. CHEM. SOC, 128, 2006, 9408-9412.
[26] K. H. Roh, D. C. Martin, Biphasic Janus particles with nanoscale anisotropy, Nature, 4, 2005, 759-763.
[27] F.Sciortino, A. Giacometti, Phase diagram of Janus particles, Phys. Rev. Lett., 103, 2009, 237801-1 to 4.
[28] H. Yu, M. Chen, Dumbbell-like bifunctional Au-Fe_3O_4 nanoparticles, Nano. Lett., 5, 2005, 379-382.
[29] T. Teranishi,Y. Inoue, Nanoacorns: Anisotropically phase-segregated CoPd sulfide nanoparticles, J. AM. CHEM. SOC., 126, 2004, 9914-9915.
[30] T. Mokari, C. G. Sztrum, Formation of asymmetric one-sided metal-tipped semiconductor nanocrystal dots and rods, Nature Materials, 4, 2005, 855-863.
[31] C.C. Lee, Y.Y. Cheng, Synthesis and electromagnetic wave absorption property of Ni–Ag alloy nanoparticles, J. Alloys and Compounds 480, 2009, 674–680.
[32] C. Damle, A. Kumar, Synthesis of Ag/Pd nanoparticles and their low temperature alloying within thermally evaporated fatty acid film, J. Phys. Chem. B,106, 2002, 297-302.
[33] Q. Zhang, J. Y. Lee, Size and composition tunable Ag-Au alloy nanoparticles by replacement reaction, Nanotechnology, 18, 2007, 1-8.
[34] P. Raveendran, J. Fu, A simple and green method for the synthesis of Au-Ag alloy nanoparticles, Green Chem., 8, 2006, 34-38.
[35] H. Bonnemann, P. Britz, Structure and chemical composition of a surfactant-stabilized Pt_3Sn Alloy colloid, Langmuir, 14, 1998, 6654-6657.
[36] W. A. Jesser,1 R. Z. Shneck, Solid-liquid equilibria in nanoparticles of Pb-Bi alloys, Physical Review B, 69, 2004, 144121-1 to 13.
[37] A. B. Smetana,, K. J. Klabunde, Low- temperature metallic alloying of Copper and silver nanoparticles with gold nanoparticles through digestive ripening, J. Phys. Chem. B, 110, 2006, 2155-2158.
[38] F. Baletto, C. Mottet, Growth of three-shell onion like bimetallic nanoparticles, Phys. Rev. Lett., 90, 2003, 135504-1 to 4.
[39] D. Cheng, W. Wang, The onion-ring Structure for Pd-Pt bimetallic clusters, J. Phys. Chem. Lett. B, 110, 2006, 16193-16196.
[40] Y. Hu, S. J. Noelck, Symmetry breaking in Gold-Silica-Gold multilayer nanoshells, ACS Nano, DOI: 10.1021/nn901743m.
[41] D. Ferrer, A. Torres-Castro, Three- layer core-shell structure in Au-Pd bimetallic nanoparticles, Nano. lett., 7, 2007, 1701-1705.

[42] P. Mulvaney, M. Giersig, Surface chemistry of colloidal gold: deposition of lead and accompanying optical effects, J. Phys. Chem. ,96, 1992, 10419-10424.
[43] G. De, C. N. R. Rao, Au–Pt alloy nanocrystals incorporated in silica films, J. Mat. Chem., 15, 2005, 891-894.
[44] R. A. Swalin, Thermodynamics of solids, John-Wiley, 1972, Chap 10, 231.
[45] A. Henglein, M. Giersig, Radiolytic formation of colloidal Tin and Tin-Gold particles in aqueous solution, J. Phys. Cham., 98, 1994, 6931-6935.
[46] S.C. Tjong, H. Chen, Nanocrystalline materials and coatings, Mat. Sci. Eng. R, 45, 2004, 1–88.
[47] F. Baletto, R. Ferrando, Structural properties of nanoclusters: Energetic, thermodynamic, and kinetic effects, Reviews of Modern Physics, 77, 2005, 371-417.
[48] S. Darby, T. V. Mortimer-Jones, Theoretical study of Cu–Au nanoalloy clusters using a genetic algorithm, J. Chem. Phys., 116, 2002, 1536-1550.
[49] G. Barcaro, A. Fortunelli, Electronic and Structural Shell Closure in AgCu and AuCu Nanoclusters, J. Phys. Chem. B, 2006, 110, 23197-23203.
[50] R. E. Reed –Hill, Physical metallurgy principle, D. Van nostrand compony, NJ, London, Toronto, 1967.
[51] R. Stefec, Primary solid solution in binary Ni alloy system, Czech. I. Phys. B, 21, 1971, 860-877.
[52] M.R. Porter, Handbook of surfactants, Blackie academic and professional, 1994.
[53] K.Yu, Z. Wu, High temperature stable Au@SnO_2 Core/shell supported catalyst for CO oxidation. J. Phys. Chem. Lett. C, 112, 2008, 2244-2247.
[54] C. Suryanarayana, Mechanical alloying and milling, Marcel Dikker, NY, USA, 2004.
[55] C. Suryanarayana, Mechanical alloying and milling, Progress in Materials Science, 46, 2001, 1-184.
[56] K. Dick, T. Dhanasekaran, Size-Dependent melting of silica-encapsulated gold nanoparticles, J. Am. Chem. Soc., 124, 2001, 2312-2317.
[57] S. M. Makin, A. H. Rowe, Self-Diffusion in gold, Proc. Phys. Soc. B, 70, 1957, 545-552.
[58] H. Yasuda, H. Mori, Cluster-size dependence of alloying behavior in gold clusters, Z. Phys. D, 31, 1994, 131-134.
[59] T. Shibata, B. Bunker, Size-dependent spontaneous alloying of Au-Ag nanoparticles, J. Am. Chem, Soc., 124, 2002, 11989-11996.
[60] Z.Liu, E.T. Ada, Synthesis and activation of PtRu alloyed nanoparicles with controlled size and composition, Chem. Mater. 18, 2006, 4946-4951.
[61] W. Vogel, P. Britz, Structure and chemical composition of surfactant-stabilized PtRu alloy colloid, J. phys. Chem., B, 101, 1997, 11029-11036.
[62] P. K. Babu, H. S. Kim, Electronic alternations caused by ruthenium in Pt-Ru alloy nanoparticles as revealed by electrochemical NMR, J. Phys. Chem. B,107, 2003, 7595-7600.
[63] G. Ren H. Shi, Synthesis and composition evolution of bimetallic Pd-Pt alloy nanoparticles, nanotechnology, 18, 2007, 385604(1 to 6).
[64] T. nakashima, S. Nohra, A new simple prepration of platinum- nickel alloy nanoparticles and their characterization as electrocatalyst for methanol oxidation, Res. Chem. Intermed., 32, 2006, 561-573.

[65] E. E. Carpenter, C. T. Seip, magnetism of nanophase metal and metal alloy particles formed in ordered phase, J. Appl. Phys., 85, 1999, 5184-5186.
[66] S. K. Lim, K. S. Ban, Monolayered Ni-Co nanoparticles template fabrication using a Ni nanoparticles array, Appl. Phys. Lett., 88, 2006, 163102(1 to 3).
[67] C. Burda, X. Chen, chemistry and properties of nanocrystals of different shapes, Chem. Rev., 105, 2005, 1025-1102.
[68] C. J. Lin, Y. H. Liou, Supported Pd/Sn bimetallic nanoparticles for reductive dechlorination of aqueous trichloroethylene, Chemosphere, 74 ,2009, 314–319
[69] M. Wong, P. J. J. Alvarez, Cleaner water using bimetallic nanoparticle catalysts, J. Chem. Technol. Biotechnol, 84, 2009, 158–166.
[70] Y. W. Lee, N. H. Kim, Synthesis and characterization of flowered-shape porous Au-Pd alloy nanoparticles, J. Phys. Chem. C, 112, 2008, 6717-6722.
[71] H. L. Lien a, W. X. Zhang, Nanoscale Pd/Fe bimetallic particles: Catalytic effects of palladium on hydrodechlorination, App. Cat. B, 77, 2007, 110–116.
[72] N. L. Rosi and C. A. Mirkin, Nanostructures in Biodiagnostics, Chem. Rev. 2, 105, 2005, 1547-1562.
[73] R. Jin,Y. W. Cao, Photoinduction conversion of silver nanospher to nanoprism, Science, 294, 2001, 1901-1903.
[74] N. Sounderya, Y. Zhang, Use of core-shell structured nanoparticles for biomedical application, Recent Patent on Biomedical Engineering, 1, 2008, 34-42.
[75] A. Kumar, V. L. Pushparaj, Synthesis of silica-gold nanocomposites and their porous nanoparticles by an in-situ approach, Langmuir, 22, 2006, 8631-8634.
[76] L.R. Hirsch, R. J. Stanfford, Nanoshell- mediate near infrared thermal therapy of tumors under magnetic resonance guidance, PNAS, 100, 2003, 13549-13554.
[77] H. Wang, D. Wingett, Fluorescent dye encapsulated ZnO particles with cell-specific toxicity for potential use in biomedical applications, J. Mat. Sci.: Materials in Medicine, 20, 2009, 1573-4838.
[78] W. Wu, T. Zhou, Smart core-shell hybrid nanogels with Ag nanoparticle core for cancer cell imaging and gel shell for pH-regulated drug delivery, Chem. Mat., DOI:10.1021/cm903357q.

Chapter 2

Methods for generating alloy nanoparticles (ANPs)

2.1 Introduction

ANPs can be generated by both chemical and physical methods in different media such as gas phase (molecular beam or vapor phase), solution (colloidal suspension) and isolated in inert matrices or on surfaces. In physical methods, fine particles are produced by applying energy to the bulk metal; however in chemical methods, metal atoms are obtained by reducing metal ions in the solution. Figure 2.1 shows the schematic of two types of generation methods[1]. The methods used to generate ANPs are the same as those used for pure monometallic systems[2,3], although the formation of ANPs is not straight forward as the system may lead to the generation of NPs of both elements and not the alloy.

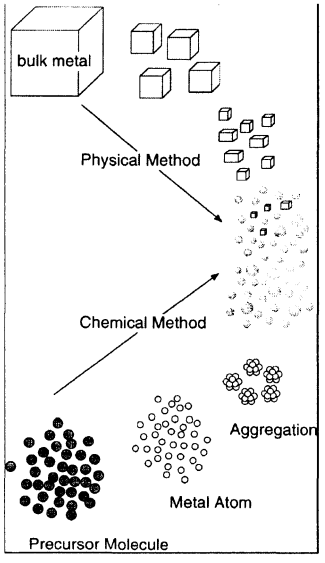

Figure 2.1: Schematic of generation methods for both monometallic and bimetallic systems at nano-scale[1].

2.2 Chemical methods

Chemical method is a bottom- up approach to produce both monometallic particles and ANPs. Colloidal dispersion of metallic particles is usually synthesized by chemical reduction of metal salts by formaldehyde[4], hydrazine[5], hydrogen, hydrogen peroxide and carbon monoxide in an appropriate solvent in presence of surfactant or polymeric ligands. Faraday reported the synthesis of Au ANPs without stabilizer in 1857 in which counteranions may have played the role as a stabilizer[71]. These types of Au NPs (without stabilizer or week ligands) are the best candidate to synthesize Au based alloy particles.

2.2.1 Co-reduction

Bimetallic colloids can be synthesized by chemical reduction of mixture of metal salts with strong reducing agent such as sodium borohydrate ($NaBH_4$), hydrazine (N_2H_4) or H_2 gas[1]. Stabilization of NPs is possible by two distinct mechanisms:

- Electrostatic stabilization: Charged layered of ions on the NPs surface, causing columbic repulsion between NPs (e.g. sodium citrate cause repulsion on the surface of Au NPs) prevent them from aggregation.
- Steric stabilization: Long chains of bulk organic molecules such as polymers and copolymers with P, N, S donor prevent NPs from aggregation[6].

The configuration type of product formed with co-reduction method could be:

1- Core-Shell structure: If there is a large difference between redox potential of both metals, core-shell structure is favored. The element with higher redox potential reduces as a core and the other element as shell. Proper capping agent can replace

the core and shell with each other (e.g. Pd-Ag). Pd with the higher redox potential reduces as core and later on Ag reduces as shell $Pd_{core}Ag_{shell}$ on top of Pd core. Ammonia leads the system to the formation of $Ag_{core}Pd_{shell}$, since ammonia has a better attachment to Pd than Ag[9].

2- Alloyed NPs: For metal ions with the close redox potentials and high enthalpies of mixing, alloyed NPs can be synthesized.

A challenge that confronts the current method is when elements do not have a close redox potentials, an element with positive redox potential reduce first, and the system may proceed to mixture of both elements instead of alloyed structure. Co-reduction method can be used to synthesize not only particles, but also tubes, and sheets at higher temperature[7]. Monometallic systems (with the control shape)[8] and different non-metallic compounds have also been reported to be produced by this method[9].

2.2.2 Two step successive reductions

Atoms of a metal can be deposited on the surface of cluster without any passivating ligand or with weakly attached surfactant molecules such as citrate. Resultant structure of current reaction would be core-shell (e.g., $Au@SiO_2$ and $Au@SiO_2@ZrO_2$)[10] or alloyed structure (e.g., FePt)[11,12]. Schematic of this process is shown in figure 2.2. Watzky et al postulated the possibility of metal polymer to produce onion like layered structure by slow reduction of metallic salt under H_2[13] which might offer more functionality to the system[70]. Successive method can also be used not only for NPs, but also to synthesize core-shell nanorods. Khannal[14] et al reported formation of Au-Pt dogboned shaped nanorod.

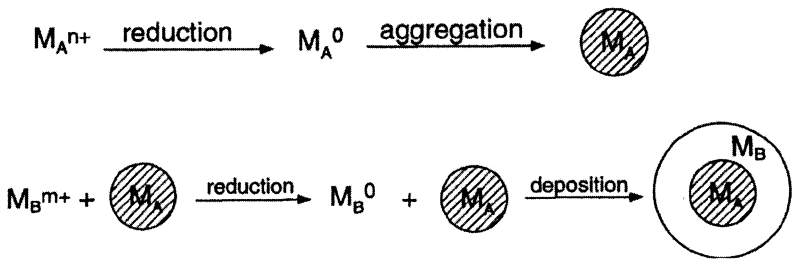

Figure 2.2: schematic of formation of core-shell structure with two step successive reductions[2].

2.2.3 Reduction of co-complexes

In this method the precursor is a complex molecule which contains both of the metal species. An example of this method is the synthesis of Ag-Pd bimetallic particles by photo-reduction (using UV light) of Ag(I)bis(oxalato)palladate(II) in aqueous solution in presence of poly(N-vinyl-2- Pyrrolidone) and also Ag-Pt was synthesized by sodium borohydride reduction of silver (I) bis(oxalato)platinate(II) ($Ag_2[Pt(C_2O_4)_2]$) in ethylene glycol[15].

2.2.4 Thermal decomposition of transition metal complex

This method has been used to generate mono-metallic and bimetallic[16] NPs particularly more noble metals with low-valent transition- metal complex (organometallic compounds and clusters or labile noble metal salts[17]). Particles synthesized with this method could be very small in size, if thermolysis is performed in presence of stabilizing ligands such as PVP[18]. These nanocatalysts were found to exhibit high catalytic activities and frequently high activity for longer periods than colloidal catalysis which are prone to coalescence and sintering. Bare ANPs (e.g. Ni-Cu, Au-Ag, Ni-Pd and Cu-Pd) are reported to be synthesized with this method[19].

2.2.5 Polyol Process

Polyols are alcohols containing multi-hydroxyl group. They are used in food and polymer industry; a class of polyol called sugar polyol is added to food as low calorie sugar. Generally, polyol process is used to synthesize monometallic[20], bimetallic[21,22,23], nonmetallic and compound[24]. In polyol process precursors are dissolved in a two hydroxyl group alcohol then depending on the surfactant or capping agent heating, reducing agent or radiation (with microwave) applied for reduction.

2.2.6 Water in oil microemulsion

Water in oil microemulsion is generally used to synthesize monometallic, compounds[25], and bimetallic systems. Ni NPs are reported to synthesize by the reduction of nickel chloride with hydrazine in the cationic water-in-oil microemulsions of water/CTAB (cetyltrimethylammonium bromide)/n-hexanol at 73°C[26]. Pt-Ru ANPs can be formed by mixing two stable microemulsions of Pt and Ru in contact by hydrazine droplets[27]. Also, formation of core-shell structure (CeO_2@SiO_2) has been reported with this method[28].

2.2.7 Biosynthesis

Biosynthesis is bottom- up approach to generate both NPs and bimetallic compounds by bimolecules. Biosynthesis includes the formation of chemical compound, NPs and nanocrystals by living organisms which are subsequently organized on longer length scale, because macromolecules act as template in current system[29].

One of the processes for biosynthesis is biomimetic synthesis. In this method biology has inspired variety of methods to organize inorganic materials at the nanoscale. Final

product with this method is particles or nanocrystals wrapped with biological systems such as proteins, polysaccharide, DNA or combinatorial phage which is more representative of a nanocomposite[30]. Polysaccharidice alginate biopolymers have been used as templates to synthesize Ni, Co and NiCo ANPs with controlled growth. The same process can be developed to synthesis Au, Ru and Fe NPs[31].

In the other process, certain microbes can reduce the metals to their zero state (to the metallic state). Macaskie and co-workers used bacterial hydrogenases to reduce aqueous Pd (II) to cell-bonded Pd (0) NPs with variable sizes. These biogenerated NPs are used for bioremediation of industrial wastes, reclamation of precious metals (e.g. Pd and Pt), and formation of high quality bio-catalysis for use in hydrogen fuel cell and other applications. Ni-Ti clusters have been studied by molecular dynamic simulation and produced by reduction of the mixture of Ni^{+} and Ti^{+} with alfalfa[32].

2.3 Physical methods

Physical methods are up-bottom approaches which usually require expensive equipments and user instrument training. These methods are usually not scalable and scientists use them for fundamental studies. In physical methods, nanostructures such as nanoparticles and nanorods (monometallic, two or multi components metallic systems and compounds) are produced by applying energy to the bulk substances[33].

2.3.1 Solution dispersion

This method could be used to synthesize NPs (e.g. Sn[34] and In[35]) and also In-Sn[36] ANPs. Bulk alloy (or metal) is dispersed in paraffin oil and the whole system is sealed and

heated up to 180℃. Disperse product in paraffin oil is centrifuged and then dispersed in proper solvent for characterization.

2.3.2 Molecular beam

Molecular beam is a method to generate free clusters in an interaction-free environment; so called cluster beam. This method can be used for both mono and bimetallic[37] systems. Clusters generate in cluster source with cluster generation consists of two steps process:

- Vaporization nucleation: this step includes both nucleation and growth. Atoms and molecules begin condensation in the form of cluster and then nucleus starts to growth. More atoms and molecules add to the initial nuclei.

- Coalescence aggregation: Merge small cluster to larger clusters.

Different types of cluster sources exist, depending on how volatile or refractory metals are.

1. Laser vaporization: Target can be in the form of powder (only monometallic powder or mixture of two metals) or rod which is vaporized by laser beam.

2. Pulse arc cluster: By passing an intense electrical discharge through the target, mono or bimetallic target is vaporized.

3. Ion sputtering: High energy inert gas ion, generally K^+ or Xe^+ is used for bombarding the metal target to produce clusters.

4. Magnetron spattering: dc or rf is used to ignite argon plasma (Ar^+) over a target and the whole system is confined in a magnetic field[1].

Recently, the epitaxial growth of MgO and CoFe/MgO on Ge (001) substrates using molecular beam epitaxy was reported at low temperature growth of 125 ^{o}C[38].

2.3.3 Ion implantation

This method can be used to generate monometallic[39,40], bimetallic[41] and also different compounds. Metal ions are dispersed in glassy substrate like silica and reduced by ion beams with energy of 100 Kev. Metal nanoclusters embedded in glassy matrix have attracted interest, because of optical, magnetic and catalysis properties. The sequential implantation of two different metal ions has been used to generate solid solution of systems such as Ag-Au, Cu-Pd and Cu-Au[42]. This method can be used for both metal and bimetallic system.

2.3.4 Melt spinning

The concept of the melt spinner was developed by Pond and Maddin[43] in 1969, whereby liquid was quenched on the inner surface of a drum. Melt spinning is the preferred method of manufacture for polymeric fibers. The polymer is melted and pumped through a spinneret (die) with numerous holes (one to thousands)[44]. This method is also used to produce alloyed nanostructures such as Bi-Cd and Pb-Cd embedded in Al matrix.

2.3.5 Heat Treatment

This method can be used to synthesize both NPs and bimetallic compounds. In this method metal ions are deposited on glassy or polymeric matrixes like silica gel or fatty acid. G. De et al[42] synthesized Au-Pt ANPs by trapping $AuCl_3^{-4}$ and $PtCl_6^{-2}$ ions in silica gel and heating up to 450°C in H_2-Ar gas mixture until both ions reduce with each other.

Kumar et al [45]reported preparation of fatty acid (stearic acid) films by immersion of the film in Ag_2SO_4 and $NiSO_4$ solution Ag^+ and Ni^{+2} are trapped on fatty acid in pH=6 and Ag_xNi_{1-x} phase was reported to form after heat treatment at low temperature ~100°C[9]. AgCo ANPs can be synthesized by dissolving Ag and Co salt in deoxygenated toluene in the presence of oleic acid and tridodecylamine and heated under a N_2 atmosphere up to 140 °C[46].

2.4 Chemical-Physical method

Chemical-physical methods are bottom-up approach where ions are dissolved and reduced in any type of solvents with various energy such as lasers or electricity. These methods can be used to synthesize mono and bimetallic NPs in the form of core-shell or alloyed structures.

2.4.1 Electro-chemical synthesis

This is a versatile method to synthesize mono and bimetallic NPs in solution and also both core-shell and alloyed structures. In this method, more reactive metals act as reducing agent for more noble metals. Bimetallic Pd-Ni, Fe-Co and Fe-Ni were synthesized by using bulk metal sacrificial anode in a single electrolysis cell.

2.4.2 Radiolysis

Radiolysis is an efficient method to generate both of mono and bimetallic transition metal clusters and Ag-Au[47], Pd-Ag[48], Pt-Ag[49], Pd-Au, Cu-Pd[50] and Pt-Au[51] systems have been reported.

In this method γ-ray radiation of water leads to solvate electrons which can be used to reduce metal ions to zero state then coalesce and formation of clusters. In this method the formation of core-shell or alloyed structures depends on γ radiation dosage, relative concentration of two metals, the rate of electron transfer and the nature of the ligands which are coordinate to metal ions. Immiscible elements require high dose of radiation for the formation of mixed pattern, although Cu-Pd, Ni-Pt and Pt-Ag formed with lower γ radiation dose, because the alloying elements are soluble in the host structures[52].

2.4.3 Sonochemical synthesis

Generally, in this method aqueous solution of metal precursors are reduced simultaneously by ultrasound irradiation. In prepared solution, capping agents or polymers are added for stabilization and control the size reduction. Sonochemical method is similar to wet chemical method and the only difference is in the reduction step where in wet chemical method, the metal ions are reduced by strong reducing agent like hydrazine, sodium borohydrate, H_2 gas or radiation. Sonochemical method is used to only synthesize ANPs (e.g. Au-Pd)[53], monometallic (e.g., Au)[54] systems and compounds (e.g., MoS_2)[55]. $Au_{core}Pd_{shell}$ was synthesized by inducing radiation to aqueous solution of Au(III) and Pd(II) ions by high-intensity ultrasound. This method leads to the formation of various morphologies in NPs which is the result of experimental condition such as the effect of stirring, microjet stream and shock wave. The following effects can be observed in sonochemical reactions and processes:

- Increase in reaction speed
- Increase in reaction output

- Switching reaction path way[97]

Here one can conclude that for elements with large redox potential difference, sonochemical method is a better candidate compared to co-reduction and successive method to synthesize ANPs. Also elements like Ag & Ni and Ag & Fe which are immiscible in bulk (at both liquid and solid state) can be alloyed by this method.

2.5 Conclusion

The choice for the method of synthesis of ANPs depends on the specific purpose (i.e. fundamental study or applied materials). Physical methods are more expensive and their processes are more controllable, making them suitable candidates for fundamental studies. On the other hand, chemical methods are simple and scalable, but controlling the process is challenging due to random nucleation and growth and other phenomenas such as Ostwald Ripening.

Refrences

[1] N. Toshima, T. Yonezawa, Bimetallic nanoparticles-novel materials for chemical and physical applications, New J. Chem., 1998, 1179-1201.
[2] T. Sugimoto, Fine particles: synthesis, characterization and mechanism of growth, surfactant science series, vol. 92, 1998.
[3] G. Schmid, Nanoparticles: from theory to application, Wiley, 2004.
[4] P. PrausI, M. Turicová, Preparation of silver-montmorillonite nanocomposites by reduction with formaldehyde and borohydride, J. Braz. Chem. Soc., 20(7), 2009, doi: 10.1590/S0103-50532009000700021.
[5] U. Nickel, A. Z. Castell, A Silver Colloid Produced by Reduction with Hydrazine as Support for Highly Sensitive Surface-Enhanced Raman Spectroscopy, Langmuir, 16 (23), 2000, 9087–9091.
[6] H. Bönnemann, R. M. Richards, Nanoscopic Metal Particles - Synthetic Methods and Potential Applications, Eur. J. Inorg. Chem. 2001, 2455-22480.
[7] H. Cuia, H. Liu, Synthesis of Bi_2Se_3 thermoelectric nanosheets and nanotubes through hydrothermal co-reduction method, J. Solid State Chem., 177, 2004, 4001–4006.
[8] X. Jiang, Q. Zeng, A self-seeding co-reduction method for shape control of silver nanoplates, Nanotechnology, 17, 2006, 4929–4935.
[9] Z. Liu, A. Kumbhar, Coreduction Colloidal Synthesis of III–V Nanocrystals: The Case of InP, Angew. Chem., 120, 2008, 3596 –3598.
[10] P. M. Arnal, M. Comotti, High-Temperature-Stable catalysts by hollow sphere encapsulation, Angew. Chem. Int. Ed., 45, 2006, 8224 –8227.
[11] Z. R. Dai, S. Sun, Phase transformation, coalescence, and twinning of monodisperse FePt nanocrystals, Nano. Let., 1, 2001, 443-447.
[12] K. Yu, Z. Wu, High-temperature-stable Au@SnO2 Core/Shell supported catalyst for CO oxidation, J. Phys. Chem. C, 112, 2008, 2244-2247.
[13] M. A. Watzky, R. G. Finke, Nanocluster size-control and "Magic Number" investigations. Experimental tests of the "Living-Metal Polymer" concept and of mechanism-based size-control predictions leading to the syntheses of Iridium(0) nanoclusters centering about four sequential magic numbers, Chem. Mater., 9, 1997, 3083-3095.
[14] B. P. Khanal and E. R. Zubarev, Polymer-Functionalized Platinum-On-Gold Bimetallic Nanorods, Angew. Chem. Int. Ed., 48, 2009, 1- 5.
[15] K. Torigoe, Y. Nakajima, Preparation and characterization of colloidal silver-platinum alloys, J. Phys. Chem.,97, 1993, 8304-8309.
[16] P. Braunstein, J. Rose, Metal clusters in chemistry, Wiely-VCH, 2, 1999, 616-618.
[17] K. Esumi, T. Tano, Preparation and Characterization of Bimetallic Pd-Cu Colloids by Thermal Decomposition of Their Acetate Compounds in Organic Solvents, Chem. Mat., 2, 1990, 564-567.
[18] J. S. Bradley, G. H. Via, Infrared and EXAFS Study of Compositional Effects in Nanoscale Colloidal Palladium-Copper Alloys, Chem. Mater., 8, 1996, 1895-1903.

[19] K. R. Harikumar, S. Ghosh, X-ray Photoelectron Spectroscopic Investigations of Cu-Ni, Au-Ag, Ni-Pd, and Cu-Pd Bimetallic Clusters, J. Phys. Chem. A, 101, 1997, 536-540.
[20] P. Y. Silvert, R. Herrera-Urbinab, Preparation of colloidal silver dispersions by the polyol process Part 2.-Mechanism of particle formation, J. Mater. Chem., 7, 1997, 293–299.
[21] D. Kodama, K. Shinoda, Synthesis of Fe-Co alloy particles by modified polyol process, IEEE Transactions on Magnetics, 42, 2006, 2796-2798.
[22] C. Liu, X. Wu, Polyol process synthesis of monodispersed FePt nanoparticles, J. Phys. Chem. B, 108, 2004, 6121-6123.
[23] C. N. Chinnasamy, B. Jeyadevan, Polyol-process-derived CoPt nanoparticles: Structural and magnetic properties, J. Appl. Phys., 93, 2003, 7583-7585.
[24] Y. T. Chen, W. Zhang, Polyol process to large-scale synthesis of Cu_2O with disk-like structure, Chinese Chem. Lett., 16, 2005, 245-248.
[25] N. I. Ivanoval, D. S. Rudelev, Synthesis of barium sulfate nanoparticles in water-in-oil microemulsion systems, Colloid Journal, 63,2001, 714-717.
[26] D.H. Chen, S.H. Wu, Synthesis of nickel nanoparticles in water-in-oil microemulsions, Chem. Mat., 12, 2000, 1354-1360.
[27] X. Zhang, K.Y. Chan, Water-in-oil microemulsion synthesis of platinum-ruthenium nanoparticles, their characterization and electrocatalytic properties, Chem. Mater., 15, 2003, 451-459.
[28] F. Grasset, R. Marchand, Synthesis of CeO2@SiO2 core–shell nanoparticles by water-in-oil microemulsion. Preparation of functional thin film, J. Colloid and Interface Science, 299, 206, 726-732.
[29] S. Mann, Biomineralization: Principle and concepts in bioinorganic materials chemistry, Oxford University Press:Oxford, 2001.
[30] B. Mann, Biomimetic materials chemistry, VCH: New York, 1996.
[31] R. Brayner, T. Coradin, Algal polysaccharide capsule-templated growth of magnetic nanoparticles, New J.Chem. , 2005, 29, 681–685.
[32] H. B. Liu, G. Canizal, Structural selection and amorphization of small Ni-Ti bimetallic clusters, J. Phys. Chem. B, 110, 2006, 12333-12339.
[33] L. Mai, W. Guo, Fabrication and Properties of VOx-Based Nanorods, J. Phys. Chem. C, 112(2), 2008, 423–429.
[34] Y. Zhao, Z. Zhang, Preparation of tin nanoparticles by solution dispersion, Mat. Sci. and Eng. A, 359, 2003, 405-407.
[35] Y. Zhao, Z. Zhang, A novel solution route for preparing Indium nanoparticles, J. Phys. Chem. B, 107, 2003, 7574-7576.
[36] Y. Zhao, Z. Zhang, Synthesis of In–Sn alloy nanoparticles by a solution dispersion method, J. Mater. Chem. , 14, 2004, 299–302.
[37] D. Zitoun, C. Amiens, Synthesis and magnetic properties of nanoscale bimetallic Co_1Rh_1 particles, New Journal of Physics, 4 ,2002, 77.1–77.11.
[38] K. R. Jeon, C.Y. Park, Epitaxial Growth of MgO and CoFe/MgO on Ge(001) Substrates by Molecular Beam Epitaxy, DOI: 10.1021/cg901380b.
[39] S. Charnvanichborikarn, J. Wong-Leung, Self-assembled Au nanoparticles in SiO_2 by ion implantation and wet oxidation, J. Appl. Phys. , 106, 2009, 103526-103526-8.

[40] X.H. Xiao, F. Rena, Formation of aligned silver nanoparticles by ion implantation, Mat. Lett., 61, 2007, 4435–4437.
[41] C. W. White, S. P. Withrow, Formation of Ferromagnetic FePt Nanoparticles by Ion Implantation, Mat. Res. Soc. Symp. Proc., 704, 2002, W.7.7.1-W.7.7.6.
[42] X. Xiang, X. T. Zu, ZnO nanoparticles embedded in sapphire fabricated by ion implantation and annealing, Nanotechnology, 17, 2006, 2636–2640.
[43] H. H. Liebermann, Processes and structures properties applications, Marcel Dekker, 1993, p.8-9.
[44] A. Ziabicki, Fundamentals of Fiber Formation, Wiley, New York (1976), ISBN 0471982202.
[45] N. S. Sobal, M. Hilgendorff, Synthesis and structure of colloidal bimetallic nanocrystals: The non-alloying system Ag/Co, Nano. Lett., 2, 2002, 621-624.
[46] N. S. Sobal, M. Hilgendorff, Synthesis and structure of colloidal bimetallic nanocrystals: The non-alloying system Ag/Co, Nano. Lett., 2, 2002, 621-624.
[47] M. Treguer, C. de Cointet, Dose rate effects on radiolytic synthesis of Gold–Silver bimetallic clusters in solution, J. Phys. Chem. B, 102, 1998, 4310–4321.
[48] C. M. Doudna, M. F. Bertino, Structural investigation of Ag-Pd clusters synthesized with the radiolysis method, Langmuir, 18, 2002, 2434-2435.
[49] C. M. Doudna, M. F. Bertino, Radiolytic synthesis of bimetallic Ag-Pt nanoparticles with a high aspect ratio, J. Phys. Chem. B, 107, 2003, 2966-2970.
[50] S. D. Oha, M.R. Kim, Radiolytic synthesis of Pd–M (M = Ag, Au, Cu, Ni and Pt) alloy nanoparticles and their use in reduction of 4-nitrophenol, J. Ind. Eng. Chem., 14, 2008, 687–692.
[51] K. Patel, S. Kapoor, Synthesis of Au, Au/Ag, Au/Pt and Au/Pd nanoparticles using the microwave-polyol method, Research on Chemical Intermediates, 32, 2006, 103-113.
[52] J. Belloni, M. Mostafavi, Radiation-induced synthesis of mono- and multi-metallic clusters and nanocolloids, New J. Chem., 22, 1998, 1239-1255.
[53] Y. Mizukoshi, T. Fujimoto, Characterization and catalytic activity of core-shell structured Gold/Palladium bimetallic nanoparticles synthesized by the sonochemical method, J. Phys. Chem. B, 104, 2000, 6028-6032.
[54] K. Okitsu, M. Ashokkumar, Sonochemical synthesis of gold nanoparticles: Effects of ultrasound frequency, J. Phys. Chem. B, 109, 2005, 20673-20675.
[55] M. M. Mdleleni, T. Hyeon, Sonochemical synthesis of nanostructured molybdenum sulfide, J. Am. Chem. Soc., 120, 1998, 6189-6190.

Chapter 3

3. Characterization methods for ANPs

Alloy nanoparticles (ANPs) can be characterized by a variety of experimental techniques including X-Ray Diffraction (XRD), Transmission Electron Microscopy (TEM), UV Spectroscopy and Differential Scanning Calorimetry (DSC). The following chapter gives brief overview of the most common knowledge about these techniques.

3.1 Analysis by X-ray diffraction

3.1.1 Introduction

X-rays were discovered by Roentgen, a German physicist, in 1895 and the name was chosen because of their unknown nature. X-ray diffraction technique was instantly developed for use in radiography (with the resolution of 10^{-3} cm) by physicians and engineers without precise understanding of their nature. In 1912 the exact nature of x-ray was discovered as an electromagnetic wave with the wavelength of approximately 1 Å and also was proven that it can be used for investigation of the fine crystalline structure of materials.

Thereafter, x-ray diffraction has been used to study the structure of matter and nowadays further information such as percentage of crystallinity, lattice spacing, particle size, information about the phase (such as mixing or degree of segregation), and quantitative chemical composition can be extracted by this method[1]. Depending on the portion of the phase in the specimen from intensity of XRD pattern, quantitative analysis of the sample is possible[2]. X-ray diffraction analysis is useful whenever it is necessary to know the state of the chemical composition or the particular phases that exists in the sample[3]. X-ray

diffraction is known as a nondestructive method which is also fast and requires only a small amount of the sample and after performing XRD, sample is reusable for further characterization. Although the interpretation of the XRD data can be complex, it is still a powerful method to determine all the characteristic of crystal structures and phases for both micro and nano-structured materials. Nanostructures could show limited number of peaks in their respective X-ray spectra; in this case it is better to perform chemical analysis before determination of phase and structure. Fewer peaks can be results of:

1- Low concentration of chemical elements (concentration can strongly impact the intensity and the number of peaks)
2- Formation of amorphous phases along with the crystal structure.
3- If surfactant or capping agents are dense organic molecules, then significant absorption of the x-ray is possible which may cause damping in the pattern.

3.1.2 Qualitative analysis

The collection of the XRD patterns was initiated by Hanawalet, Rinn and Frevel at the Dow Company. They obtained and classified diffraction data for nearly 1000 substances in 1941 which became the great resource for the technical community. This data base has been used to determine the crystalline structure of materials and have been developed for other materials each year under the title of ICCD pdf-4[4]. Hanawalt and Fink are two methods available for quantitative analysis of XRD pattern manually and Jade software is generally used to identify the phase. In Jade software, search match can be performed based on intensities, *d* spacings or both of them. In this thesis, search match is based on

only d spacing (Fink method), since intensities in XRD pattern of nanostructures can be affected by other factors rather than simply the atomic positions.

3.1.2.1 Hanawalt method

Hanawalt developed a method to characterize each substance by d values of the three strongest intensities. In other words, d_1, d_2, and d_3 and their relative intensities are sufficient to characterize an unknown pattern[5,6]. One of the challenges in the characterization of nanostructures with XRD is that less peaks observable in the XRD patterns of materials which makes identification vague. Furthermore, intensities of XRD pattern may not be representative of atomic position in the unit cell, because of other effects such as preferred orientation. Therefore, Hanawalt method is not a reliable method for the indexing of nanostructure materials.

3.1.2.2 Fink method

Fink method is a numerical method which relies on the d spacings rather than the intensities and originally was designed for indexing of the electron diffraction patterns. This method is a reliable method for the characterization of nanostructures, because intensities in their XRD pattern do not directly correspond to the atomic positions[7]. Therefore, in this thesis, since only two to five peaks are usually observable in the XRD patterns (of nanostructures); I considered only the d spacing values for determination of the phases, and not the intensities[1].

3.1.3 Optimization of powder diffraction

Good data collection in XRD is a direct result of conscientious sample preparation, accurate instrumentation, and appropriate data collection condition. For sample configurations, the following possibilities should be considered:

- Fluorescence samples: when Fe, Co and Mn are samples and x-ray hits the sample, radiation other rather x-ray makes the analysis of data complicated.
- Sample composition
- Preferred orientation
- Peak overlaps
- Sample roughness/ particles size: may cause a shift in XRD pattern.
- Crystallite size
- Percent crystallinity

Each set of the above conditions or characteristics require different conditions in XRD data collection. Performing the pre-scan can lead to minimal timing to reach better and unambiguous results[8].

3.1.4 Preparation of samples for XRD

The preparation of samples was carried out on glass slides and also repeated on silicon. Below are the advantages and disadvantages of using glass slides:

Advantages

- Elimination of contamination from previous experiment, since each slide is used only once.
- Inexpensive.

Disadvantages

- If the sample is transparent (low absorption coefficient), it may be affected by the background interference from the holder.
- All the solvent must evaporate; otherwise the peak from the solvent might appear in the pattern which makes the analysis of the pattern complex.
- Difficulty with powder samples (because achieving a flat surface is difficult).

Sample preparation with low concentration solution is time consuming and requires many times of drop casting the solution. On the other hand, after evaporation of the solution, a preferred orientation may take place, especially, when the surfactant still remains in the solution. Unfortunately, there are no criteria to measure the optimum thickness for XRD samples. In samples with small thicknesses, peaks cannot be detected due to high noise to signal (peak) ratio. On the other hand, thick samples cause shifts along 2θ axis in XRD patterns. The surface of the sample must be exactly at the same level as the edge of the holder, otherwise, peak positions will be shifted towards the lower 2θ and broaden asymmetrically. It is more convenient to prepare a sample on zero background holders, because amorphous background (which shows up in glass slides) can be removed. This holder can be made of silicon which is grown parallel to (510) plane and has no diffraction reflections in the typical scan range. One of the disadvantages of this holder is high sensitivity to impurities. Improper cleaning from previous runs can easily lead to cross-contamination for subsequent samples.

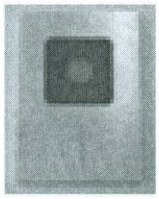

Figure 3.1: Zero background holder which is made of silicon grown parallel (510) direction and doesn't show any peaks in the range of 2θ = 3-90.

3.1.5 Common errors found in XRD data collection

Careful sample preparation can minimize the below errors:

- Sample displacement: can cause shift ~0.01° (2θ) for every ~60 μm elevation offset.
- Sample transparency
- Sample particle size: Particles must be small enough to allow x-rays to penetrate the core and packed to provide a flat surface. To minimize re-absorption of reflected x-rays within the sample, the general rule is that powder particulate sizes should be <45 μm diameter (325 mesh screen or finer). If the sample has heavy elements, 500 mesh or smaller particle size may be necessary.
- Preferred orientation: The sample's crystals line up (or stack) in such a way that certain reflections appear more intense than normal which is commonly observed in clays, mica, graphite and thin film samples obtained by evaporating a solvent to dryness.
- Substrate interface

Instrument choice such as correct starting and stopping angles, step size or dwell time and slit choice can minimize these errors.

3.1.6 Optimization of measurement in X-Ray diffraction

X-ray diffraction is a known method for the characterization of microstructures. XRD is a powerful method for the characterization of nanostructures and certain optimization may help to overcome the challenges in the characterization of nanostructures. General guidelines are as below:

1. Wide slits give higher intensity, but lower resolution.

2. Narrow slits give lower intensity, but higher resolution.

3. Use narrow slits, if the sample is very small.

Four optional slits are 1.2 mm, 2.0 mm, 5.0 mm, and 10.0 mm (OPEN), [default] = 10.0 mm, compared to smaller slits, using larger slits will cause:

a. Higher intensity measurement, because more sample is irradiated.

b. Broader peaks and loss of peak profile sensitivity due to scattering effects caused by more coincident x-rays.

c. Higher background interference from sample holder, if sample size is small.

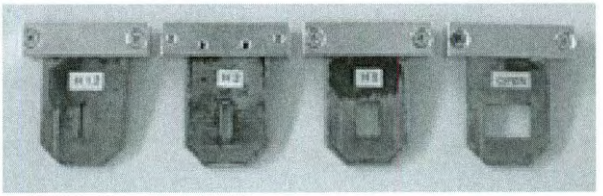

Figure 3.2: different slit sizes from left to right 1.2 mm, 2.0 mm, 5.0 mm, and 10.0 mm (OPEN).

Figure 3.2 shows different slit sizes. To achieve higher intensity peak, higher slit size is required especially with zero background holder, although it is not a good option with glass slide. It is better to use 1.2 mm slit with glass slide.

Pre-Scan is suggested for minimization of the time and cost and it is wise to never make an assumption for data collection (phase determination) even based on literature. Pre-Scan can be performed between 2θ=2-70° with step width 0.05 at 20°/minutes for small samples or 7°/minutes for smaller samples. For better data collection it is better to:

- Store the data as count mode not cps
- Use largest divergence slit, scatter slit, receiving slit and standard soller slit pairs to optimize intensity for pre-scan.
- Find the full width at half maximum (FWMH) of narrowest peak in pre-scan pattern, divide by 5 or 7 and find the appropriate step size.
- Step size and receiving slit are hand in hand. There is a table on each Dmax which shows that appropriate receiving slit can be found for the calculated step size from FWMH determined by pre-scan pattern.

Smaller step size usually gives more noise in the pattern. Pre-scan pattern could be analyzed with Jade software and in view (window menu); choose zoom in→data points which helps to differentiate noise and peaks from each other.

Receiving slit is the best parameter to achieve better resolution and better peak to background ratios. Intensity is sacrificed with smaller slit and typical choices in measurement are 0.6mm, 0.3mm and 0.15mm. Table 3.1 shows the minimum receiving

slit value suggested by Rigaku when the step size is known. Table 3.2 depicts the instrument setting for the all our XRD measurements of alloy nanoparticles .

Table 3.1: Minimum recommended step size for specific slit width.

Slit Width Slit [mm]	Minimum Recommended Step Size [2θ]
0.05	0.002°
0.15	0.005°
0.3	0.01° **[default]**
0.6	0.02°
1	0.034°
2	0.068°
10 (open)	0.340°

Table 3.2: shows instrument setting for XRD measurement of alloy nanoparticles in this thesis.

Div. Slit.	Reg. Slit	Sct. slit	Slit size
1 deg.	0.3	1 deg.	1.2 mm for glass slide 10 mm for Zero Background

3.2 Analysis by Transmission Electron Microscopy

3.2.1 Introduction

Historically, TEMs were developed because of the limitation in the resolution of the light microscope imposed by the visible light (with wave lengths of 380-740 nm). Louis and Broglie (1925)[9] first theorized that the electron had a wave characteristic with a wavelength less than visible light in 1925. Davisson and Germer[10] independently carried out their classic electron diffraction experiments which demonstrated the wave nature of

electrons. Shortly thereafter, the idea of an electron microscope was proposed by Knoll and Ruska[11] in 1932 and this was a key step for Ruska to receive the Nobel Prize in late 1986. TEMs were developed by commercial companies only four years later. The first TEM under the name of Metropolitan Vickers EM1 was built in the UK in 1936, but apparently it did not work well and the regular production started by Siemen and Halske in Germany. TEMs became widely produced from different sources (JEOL, Hitachi, Philips and RCA) after World War II. Thomas in 1962 pioneered the use of TEM for the characterization of materials in the United State[12].

It is important to determine the degree of aggregation, size, size distribution, morphology and structure of NPs with various microcopies. Electron microscopy is particularly useful for nanoparticles (NPs) and alloy nanoparticles (ANPs).

3.2.3 General information about TEM Grids

To prepare TEM sample, grids need to have a support to hold the specimen in place above the objective lens. Some samples have their own support, and grid support is not necessary for preparation of the sample on the grid. The selection of the "right" support film has never been an easy exercise, even for the most experienced TEM users. The only way to really determine which support film is the best for a particular application is to explore various films. As an example for TEM characterization of carbon based materials, lacy grid can be the better option compared to carbon coated grids (because contrast will be minimum). All the grids are 3.05 mm diameter, but thickness can vary within the mesh size change. Copper grids are the least expensive and are extensively used by coating carbon or formvar. Carbon and formvar grids are well known for their

stability in high beam. In this thesis, holey carbon grid was used to characterize ANPs. Nickel grids are magnetic and they won't stick to tweezers and have a high resistance to chemical attack. For carbon based material, usually lacy grids (polymer grids) are the better option, because high contrast can be achieved. Molybdenum grids are suitable for high temperature study and they are available in any coating. Polymer coating is not the best option for study at high temperatures, because of degradation during the heating process. Silicon nitride membrane window grid might be the better choice, because one can do in situ heating experiment beyond 1000℃ without membrane rupturing. These grids are the best candidates for studying a sample under Cryo TEMs on liquid.

In this thesis, TEM was used as the primary tool to characterize nanostructures and it is required to choose an appropriate technique, magnification calibration and grid to achieve the best quality characterization. Different techniques in TEM for characterization of nanostructure are Bright Flied Imaging (BFI), High Resolution Transmission electron Microscopy (HRTEM), Scanning Transmission Electron Microscopy (STEM) and High Angle Annular Dark field (HAAD), each of them providing specific information. The motivation for this discussion here is not to provide new or advanced details about this method, but clearly discuss the strength and weakness for better characterization in future and also overcome the challenges involved in this method for further improvement based on theory. Recently, remarkable progress in transmission electron microscopy (TEM) enables scientists to study not only structure, but also composition of isolated particles at the specific temperatures. Our knowledge such as the structure and the alloying process of two component alloy particles are due to in-situ TEM studies. Currently, TEM is the

only characterization method where the formation and stability of two (or multi) components isolated nanoparticles can be studied as a function of temperature, diameter and composition. Further development and proposition of novel methods are required along with the current characterization methods to study stability and phase diagram of nanoscale systems. Blow is brief discussion about the different techniques in TEM.

BFIs are generated using transmitted beam. The imaging needs high voltage and short exposure time. The image resolutions are improved at the cost of contrast[13]. BFIs are taken by inserting an objective aperture that is small enough to allow only the direct beam to pass through (to achieve better image contrast). HREM imaging is similar to BFI; however, a large-objective aperture or the removal of the objective aperture is required such that both the direct beam and Bragg-diffracted beams are used to generate the image. HRTEM is usually used to details at the atomic scale such as planes and columns of atoms in projection. The limited contrast between the nanostructure and background (grid) is one of the principal difficulties in accurately assessing the particle size distribution. However, because of unavoidable imperfections in the manufacture of electromagnetic lenses, most conventional TEMs suffer from a variety of aberrations that diminish the obtainable resolution. A few of the major ones are spherical aberration, chromatic aberration, and astigmatism.

3.3 UV spectroscopy

Optical properties of clusters mirror their electronic structure, geometry and their size. For noble metal clusters, the main feature of the optical response to excitation by light is an absorption band in the UV-visible range related to surface plasmon resonance. The

most immediate observable property of noble metal NPs dispersions is their color[14]. Faraday showed that classical Au sol is clear ruby-red color. Au, Ag and Cu (Group 1B metals) NPs have the characteristic colors related to their particle size and shape. Thus, for these metals, observation of UV-Vis spectra can be a useful complement with other methods in characterizing metal particles. The optical properties (in particular the surface plasmon resonance) are sensitive to the chemical composition and degree of ordering of bimetallic NPs, especially for the noble metals[15]. Changes in UV-vis spectra can also be used as a quick test whether binary alloys are formed or not. Other complementary characterization methods are required to determine whether alloying takes place[16].

3.4 Differential scanning calorimetry (DSC)

The history of caloric measurement goes back to the middle of 18th century and today with new DSC instruments, an accurate measurement can be performed compared to that of classic calorimeter instrument. The purpose of calorimetry is the measurement of exchanged heat. The exchanged heat causes a local temperature change along its path in the body of the material or phase transformation. In this measurement, the temperature difference between the sample and the reference is investigated as a function of temperature. The main advantage of this method is ease and simplicity of operation, but experimental manipulation inside the closed crucible is not possible. After this characterization, the sample is not re-usable for other characterization. According to the International Confederation for Thermal Analysis and Calorimetery (ICTAC), the definition of Differential Scanning Calorimetery (DSC) is as following: A technique in which the heat flow rate versus temperature change in the sample (compared to that of reference) is recorded while the temperature of the sample in specific atmosphere is

programmed and our measurement is in N_2 atmosphere. DSC measurement is applied in the following fields:

- Thermal stability investigation
- Evaluation of phase diagrams
- Purity determination
- Investigation of kinetics
- Comparison (relative) measurements (quality control, identification of mixtures)

In DSC, generally the measured signal is proportional to the heat flow rate. This curve or any derivative of that shows the heat of transformation or reaction or any change in heat capacity of the sample. Below is some general information about DSC which each user is required to have before starting to use this knowledge. The DSC curve reveals the information such as the melting point and behavior of the phase transformation. These investigations are more meaningful along with other structural analysis such as hot stage microscopy[17], infrared spectroscopy and X-ray diffraction. Counter part of melting is freezing and although freezing is complicated, there is general agreement about its essential features. Melting is still a mystery and opinions about its origin abound, but normal melting is initiated by continuous vibrational lattice instability at solid surface or solid-solid surface. In the DSC, a second run is recommended to do so to understand whether the phase behavior of a sample is reversible[18]. The second run in some systems shows the melting peak of metastable phases, which is the one of the main problems encountered in determination of phase diagram. The heating rate is one of the important parameter in DSC measurement, because the rate of transformation from metastable to stable phase is low in solid phase. At high heating rate (> 20 $Kmin^{-1}$) the formation of

stable phases may not happen, thus for equilibrium phase transformation low heating rate is required. Moderate heating rate (ca. 5K min^{-1}) could be the best rate for equilibrium transformation as the sample reaches some intermediate state.

Generally, two different types of differential scanning calorimeters are available:

- The heat flux DSC
- The power compensation DSC

Both types of above DSC have a same principle as below. Both measurements are based on the value difference between the sample and reference and are reported as a signal of measurement.

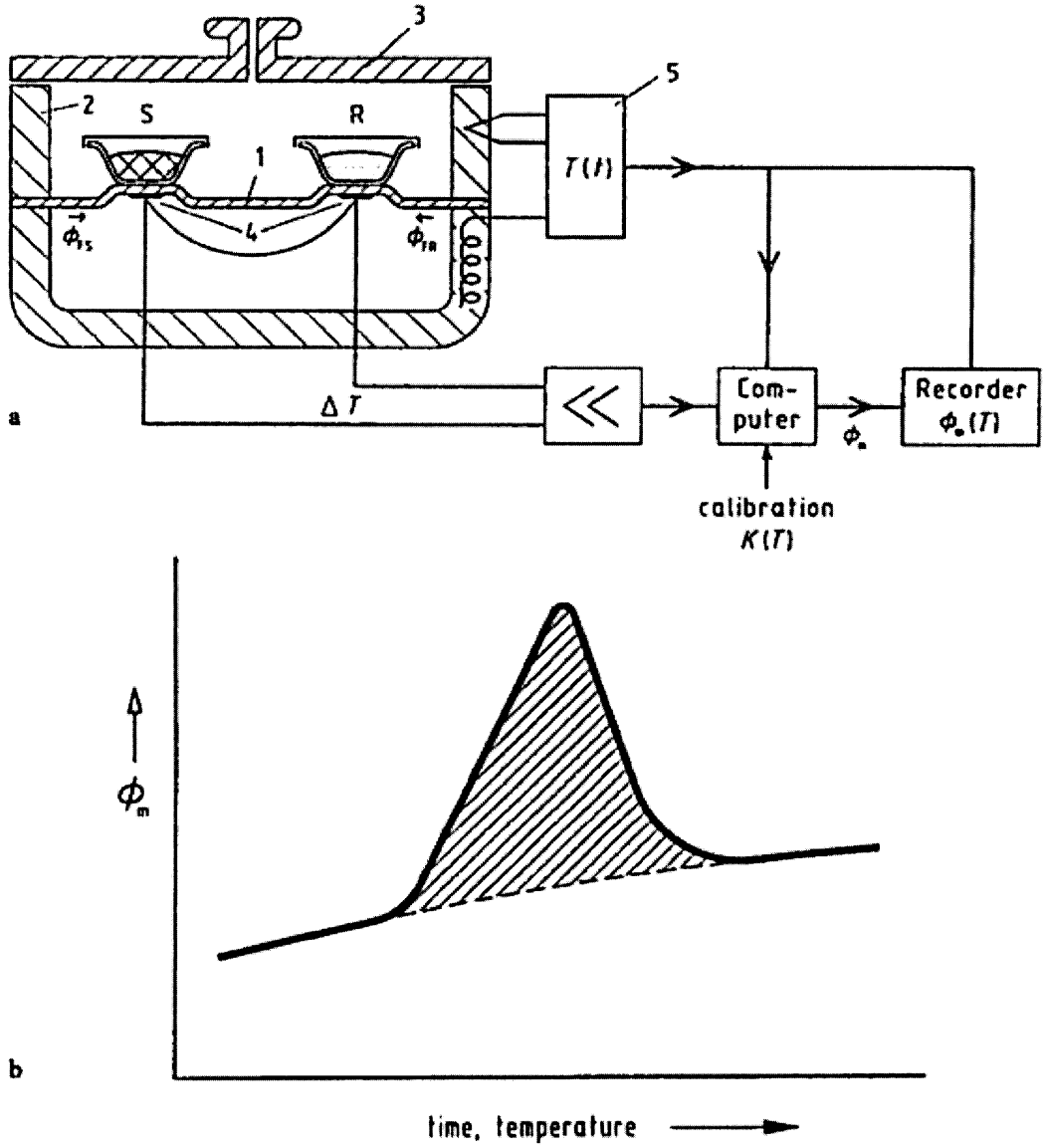

Figure 3.3: a) Different part of disk type DSC measuring system 1 Disk, 2 Furnace, 3 Lid, 4 Differential thermocouples, 5 Programmer and controller, S crucible with sample, R crucible with reference sample, Φ_{FS} heat flow from furnace inside the instrument to sample, Φ_{FR} heat flow from furnace to reference sample, Φ_m measured heat flow rate (Subtract Φ_{FS} from Φ_{FR}), K calibration factor. b) Heat flow measurement (Φ_m) from set up in part a[19].

The measurement in this study was carried out in Q-600 simultaneous TGA/DSC from TA instrument. Aluminum pans were used for DSC measurement and the empty one as a reference. DSC was used for the determination of ANPs melting point by the deposition

of concentrated ANPs solution in Al pans. When the system is programmed and starts to run, the furnace is heated and heat moves from disk through the sample. When the heat distributes (ideally symmetrically) in the sample and reference, the transition would be in steady-state equilibrium. In this case, the difference between the heat flow rate in the sample and the reference is proportional to the change in the temperature of the sample:

$$\Phi_{FS} - \Phi_{FR} \sim -\Delta T; \qquad \Delta T = (T_S - T_R)$$

Generally, thermal measurement of nanostructures and microstructures are the same and no specific optimization is required for nanostructured materials. The only challenge occurs in sample preparation of the nanostructure, since colloidal solutions are highly dilute and heating leads to aggregation and reduction of surface area. The surface area affects the melting point directly and will be discussed in the next chapter. The best way to prepare DSC sample is to drop-cast the concentrated solution in the Aluminum pans; although this process is time consuming, it can be a way to preserve the high surface area of nanostructures.

3.5 Conclusion

Among all the methods for the characterization of two or multi-components alloy nanoparticles, only TEMs enable the study of structure and their chemical composition at the specific temperature. Other methods need complementary methods to prove whether alloying takes place. This capability opens a wide unexplored research field on the structural stability of two or multi-component nanostructure systems. Most of the current knowledge on the phase stability of two or multi-components alloy nanoparticles has been carried out by in situ TEM studies and recent improvement in TEMs (such as

Aberration-corrected TEM[20] , 3D imaging and improvement in the resolution of STEM[21]) gives scientists better chance to explore novel structures of ANPs with clarity. Fifty years after Feynman's famous speech, great progress has been made towards the invention of novel instruments such as the scanning tunneling and atomic force microscopy to manipulate nanostructures, but still challenges remain in the study of the phase stability of nanostructures[22].Therefore, novel characterization methods enable an in-depth study of two (or multi-) component nanostructures leading to the transformation of nanoscience from laboratory scale to useful materials.

References

[1] Li-ling Ooi, Principles of x-ray crystallography, Oxford; New York: Oxford University Press, 2010.
[2] V. Vassileva, E. Gatev, X-ray quantitative phase analysis of anorthite in electric insulation ceramics, 9, 1990, 741-742.
[3] B.D. Cullity, Elements of X-ray diffraction, Addison Wesley Publishing Company INC., 1977.
[4] J. Faber, ICDD's new pdf-4 organic database: search indexes, full pattern analysis and data mining, Crystallography Reviews,10, 2004, 97- 107.
[5] J.D. Hanawalt, and H.W. Rinn, Ind. Eng. Chem. Anal. Ed. 8, 1936, 244-250.
[6] J. D. Hanawalt, H. W.Rinn and L. K. Frevel, Ind.Eng. Chem. Anal. Ed. 10, 1938, 457-512
[7] E. Lifshin, X-ray Characterization of materials, Wiley-VCH, 1999, 68-70.
[8] C. Suryanarayana, G. Norton, X-ray diffraction; practical approach, Plenum Press, New York, 1998, 73-93.
[9] L. de Broglie, Ann.de Physiques, 3, 1925, 22.
[10] G. Davisson, L.H. Germer, Phys. Rev., 30, 1927, 705.
[11] M. Knoll, E. Ruska, Z. Physik, 78, 1932, 318.
[12] D. B. Williams, C. Barry Carter, Transmission Electron Microscopy, 1, 1996, 1-2.
[13] T. Goringe, Transmission electron microscopy of materials, Wiley, 1979, 39-40.
[14] U. Kreibig, M. Quinten, Clusters of atoms and molecules, H. Haberland, Springer-Velag, Birlin, 1994, 11, 321-324.
[15] J.S. Bradly, Clusters and colloids: From theory to applications, VCH: Weinheim, 1994.
[16] U. Kreibig, M. Vollmer, Optical properties of metal clusters, Springer-Verlag, Berlin, 1995.
[17] I. M. Vitez, A.W. Newman, The evolution of hot-stage microscopy to aid solid-state characterization of pharmaceutical solids, Thermochimica Acta, 324, 1998, 187-196.
[18] W. Hemminger, G. Hohne, Calorimetry,; Fundamentals and Practice, Verlag Chemie, 1984.
[19] G. Hohne, W. Hemminger, Differential scanning Calorimetry; an introduction for practitioner, Springer, 1996.
[20] B. Janssens, Aberration-corrected TEM; A New Wave of In situ Investigations in Materials Science, Imaging & Microscopy, 9, 2007, 42-43.
[21] W. G. Morris, S. Madras, An order of magnitude improvement in STEM resolution: Wavelength high-energy electron localization, Microscopy Today, 18(2), 2010, 38-40.
[22] Plenty of room, plenty of history, Nature Nanotechnology, 4, 2009, 783-784.

Chapter 4

4. Characterization of low melting point Au-Sn alloy nanoparticles (ANPs)

4.1 Introduction

Scientific community have made a tremendous progress in the advancement of the semiconductor electronics and their development in the industries while the essential requirements for interconnects remain unchanged. Traditionally, Pb-Sn alloys have been used as electrical interconnections, because of their low cost and excellent soldering properties. The Sn-Pb solder alloy is a simple eutectic (Sn- 37% Pb) system with the melting temperature of 183°C by reduction of almost 50°C from pure Sn at 232° C[1]. Solder materials are available in variety of shapes for electronic interconnection such as paste, wire, ball, bead, ingot and ribbon/foil. The solder paste is a mixture of over 90% pre-alloyed solder powders and a chemical flux-vehicle (electrically conductive adhesive (ECA)) that has a creamy, butter-like flexibility[2]. ECA consists of a polymeric resin (such as epoxy, silicone, or polyimide) that provides physical and mechanical properties including adhesion, mechanical strength and impact strength and metal filler (such as silver, gold, nickel or copper) that conducts electricity[3].

Lead, a major component of Sn-Pb alloy solder has been a threat to the consumer health and environment. Most electronic products have a very short service life (e.g., cell phones, pagers, electronic toys and etc.) which often ends up in landfills in just a few months or years. Lead from discarded consumer electronic products in landfills can leach into underground water and eventually into the drinking water system this is still under debate in scientific community. On the other hand, the recycling of lead-containing consumer electronic products has been proven to be very difficult. Therefore, the

electronic manufacturers would prefer to use lead-free interconnect materials in manufacturing of electronic devices. Sufficient knowledge about the reactions during the soldering process, information from phase equilibria data and thermodynamic calculations has proven to be important tools in the design and understanding of new lead-free solder alloys[4].

4.2 Lead restriction and other regulation influences

Industrial domain is governed by the laws of the country, state or region in which they are located. Certain limitation and restrictions based on the laws are imposed on industrial activities such as disposing, recycling hazardous and solid waste. Technologist and engineers are addressing important changes in the chemical content of electronic products based on the state laws. Restriction of hazardous substances (RoHS) is the most important piece of legislation adopted by European Union which affects electronic products. Effective since July 1, 2006 the electronic products placed in the market must not contain more than restricted values and maximum concentrations of hazardous substances. That is the reason some industries find the European market uneconomical[4]. Table 4.1 summarizes hazardous substances and maximum allowable concentration of them.

Table 4.1: Maximum concentration values for RoHS restricted substances[5].

Restricted substance	Maximum concentration values (MCV)
Lead and its compounds	0.1% by weight
Mercury and its compounds	0.1% by weight
Hexavalent chromium and its compounds	0.1% by weight
Cadmium and its compounds	0.01% by weight
Polybrominated biphenyls (PBBs)	0.1% by weight
Polybrominated diphenyl ethers (PBDEs)	0.1% by weight

Japan initiated the voluntary reduction of hazardous substances from their products placed in the world market. The Japanese government reported in 2005 a series of studies focused on information exchange related to the RoHS restricted substances. This led to the Japanese industry to arise as a leader in creating standardized chemical contents for limited set of products. In the United States, California was the first state that addressed both recycling (through the collection fee at the point of purchase) and restricting hazardous substances through the partial implantation of RoHS at the beginning of 2007. 37 other states have proposed or passed environmental legislations in a similar manner. In Canada similar to the United State, there are no legislations and at least in six provinces, efforts are ongoing since 2007. In China, a version of RoHS has been developed by the Ministry of Information Industry (MII) and is officially called 'Management Method on

Controlling Pollution from Electronic Information Products'. The law was officially announced in February, 2006 and March 1, 2007 was the effective date of implementation for some requirements such as restricted substances, recyclability disclosure, packing description and labeling. In Mexico, a change in environmental legislation has started since 2007 modeled after the United States.

4.3 Lead-free soldering

A variety of lead-free solder alloys have been investigated as potential replacements for Sn-Pb solders. The nontoxic lead-free candidate should satisfy the following criteria:

1) Being plentiful in supply
2) Be wettable
3) Possess melting and solidifying temperature not higher than Pb-Sn alloy
4) Possess strength and toughness
5) Be highly conductive
6) Cost the same as Pb solders[6].

Several Pb-free systems have been studied including Sn-Bi, Sn-Zn, Sn-Ag, Sn-Cu, Sn-Ni, Sn-Au, Sn-Sb and Sn-In[5]. Sn-Bi and Sn-Zn are better potential candidates among other Pb-free solder systems because they do not form any intermetallic compounds in their solid solution, but Bi is an expensive element and Zn is prone to oxidation. Several methods have been used to produce solder NPs including gas atomization[7], mechanical alloying (MA)[8] and electroplating[9,10,11]. However, these methods produce solder particles with relatively large sizes. Behaviors of Sn-Au[9,10,11], Sn-Ni[12,13], and Sn-Cu[14] alloys are similar in that during alloying process variety of intermetallic compounds (IMC) can for

making them not very suitable for soldering application. Solubility of Bi in Sn is high and at the eutectic point, it has a low melting point at 139° C[15] which is not suitable for electronic packaging. Study on phase formation of Bi-Sn ANPs by in situ transmission-electron microscopy revealed that the phase equilibrium of these particles is significantly different from that of the corresponding bulk materials and the melting point of 10 nm Sn-Bi ANPs decreases to approximately 105° C[16]. In this case Sn-Bi ANPs are not suitable candidates for lead-free soldering for high temperature electronic packaging. Figure 4.1 shows superimposition of the phase diagram of the Sn-Bi at bulk and nano-scale (for d=10nm particles). Nano-phase diagram compared to that of the bulk decreases in transition temperature and shifts towards the higher composition of Sn.

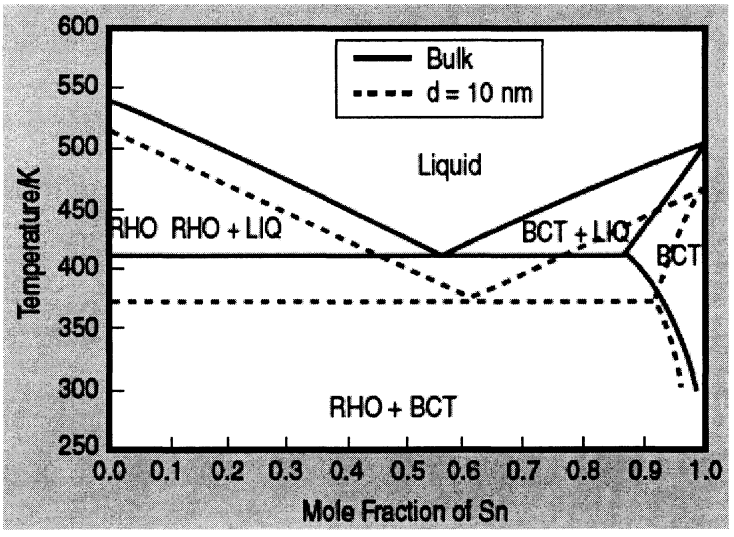

Figure 4.1: The phase diagram of the Sn-Bi system in which (a) the bulk phase is shown with a solid line and the nano phase is shown with a dashed line for 10 nm Sn-Bi alloy particles[16].

The binary nanophase diagram of the other solder systems have not been developed yet and the bulk phase diagram can be used as a source of comparison of microstructure with

phenomena which was observed at nano-scale, although the phase diagram at nanoscale can be substantially different from the bulk. When nanosystem goes through phase transition, the equilibrium phase diagram is shifted towards higher Sn composition compared to that of the bulk.

Jiang et al[17] synthesized Ag-Cu alloy nanoparticles by polyol process in the presence of Poly (N-Vinylpyrrolidone)(PVP) for lead free interconnects materials. The final product has an alloyed structure rather than core-shell structure evident from HRTEM and EDS. Ag-Sn alloy is one of the lead-free solders alloy system with the phase diagram well established (even by adding third element such as Bi, Cu, Zn and In)[18,19]. Figure 4.2 shows the phase diagram of the Ag-Sn alloy revealing that the melting point of pure Sn decreases c.a. 11℃ because of alloying with Ag and the lowest melting point is at eutectic point (Sn-3.5 Ag%). One of the challenges for lead-free solders is poor wettability due to their higher surface tension compared to Pb-Sn alloy and also, poor mechanical property because of the formation of intermetallic compounds[20].

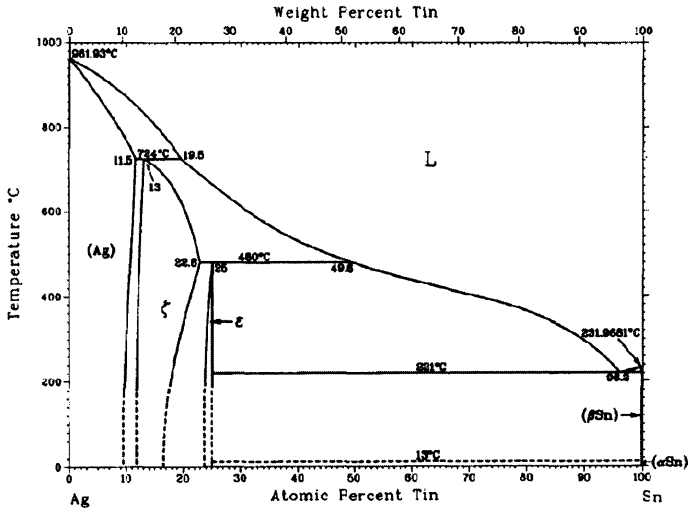

Figure 4.2: Phase diagram of Ag-Sn and eutectic point is at 96% Sn and 231.9 °C[21].

A third element (such as Bi[22,23], In[24], Zn[25] and Cu) may be added to the Ag-Sn alloy to improve wettability and mechanical properties by reducing grain size and to prevent oxidation. Currently, near eutectic SnAgCu (Sn-3.5Ag-0.5Cu) alloy is used as a lead free solder in electronic packaging. Hsiao et al synthesized Sn-3.5Ag-xCu (x= 0.2, 0.5, 1) ANPs by chemical precipitation method using $NaBH_4$. The X-ray diffraction (XRD) pattern revealed that the Ag_3Sn was formed as a result of the alloying process. The formation of Ag_3Sn and Cu_6Sn_5 gave strong evidence that the NPs were mixed homogeneously. Scanning Electron Microscopy (SEM) images showed particles within 41-45 nm sizes, but Transmission Electron Microscopy (TEM) images further revealed the aggregation of smaller particles of 4 to 5.5 nm sizes with the melting points from 214 to 215°C. The wettability test on AgSnCu particles revealed good metallurgical bonding between solders and substrates after reflow[26]. Rapidly solidified Ag-Sn-In alloy powders with composition of Ag-6.0Sn-3.0In were prepared by gas atomization to improve soldering property compared to Sn-Ag alloy[27]. Rare earth elements such as Bi added into the solder were adsorbed at the grain boundary of IMCs. The adsorption behavior changed the relationship between the growth velocities of the various crystalline directions of IMC which resulted in finer particles and more uniform distribution of the IMC phase and better soldering properties. The average size and distance of IMC particles decreased from 0.20 μm to 0.12 μm and 1.25 μm to 0.65 μm respectively. Fine IMC particles made the lead-free alloy mechanically stronger and more ductile through dispersion strengthening[28]. By doping Lanthanum (La) in microstructure of Ag-Sn solder alloy, the size of the Ag_3Sn decreases and remain stable even after thermal aging. Higher level of La doping leads to increase in the total number of Ag_3Sn particles and better

soldering properties[29]. Shen et al reported that by mechanical stirring of ZrO_2 during Ag-Sn alloying process, the size of Ag_3Sn IMCs are refined resulting in the increase in Vicker's micro-hardness of the prepared Sn-3.5 Ag alloy[30].

The Sn-Cu alloy has the potential to be a low cost alternative for wave soldering (large scale soldering). As mentioned before, the melting point of lead-free solders is approximately 30-40°C higher than Sn-Pb alloy. Therefore, the reflow temperature for soldering components on assembly boards should be raised at least by ~30-40°C. The higher reflow temperature leads to higher thermal stress on components and substrates which can cause package reliability problems such as substrate warpage, thermal stress, and popcorn cracking in compounds. Sn-Ag-Cu[31,32] and Sn-Cu[33,34] seems to have attracted the most attention for lead free soldering in electronic industries, because of better soldering properties and being more economical. Concerns with this alloy family include higher processing temperatures, poorer wettability due to their higher surface tension and their incompatibility with lead bearing finishes. Currently, SAD (Sn-3Ag-0.5Cu) is the most promising replacement for Sn-Pb in electronic industry. Recently, Gao[35] reported synthesize of nanoscale lead-free solders ("nanosolders") in form of multisegmented metal nanowires using an electrodeposition method in nanoporous templates and in the range of 1-200nm in diameter and 1-10μm. The melting point was reported close to bulk value, but the advantage would be that barrier segment is to avoid the intermetallic formation and the wetting segment is used to protect the metal surface and to ensure good solder reflow properties (solderability).

Au-Sn solder alloys have been studied less compared to Ag-Sn solder alloys, due to the cost associated with Au and the high melting point (~280°C at 30% Au) of the system

which can be an impediment to the packaging process causing damage to other electronic components. Ivey et al reported electroplating method to generate bulk Au-Sn solder alloy which is an alternative to the current commercial solder deposition process in vacuum[9-11]. Chemical reduction of Au-Sn ANPs has not been attempted so far. In this study we have successfully synthesized and lowered the melting point of Au-Sn solder, so that soldering can be accomplished without damaging the package. Upon melting of the ANPs and subsequent joint formation, the Au-Sn joint can offer superior creep resistance and reliability at high temperatures by reclaiming bulk characteristics such as high melting point (up to 420° C).

4.4 Au-Sn Phase diagram

Table 4.2 shows the characteristics of Au and Sn. The difference between their atomic radii is 4.6%, and based on the Hume Rothery rule, these two elements are extensively soluble. Two eutectic points at 30% and 93% Sn is observed in Au-Sn alloy system. Figure 4.3 shows the equilibrium bulk phase diagram of the Au-Sn alloy; the nanophase diagram of current system has not been developed yet.

Table 4.2: Characteristics of Au and Sn[36].

characteristic of elements	Atomic radius(nm)	Crystal structure	Electron configuration	Surface energy*(J/m^2)[37]
Au	0.144	FCC	[Xe] $4f^{14}$ $5d^{10}$ $6s^1$	1.39 ± 0.07
β-Sn	0.151	Tetragonal	[Kr] $4d^{10}$ $5s^2$ $5p^2$	0.68

*Surface free energies for Solid-Vapor Interface at the melting point.

In Table 4.3 some of the Au-Sn intermetallic compounds are reported. Gosh et al[38] calculated total energy of 29 Au–Sn intermetallics (stable, metastable, and virtual) from first-principles density-functional theory (DFT) employing ultrasoft pseudopotentials (USPP) and both local-density approximation (LDA) and generalized gradient approximation (GGA) for the exchange-correlation functional. He found that among the intermetallics, the ground-state structures are found to be for AuSn, $AuSn_2$, and $AuSn_4$ phase. Au_5Sn, though present in the equilibrium diagram, has slightly higher energy compared to other intermetallic compounds.

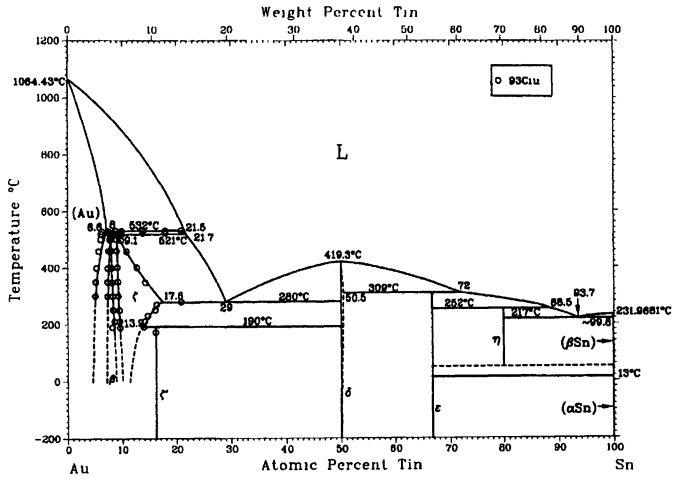

Fig 4.3: Au-Sn alloy phase diagram [31].

Table 4.3: Intermetallic compounds and elements available in Au-Sn phase diagram[39]

Phase	Composition, % Sn	Space group	Prototype
Au	0-6.8	Fm_3m	Cu
$Au_{10}Sn$ (ß)	9.1	$P6_3/mmC$	Ni_3Ti
ζ	10-18.5	$P6_3/mmC$	Mg
ζ'	16.7	R_3	...
δ or AuSn	50-50.5	$P6_3/mmC$	AsNi
ε or $AuSn_2$	66.7	Pbca	...
η or $AuSn_4$	80	Aba_2	$PdSn_4$
(ß Sn)	99.8-100	I41/amd	ßSn
(α Sn)	99.994-100	Fm_3m	C(diamond)

4.5 Experimental Section

Here the synthesis of Au-Sn ANPs by chemical reduction method is reported. Chloroauric acid ($HAuCl_4$), tin chloride ($SnCl_2$) as the metallic precursors and polyacrylic acid (PAA), Cetrimonium bromide ($(C_{16}H_{33})N(CH_3)_3Br$) or CTAB as the surfactant and sodium borohydride ($NaBH_4$) were used as purchased from Sigma-Aldrich. All precursors were applied in experimental processes without further purification. In a typical experiment, 25 ml of chloroauric acid solution (10^{-4}M) was added to 25 ml of tin (II) chloride solution (10^{-4}M) in the presence of 0.18 g capping agent to maintain concentration at about 10^{-3}M. This solution was reduced by 0.01 g sodium borohydride to obtain Au-Sn ANPs with narrow size distribution and with grey

color was synthesized for the first time with chemical reduction method at room temperature and schematic of reaction is shown in figure 4.1.

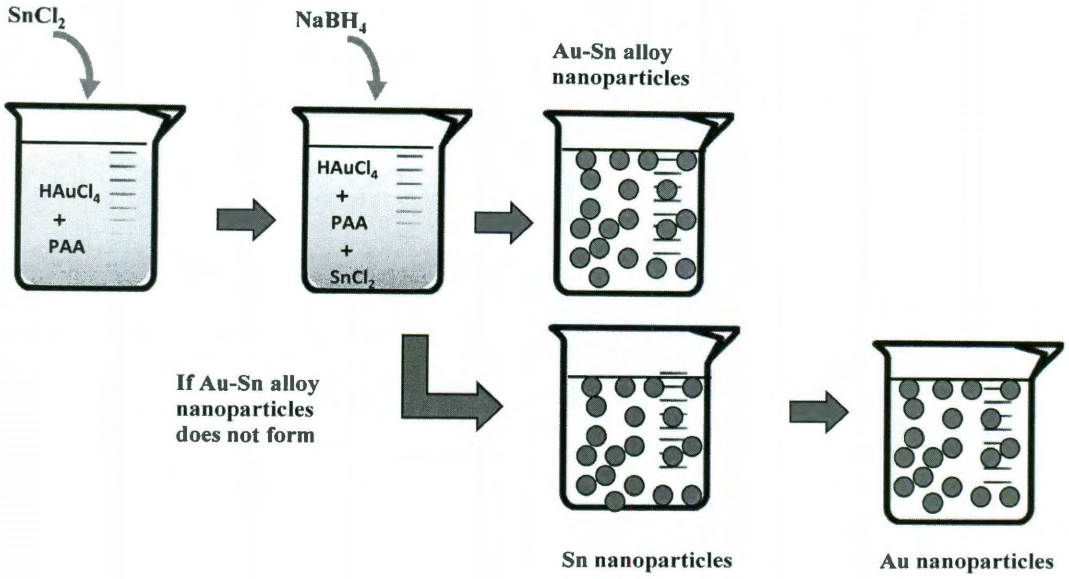

Figure 4.4: The schematic of experimental process to generate Au-Sn ANPs with co-reduction method.

The mixture was purified by recovering Au-Sn ANPs with ultra centrifugation at 40k rpm for 15 minutes and was then washed in water two times. There are certain challenges associated with the synthesis of Au-Sn ANPs using co-reduction method, since the reduction potential of Au and Sn $E^0(V)(Au^{+3}/Au) = +1.5$ and $E^0(V)(Sn^{+2}/Sn) = -0.14$ are not sufficiently close to co-reduce Au and Sn ions with $NaBH_4$. In this case, the system may lead to the reduction of Sn, since Au is capped (by surfactant or capping agent) and solution turns to brownish color. The Sn NPs are no longer stable and depend on the size of the Sn, they may act as reducing agents for the Au ions in the solution, leads the system to the formation of Au NPs. Lee et al[40] reported the environmentally friendly synthesis of Ag NPs with tin acetate (act as a reducing agent and catalyst). By increasing

the amount of reducing agent, bigger Sn NPs (with less catalysis property) are formed which may postpone the formation of Au NPs up to 1 month.

One experiment out of six, Au-Sn ANPs with grey color formed in presence of PAA with co-reduction method, otherwise, system mostly leads to the formation of Sn NPs. Not only method, selection of capping agent is also important in the formation of ANPs. CTAB is reported for tuning and assembly of Au NPs, because of its adequate attachments to the gold[41]. That could be the reason that Au-Sn ANPs (Au/Sn:1/1) cannot be co-reduced in presence of CTAB, but later on we discuss that Au-Sn ANPs are formed with (Au/Sn:4/1 & 1/19 weight % of Au and Sn precursors). Two step successive reductions was found to be more reliable and repeatable method for generation of Au-Sn ANPs. Figure 4.5 shows the schematic of the two step successive reductions and Au-Sn ANPs (Au/Sn:1/1 in presence PAA) were synthesized with this method has the lowest melting point.

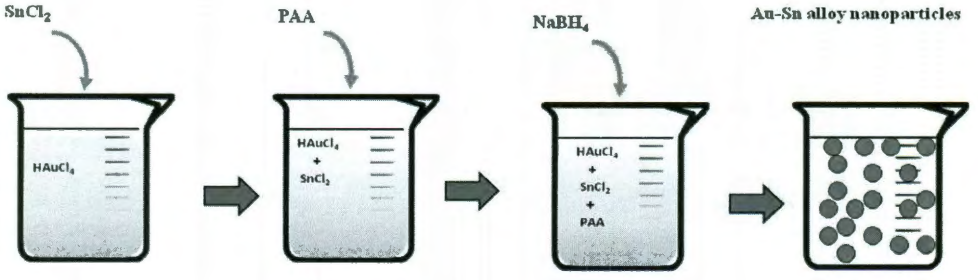

Sample Number	Weight % of Au:Sn precursors	Size distribution (nm)	Range of melting point (°C)	Crystal structure
Au:Sn 1:1	50:50	2-9	129-139	-----
Au Sn 1:1 (with out PAA)	50:50	5-10	80-149	Orthorhombic

Figure 4.5: shows the schematic of experimental process to generate Au-Sn ANPs with successive method also table which shows the characteristic of the samples were synthesized with current method.

Different molar ratios such as Au/Sn: 4/1, 1/1, 1/4, 1/19 were synthesized to further study the structure and melting point of ANPs within the increasing amount of Sn to find the best solder candidate (Figure 4.6). Au/Sn: 4/1 and 1/19 were chosen, because the current weight ratio of precursors represent eutectic points in the Au-Sn phase diagram.

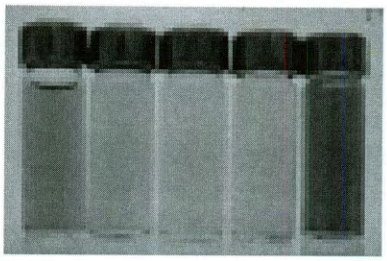

Figure 4.6: Different molar ratio of Au and Sn was used to synthesize Au-Sn ANPs. From right to left the ratio of Au/Sn precursors is: 4/1, 1/1,1/2, 1/4 , 1/19. Sample with higher molar ratio of Au precursor shows the Ruby red color similar to Au, but sample with equal amount of Au and Sn has grey color. By increase the amount of Sn, the color of solutions turn to brown color.

Yu et al[42] reported the preparation of high temperature stable Au@SnO_2 from AuSn ANPs with successive method followed by dry-oxidation approach as a catalysis for CO oxidation. First, Au NPs were synthesized under vigorous stirring and were refluxed by adding sodium citrate solution then $SnCl_2$ solution added along with PVP (Poly(vinyl Pyrrolidone), M_W= 30000). Mori [43]and Yasuda[44] studied structure and phase stability of Au-Sn alloy with in situ TEM by deposition different percentage of Sn up to 60% Sn. Henglein et al reported formation of Sn and Au-Sn particles by γ radiation. In the presence of colloidal Au particles, the reduction of Sn(II) by organic radicals is strongly enhanced[7]. Based on above reviews Au-Sn ANPs are reported by radiolysis and two step successive reductions.

In our typical experiment, the Au-Sn ANPs are formed in grey color, although the pure Au NPs is ruby red and Sn NPs is brown. Au-Sn ANPs showed no aggregation over a long period of time (several months) indicating particle stability and proper attachment of PAA to the surface of ANPs. Figure 4.7 shows the structure of CTAB and PAA which was used as a capping agent. CTAB has a long hydocabonyl chain which may not let Sn atoms diffuse to Au structure at room temperature. Characterization of the sample capped with CTAB is quite difficult; since CTAB cannot wash off easily from the sample then pure CTAB film was prepared in the same concentration of experiment for XRD measurement. Figure 4.8 shows the XRD pattern of CTAB film which is similar to the pattern observed from Au-Sn ANPs.

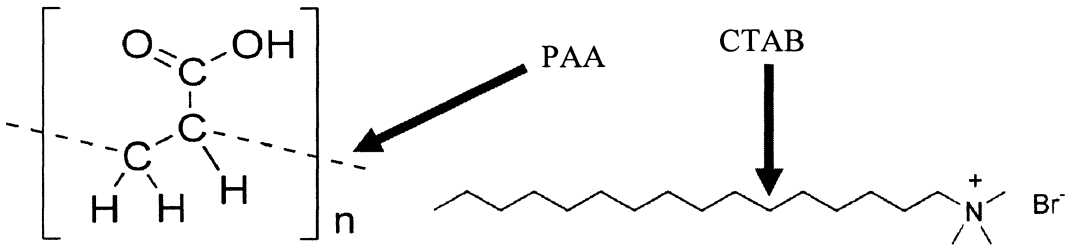

Figure 4.7: Cetrimonium bromide ($(C_{16}H_{33})N(CH_3)_3Br$) has a longer hydrocarbon chain than Polyacrylic acid (PAA) can be the reason that alloying did not occur for Au-Sn ANPs (Au/Sn:1/1) in presence of CTAB.

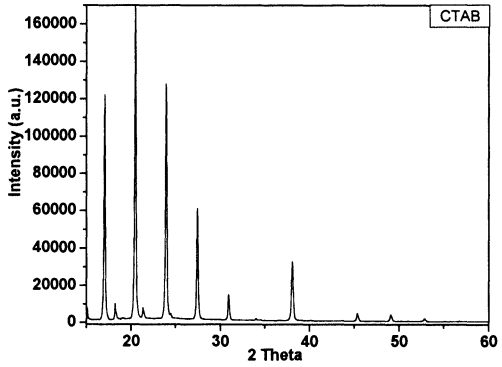

Figure 4.8: XRD pattern of only pure CTAB. If CTAB did not wash completely from the sample, these peaks superimposed with other peaks from sample and differentiation between the peaks is difficult.

UV spectroscopy, X-ray Diffraction (XRD), Fourier Transform Infrared spectroscopy (FTIR), Electron microscopy and spectroscopy confirm the formation of AuSn ANPs using chemical reduction method. UV spectroscopy was performed on a UV-3600 Shimadzu Spectro-Photometer operated at a resolution of 2 nm. FTIR measurements of the Au NPs were carried out in the diffuse reflectance mode at a resolution of 4 cm^{-1} on a FTIR 8400S Shimadzu infrared spectrometer. Size, shape, and structure of Au-Sn ANPs were studied by JEOL transmission electron microscope (TEM) operated at 200 kV. The chemical composition of individual particles deposited on holey carbon grid was analyzed by energy- dispersive x-ray spectroscopy (EDS) and was calculated from the intensity ratio of Au M_α to Sn M_α peak. The EDS was carried out using an electron probe of approximately 1nm in diameter. X-Ray diffraction (XRD) measurement was conducted by using Rigaku D/max Ultima II, and the data was analyzed using JADE 8.5 software and PDF-4 database from the International Center for Diffraction Data (ICDD).

4.6 Characterization of Au-Sn alloy ANPs

Sn and Au NPs were synthesized as control samples in the same condition that was used to synthesize Au-Sn ANPs. Figure 4.9 and 4.10 show the TEM images of spherical Au and Sn NPs and their size distributions in the presence of CTAB. Au NPs are up to 10 nm in size and Sn NPs are between 2-7nm, although larger particles in the range of 20-30 nm still exist in both control samples. CTAB with long chains may prevent atomic diffusion of Sn into Au and the alloying process for Au-Sn ANPs (Au/Sn:1/1) at room temperature does not take place. The alloying process of Au-Sn ANPs (Au/Sn:1/1) in the presence of CTAB will be further discussed at a later section. However, the Au-Sn ANPs with molar ratios of Au/Sn:4/1& 1/19 in the presence of CTAB are formed. In this case, the Au ions are capped with CTAB in solution and subsequently, the Sn ions are reduced by $NaBH_4$ to form Sn NPs. Sn NPs are stable only for a short time and then the system is led to the formation of Au NPs where each step was confirmed by UV spectroscopy and electron diffraction (Figure 4.11). The formation of Au NPs delayed up to one month by increasing the amount of the reducing agent (up to 8 times). The increase in the amount of reducing agent leads the system to the formation of lager Sn NPs resulting in the decrease of catalysis property of Sn NPs and delay the formation of Au NPs. The formations of Au NPs can be accelerated by:

1) Heating the solution up to 80° C

2) Stirring the solution at high speed during synthesis.

Another capping agent is polyacrelic acid (PAA) which did not exhibit adequate attachment to the surface of the Sn and Au NPs, and particles began to aggregate shortly

after their synthesis, but showed proper attachment to the surface of Au-Sn ANPs. The stability of Au-Sn ANPs can be attributed to the surface modification of ANPs with PAA (acting as a surfactant)[45]. The presence of PAA in the solution is believed to have two main roles:

1- It stops the growth of the particles at a small size distribution.

2- It prevents the individual particles from aggregation.

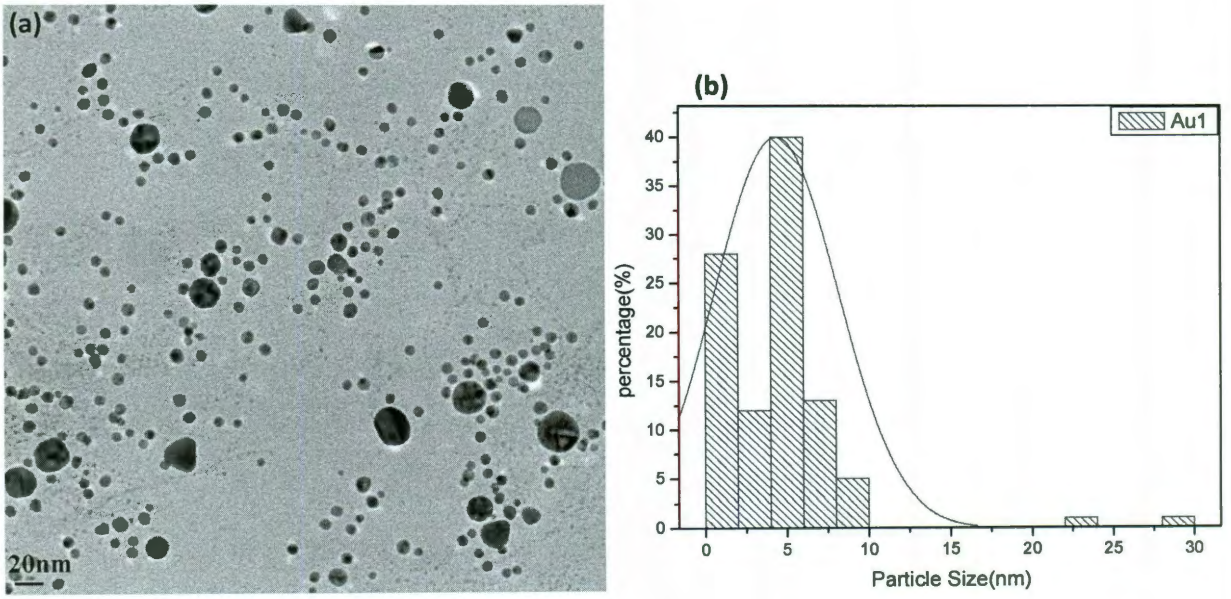

Figure 4.9: (a) the spherical morphology of the Au in the presence of CTAB. (b) Size distribution of Au NPs is up to 10nm, although some larger particles around 20-30 nm can be observed.

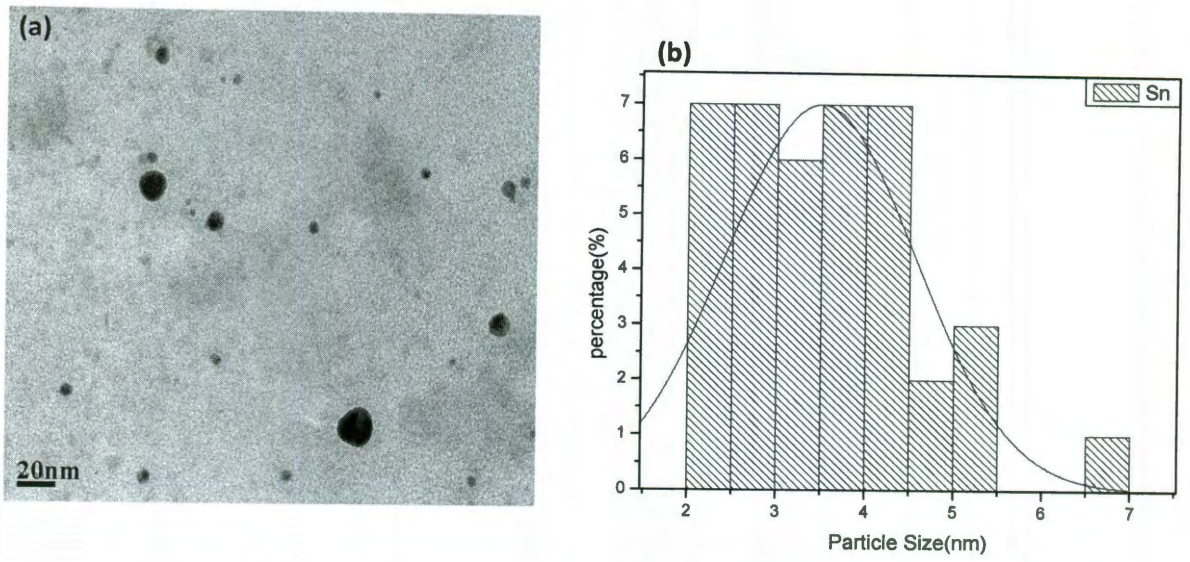

Figure 4.10: (a) the spherical morphology of Sn NPs in presence of CTAB. (b)Size distribution of Sn NPs is 2-7 nm.

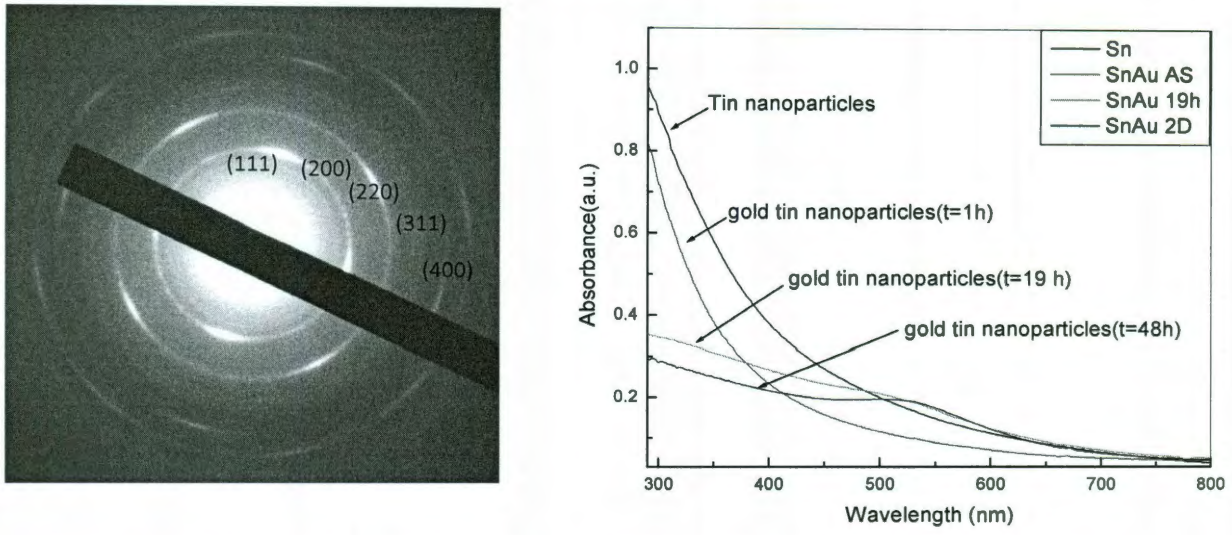

Figure 4.11: a) Electron diffraction (ED) of the solution after it turned from brownish color to ruby red color. Electron diffraction from different part of the sample confirms the formation of Au NPs with cubic structure. b) Time evolution of the solution which Au-Sn alloy did not form; subsequently Sn and Au NPs were formed which was confirmed by ED and EDX. CTAB was used as surfactant.

The primary reaction in the alloying of Au-Sn ANPs involved the Au/Sn:1/1 (molar ratio of precursors) and in subsequent experiments various molar ratios of Au and Sn have been investigated (based on weight percentage in phase diagram) to find the best ANPs

candidate for Pb-free soldering. For this purpose, two eutectic points (20 and 92 weight percentages of Sn) were chosen to study the structure, compositions and their melting points. Table 4.4 shows different molar ratios of Au and Sn precursors, their size distributions, melting points and structures, respectively. When the concentration of Sn increases, the size distribution of ANPs is significantly reduced.

Table 4.4: Different weight percentages of Au and Sn precursors used to synthesize Au-Sn ANPs in the presence of PAA and CTAB.

Name of samples & precursors ratio	Weight % of Au:Sn precursors	Size distribution (nm)	Range of melting point (℃)	Crystal structure
Au as a control sample	100:1	5-10	900 - 1020	FCC
Sn as a control sample	1:100	2-7	160 - 170	Tetragonal
(1) Au:Sn 4:1 (CTAB)	80:20	4-13	85 – 140	-------
(2) Au:Sn 1:1 (PAA)	50:50	2-10	187 - 186	Hexagonal
(2') Au:Sn 1:1 (PAA)	50:50	5-10	80 - 149	Orthorhombic
(3)Au:Sn 1:19 (CTAB)	5:95	1-4	165 - 175	Orthorhombic

Figures 4.12 and 4.13 show the particle size and the spherical morphology of Au-Sn ANPs. The morphology of particles did not significantly change after increasing the amount of Sn precursor, but decrease in the size distribution and melting points were observed.

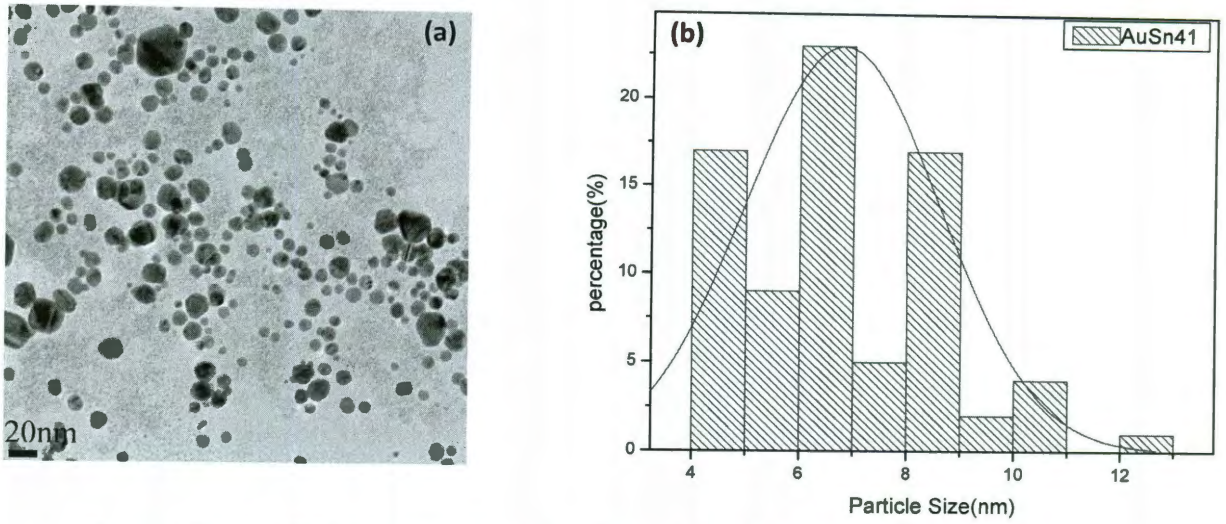

Figure 4.12: (a) TEM image of Au-Sn alloy ANPs (Au/Sn:4/1) with spherical morphology and (b) size distribution of 4-13 nm and also larger particles up to 20 nm.

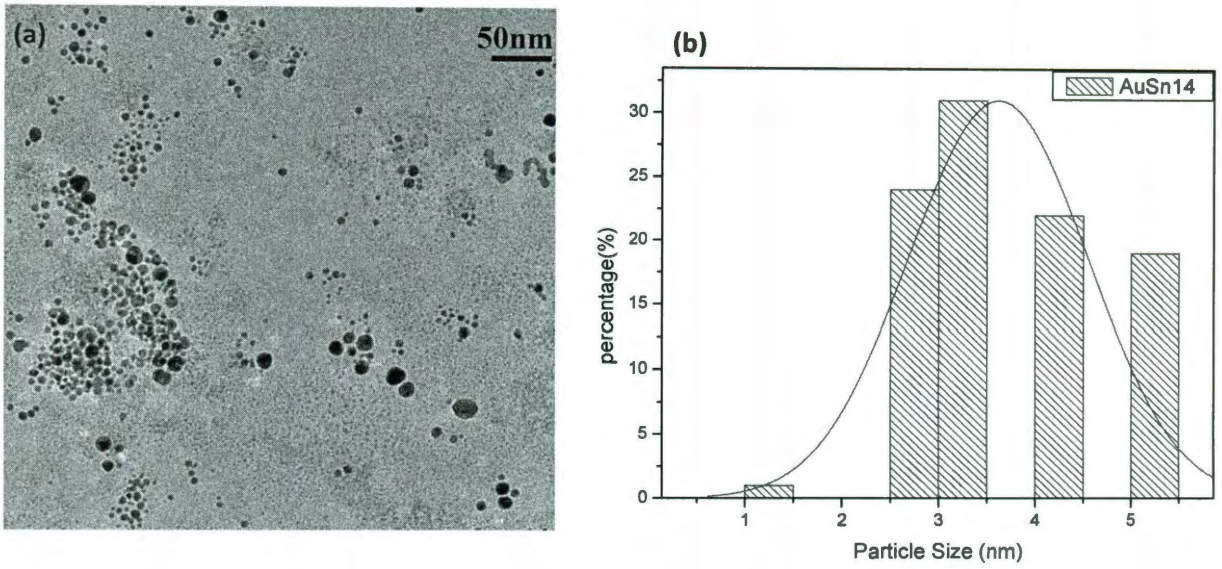

Figure 4.13: (a) TEM image of Au-Sn alloy ANPs (Au/Sn:1/4) with spherical morphology and (b) size distribution of 1-6 nm and also with larger particles up to 20 nm.

The absorbance studies were performed after 1 hour to ensure the complete reduction of the metal ions. The Au NPs solution shows the characterized absorbance of ~520 nm (Figure 4.14 a)) due to the surface plasmon resonance. Sn NPs solution shows typical semiconducting behavior and does not show significant features in the visible region. The

absorption peak of Au-Sn ANPs is tunable depending on the amount of Sn incorporate to the Au structure. Figure 4.14 shows the evolution of optical absorption of Au-Sn ANPs within the increase in the amount of the Sn and change in the size of ANPs in the presence of CTAB and PAA. The absorbance behavior of the ANPs is found to be similar to that of Sn NPs (absorption peak completely dampened) by increasing the ratio of the Sn (Au/Sn: 1/4, 1/19) which can be the result of change in electron density and reduction of electron mean free path in ANPs. Mean free path of the electron clearly depends on the homogenous effect such as size, shape and local porosity[5]. Similar optical trend (size and time evolution of the absorption spectra) has been observed by Henglein with deposition of Sn on Au NPs in aqueous solution by γ radiation[46] and also, Dahal and co-worker reported dampening in absorption band for Au-Fe ANPs compared to Au NPs[47]. Table 4.4 shows the decrease of the size distribution of ANPs and Figure 4.15 depicts the size evolution of absorption peaks similar to that observed by Henglien. By decreasing the size of the particles, the absorption peaks of the ANPs are completely dampened.

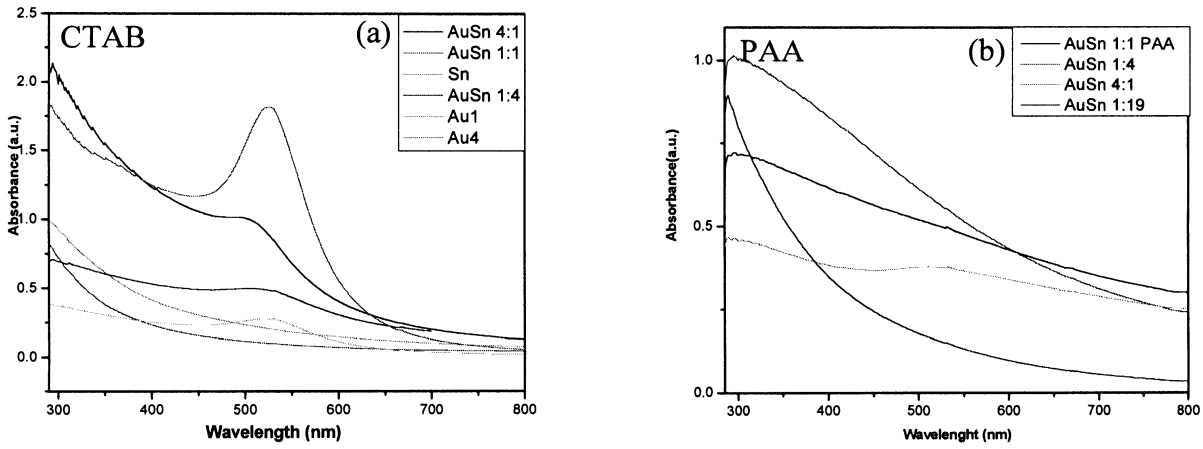

Figure 4.14: a) Optical absorption of Au-Sn ANPs in presence of CTAB. The number front of sample is the molar ratio precursors. b)) Optical absorption of Au-Sn ANPs in the presence of PAA. When the molarity of Sn is equal or higher similar behavior as Sn is shown, except for the higher ratio of gold where a broad absorption peak was observed.

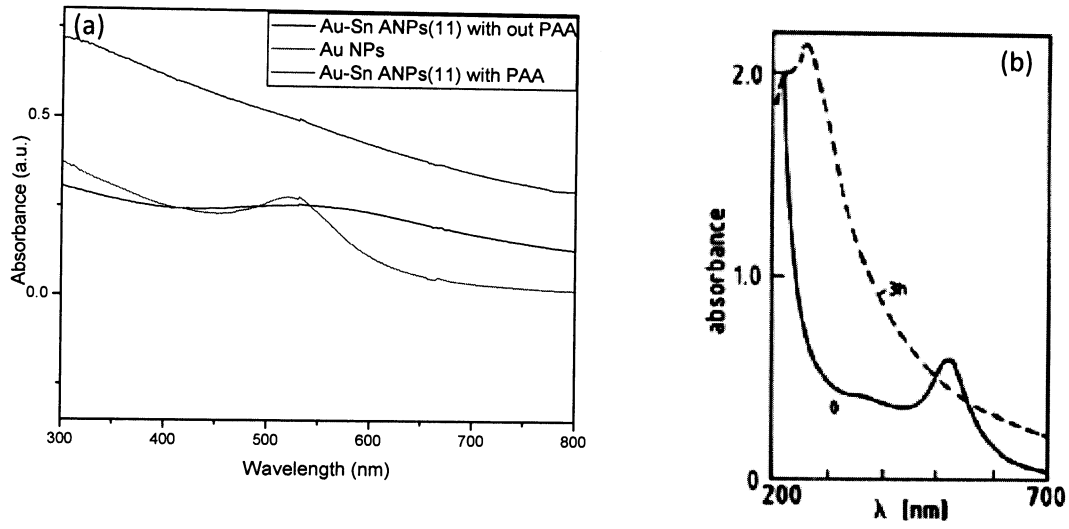

Figure 4.15: a) The optical absorption of Au NPs and Au-Sn ANPs with and without PAA. The size effect is clearly observable here, but not the composition effect. b) The absorption peak of Au at ca. 500nm where after 3 hours of γ radiation, the absorption band of Au is completely dampened during alloying[46]. Even in our experiment within the alloying with Sn absorption peak of Au is become broader and dampened.

Figure 4.15 shows the absorption peaks of Au-Sn 1:1 ANPs with and without PAA. Clearly, ANPs without PAA have more contribution of Sn in the alloying process and are expected to be larger in size, since there is no ligands that contributes in this process. The absorption peak of the ANPs after increasing the amount of Sn is expected to completely dampen compared to that of Au NPs and ANPs with lower Sn content where the absorption peak is severely broadened and only partially dampened. This is caused by the effect of size not composition. In other words, ANPs without PAA have larger particles which lead to the absorption peak being broadened and dampened compared to that of Au NPs and Au-Sn ANPs with PAA.

To investigate the stability of the Au-Sn 1:1 ANPs with PAA, FTIR study was performed on a film of Au-Sn ANPs. Figure 4.16 shows the FTIR spectra of a drop-coated film of PAA capped Au-Sn ANPs and PAA powder on Si (111) substrate. A prominent absorption is seen at ca. 1546 cm^{-1} for both the pure PAA film and PAA capped Au-Sn ANP film. This band is due to the excitation of carbonyl stretch vibrations in the carboxylic groups of PAA molecules. The presence of carbonyl stretch in Au-Sn ANPs indicates that Au-Sn ANPs are stabilized by PAA acid. The PAA film shows an additional absorption at ca. 1716 cm^{-1}. This band is assigned to the carbonyl stretch of the carboxylate groups of PAA molecules.

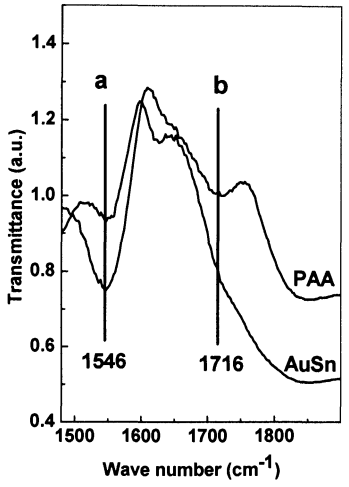

Figure 4.16: FTIR spectra of PAA capped Au-Sn and pure PAA film shows adequate attachment of PAA on the surface of Au-Sn 1:1 ANPs.

The XRD pattern from the Au-Sn ANPs (Au/Sn: 1/1 capped with PAA) deposited on a glass substrate is shown in Figure 4.17. For the XRD phase identification, both intensity and lattice spacing are equally considered in the search match (Hanawalt method) using Jade software. This XRD pattern shows prominent Bragg reflections of 23.6, 28.7, 40.5,

41.6, 59.6 and 75.6 which correspond to the (100), (101), (102), (110), (202) and (212) Bragg reflection planes of the Yuanjiangite (AuSn) phase, respectively. As indicated in JCPDS card No. 98-000-0470, this structure has the space group symmetry of P63/mmc (194) with hexagonal structure. During the alloying process, the unit cell structure of Au shows a positive deviation means XRD pattern of AuSn moved towards smaller angle compared to Au XRD pattern. Table 4.5 shows the Au structure contributions to 6.1% in both X and Y axes 35.5% in Z axis and 3.07% volume expansion of unit cell during the alloying process. The 2D and 3D projections of the AuSn phase structure are shown in Figure 4.18.

Table 4.5: Volume and axis expansions of Au unit cell and AuSn 1:1 unit cell in presence of PAA structures during the alloying process.

Materials/cell characteristic	X (Å) axe of unit cell	Y (Å) axe of unit cell	Z(Å) axes of unit cell	Volume(Å)^3 of unit cell
Au	4.064	4.064	4.064	67.12
AuSn	4.316	4.316	5.51	273.01
Volume expansion	6.1%	6.1%	35.58%	3.07%

Yu et al also identified AuSn phase with the same structure by successive method which involved the reduction of Sn^{+2} in the presence of Au NPs at room temperature. Au nanoparticle seeds were synthesized under vigorous stirring and reflux of $HAuCl_4$ in the presence of sodium citrate and the $SnCl_2$ was subsequently added and reduced in the presence of poly(vinyl pyrrolidone) (PVP, M_w=30000). Sharp peaks in the XRD pattern might be the result of sintering of the Au-Sn ANPs on the glass substrate at room

temperature. TEM image reveals that AuSn ANPs in the range of 2-10nm are not spherical. It can be noted from the integrated intensity above the background of XRD data that the ratio between the intensity of (100) to (102) and (101) to (102) peaks are slightly higher than the powder diffraction file (PDF) card. The intensity ratios reveal that the hexagonal structure is abundant in (100) and (101) planes on the surface which explains the non-spherical (faceted structure) characteristics of particles usually observed for particles above 50nm[48].

Table 4.6: Comparison of the second and the third highest intensities of XRD of AuSn 1:1 ANPs in presence of PAA with that of the pdf-4 data base, reveals the abound of plane (100) and (101).

Plane	In experiment	In data base
Ratio of (100)/(102)	53.3	68.3
Ratio of (101)/(102)	47.2	48.3

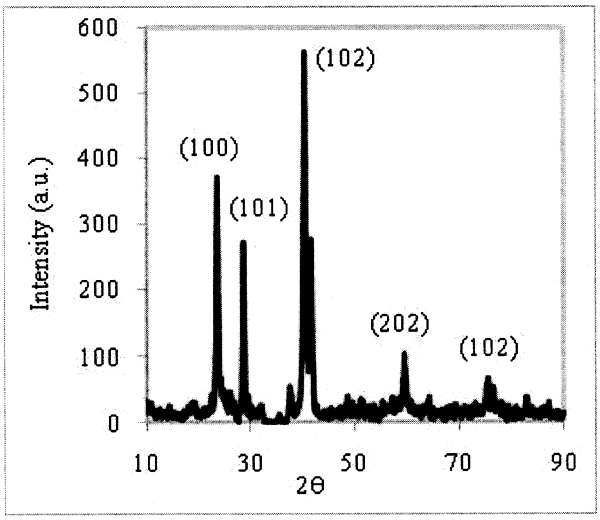

Figure 4.17: AuSn phase identified with hexagonal structure (JCPDS card No. 98-000-0470).

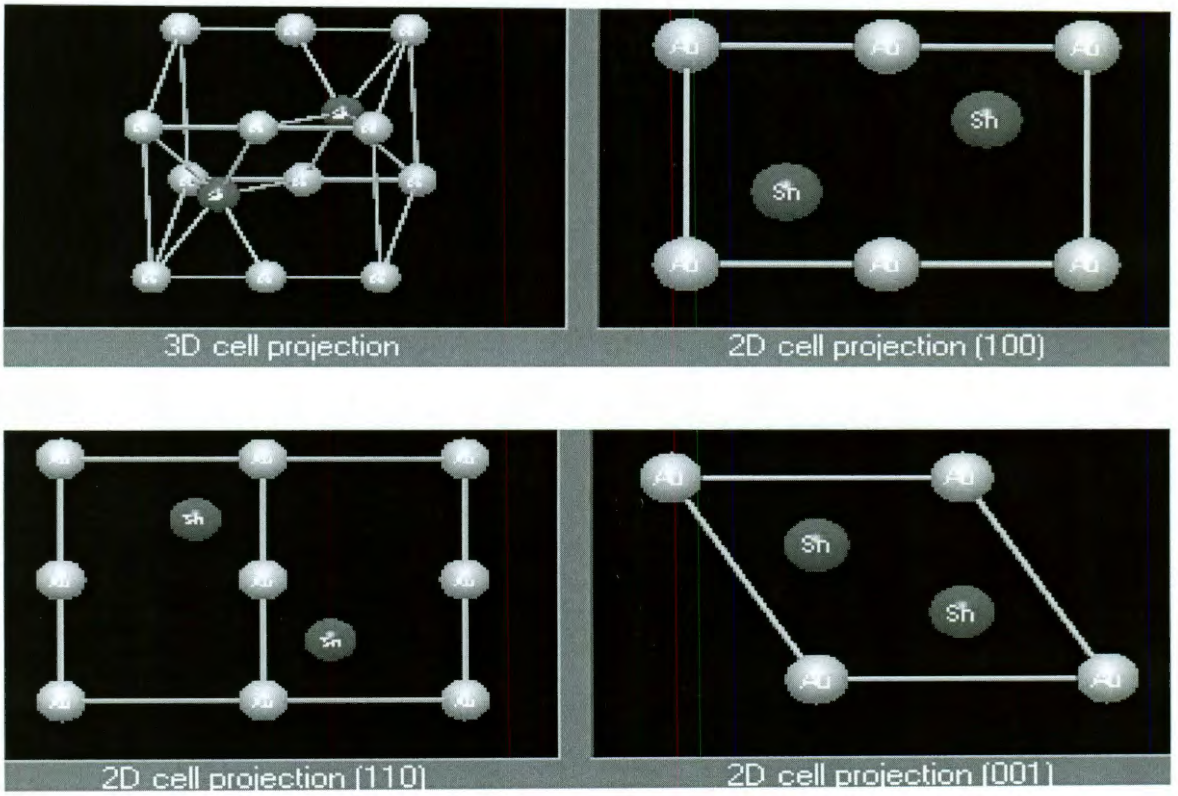

Figure 4.18: The 2D and 3D projections of hexagonal AuSn ANPs where particles are abundant in (100) on the surface, because the intensity of (100)[respect to 100% peak] in XRD pattern of our experiment is higher than that intensity of (100) exist in pdf.

To further study the role of PAA in the alloying reactions, Au-Sn ANPs (Au/Sn:1/1) were synthesized without PAA where the ANPs were observed to be unstable. By reducing the amount of $NaBH_4$ down to 1.25×10^{-3} mole, stable Au-Sn ANPs without PAA were obtained (referred to as sample 2'). The size of the ANPs strongly depends on the presence of PAA and in case of sample 2' without the presence of PAA, larger particles were formed.

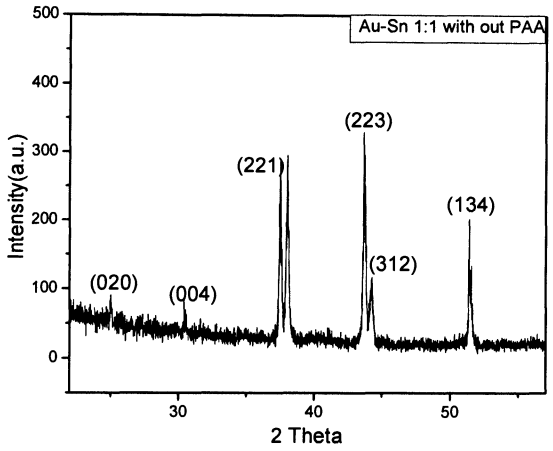

Figure 4.19: XRD pattern of Au-Sn ANPs (Au/Sn:1/1 without PAA) shows the formation of $AuSn_2$ with orthorhombic structure which is different from ANPs with hexagonal structure formed in the presence of PAA.

The X-ray diffraction pattern in figure 4.19 indicates the formation of intermetallics $AuSn_2$ with orthorhombic structure (space group Pbca, JCPDS card No. 03-065-1322). For further study of crystalline structure of the $AuSn_2$, figure 4.20 shows clearly atomic positions of Au and Sn in the 3D structure and 2D structure projected in (100), (001) and (101).

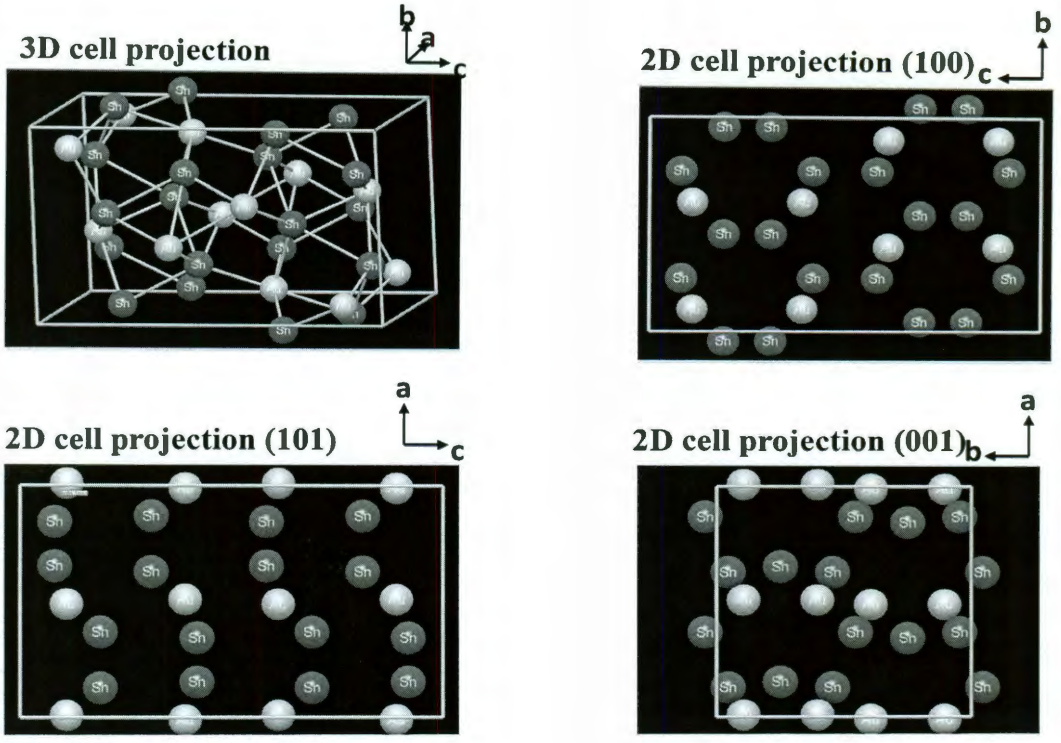

Figure 4.20: Different structural views of $AuSn_2$ in 2D and 3D cell projections on (100), (001) and (101) planes which clearly shows the Au and Sn positions in the cell.

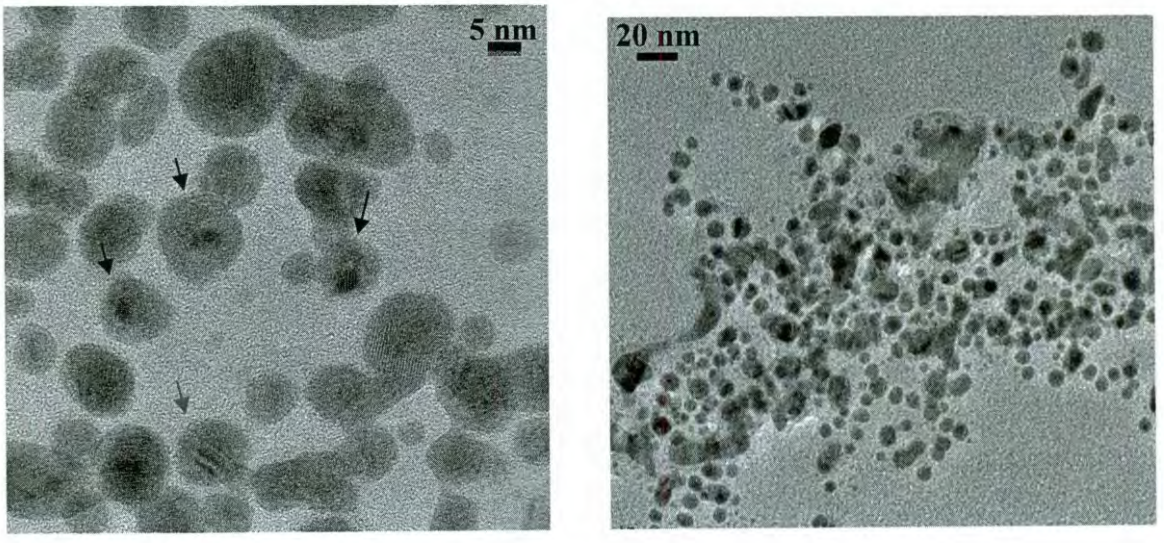

Figure 4.21: Au-Sn ANPs (Au/Sn:1/1 capped with PAA) with core-shell (displayed by black arrows) and twine structures (red arrow).

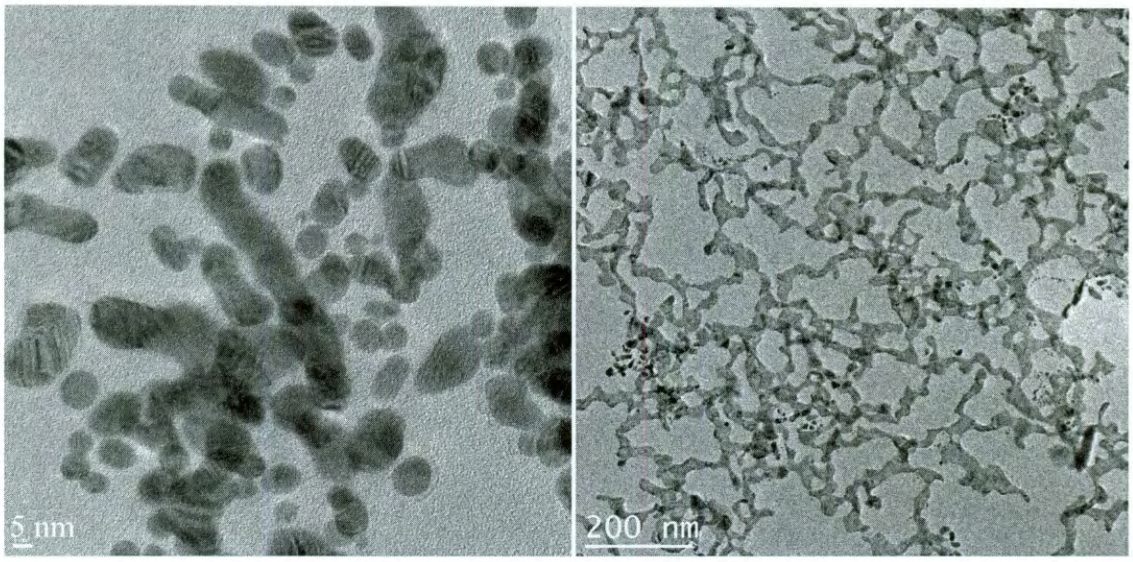

Figure4.22: Au-Sn ANPs (Au/Sn:1/1 without PAA) with semi-spherical, ellipsoid and network structure is observed.

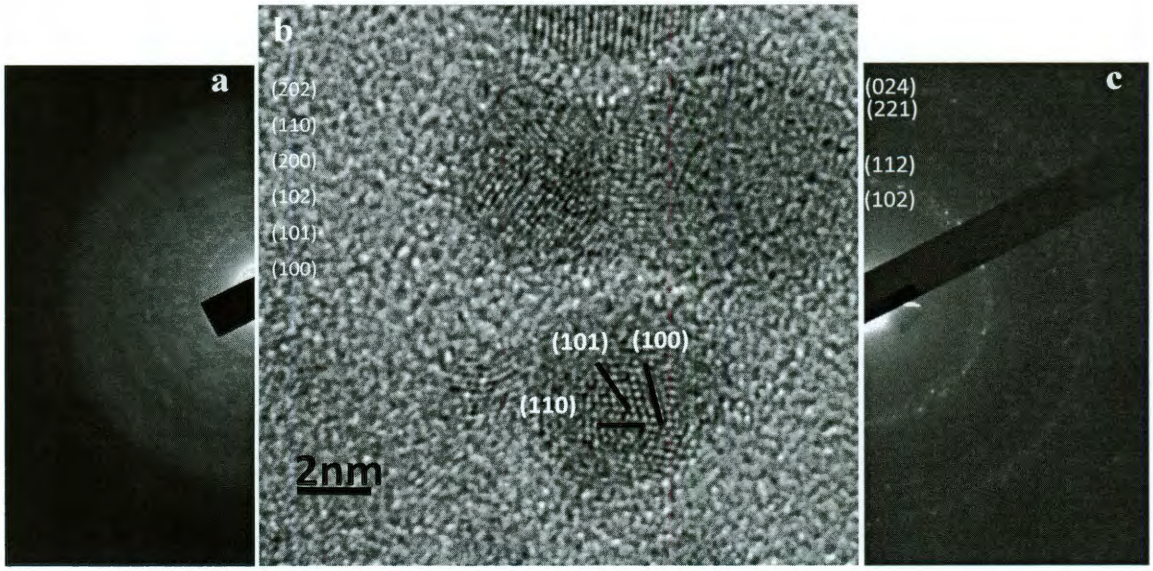

Figure4. 23: a) Electron Diffractions of Au-Sn ANPs (Au/Sn:1/1 with PAA) with AuSn hexagonal structure. b) HRTEM shows the abundant plane (100), (101) and (110) of AuSn in the surface of hexagonal structure. c) Electron Diffractions of Au-Sn ANPs (Au/Sn:1/1 without PAA) with AuSn orthorhombic structure and planes are (from smaller rings to larger rings) (102),(112),(221)(024).

Figure 4.23(a) is the diffraction pattern of AuSn ANPs (in the presence of the PAA) showing the polycrystalline structure of particles depicted in Figure 4.23(b). The geometry and structure of the sample was determined by selected area diffraction (SAD). The Debye-Scherrer rings can be indexed as (100), (101), (102), (200), (110), (202), respectively which confirms the formation of AuSn phase with hexagonal structure and the same structure was reported by Mori at el for ANPs below 10nm produced by deposition of Sn on Au NPs. High-resolution transmission electron microscopy (HRTEM) confirmed the hexagonal structure of ANPs (Figure 4.23(b)) and showed that the ANPs do not exhibit a core-shell structure. Figure 4.23(c) confirms the orthorhombic structure Au-Sn ANPs (Au/Sn:1/1 without PAA). The distance between the adjust lattice fringes of AuSn (101), (110), (100) are 0.309, 0.215, 0.373 nm which are in agreement with electron diffraction. The Au-Sn ANP (Au/Sn:1/1 with PAA) size distribution of 2-10 nm is shown in Figure 4.24(a) and Figure 4.24(b) reveals the energy dispersive X-ray analysis (EDX) spectra obtained from the different particles showing Sn M_α and Au M_α peaks from individual NPs.

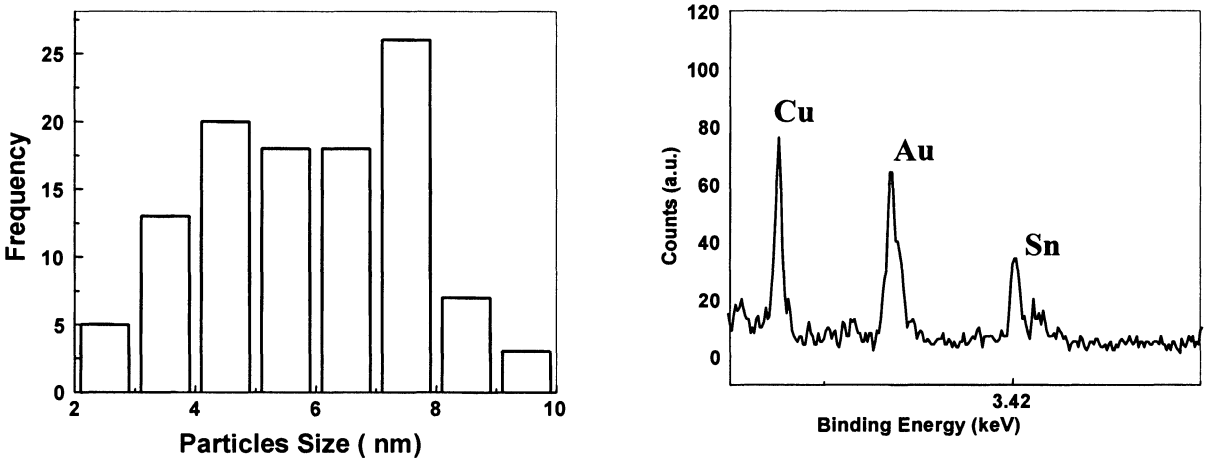

Figure 4.24: a) EDS confirms that both Au and Sn are present in the individual particle. b) Au-Sn ANPs (Au/Sn:1/1 with PAA) are between 2-10nm.

The EDX spectrum from different individual NPs shows that the composition of different particles ranges from 16 to 57% Sn. Further study on the different particles sizes and their composition reveals that the composition of these ANPs is size dependent. Yasuda[44] et al showed in an in situ study that the composition of particles falls into two regions as functions of both size and concentration (Figure 4.25). Study on Cd- Bi ANPs[49,50,51] which was synthesized by melt spinning revealed that the size of ANPs is not composition dependent, but other systems such as Au-Sn alloy are more complex and for specific size, particles with different compositions are exist.

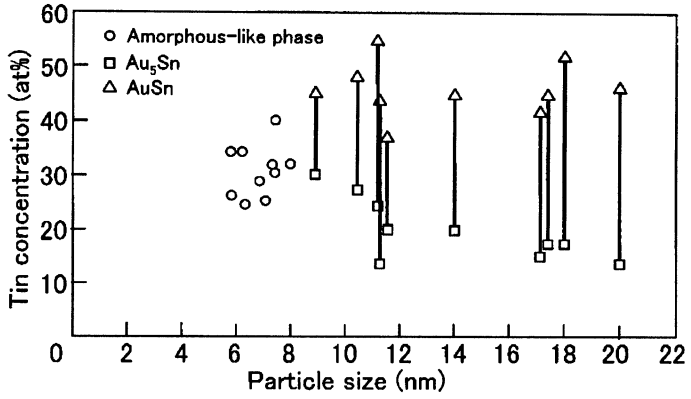

Figure 4.25: Change in the nanostructure of alloy nanoparticles when the composition falls into two phase region as functions of both size and concentration[44].

Further study reveals that when the particle size was at or above 10 nm, two phases are formed as expected from the phase diagram. However, for particles below 6 nm, amorphous structures were observed when the compositions falls between 18-59% Sn. The interfacial energy between two phases increases the Gibbs free energy of the small particles and can reduce their stability, therefore, minimizing the possibility of two phase formation for particles below 10 nm.

In the Au-Sn phase diagram, within the range of 16 to 57% Sn, two phases of AuSn and Au_5Sn co-exist at room temperature and only AuSn phase is observed through the line of 50% Sn. A slight composition deviation from 50% Sn in equilibrium leads to the formation of Au_5Sn (for less than 50% Sn) and $AuSn_2$ (for higher than 50% Sn) as well, but for particles below 10nm, the formation of two phases is not possible as previously stated. The formation of AuSn phase in our system, for this range of composition at the nanoscale, shows an increase of solubility of Sn in Au, because the lattice itself softens, and lattice distortion induced by dissolution of Sn atoms could be much more relaxed than in bulk materials. The formation of AuSn (with hexagonal structure) not Au_5Sn (with orthorhombic structure) in our system could be due to the higher stability of hexagonal structure compared to the orthorhombic structure in bimetallic compounds (e.g. lanthanide manganates ($LnMnO_3$)) based on computer simulation)[52,53]. Also, Ghosh et al stated that among intermetallic compounds the ground state was found to be for AuSn, $AuSn_2$ and $AuSn_4$. Another phase (Au_5Sn) though exists slightly higher than the ground state[54].

The melting temperature of AuSn ANPs was measured using differential scanning calorimetry (DSC) performed on a Q-600 Simultaneous TGA/DSC from TA Instruments. AuSn ANPs were synthesized in large scale, since a minimum of 5 mg was required for DSC measurements. The first heating cycle was from room temperature to 500°C with the heating rate of $5°Cmin^{-1}$and the system started melting at about187°C. Figure 4.26 shows five melting (endothermic) peaks between 187 to 196°C. The replacement of one melting point by a range of points is in agreement with the prediction made previously by Herlach et al for small nanoparticles. Herlach et al constructed particle size-dependent

phase diagrams for binary alloys using free energy functions that included the capillary energy of internal interfaces that separate the phase within the particles.

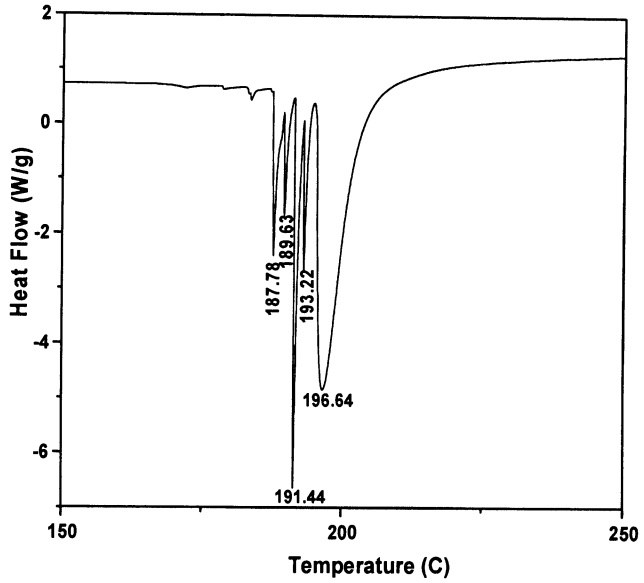

Figure4.26: DSC of AuSn ANPs with PAA capped shows significant decrease in melting point, ranging from 187-196°C.

A significant finding from the DSC curve (Figure 4.26) is that the melting point of AuSn ANPs (187-196°C) is much lower than that of the bulk alloy based on the conventional phase diagram (along 50% Sn, $T_{Au\text{-}Sn}$= 419°C). The melting point of AuSn ANPs (as low as 187°C) is even lower than that of Ag-Sn solder ANPs (10 nm) with a melting point around 194°C. Comparing the DSC curve in Figure 4.26 with the size distribution of particles (Figure 4.24 b), we can conclude that particles with 7-8 nm have melting point of ~191°C. The thermodynamic calculations for spherical nanoparticles indicate a linear relationship between the melting point and R^{-1} as below:

$$T_m = T_{m,inf}(1-\alpha/2R)$$

Where $T_{m,inf}$ is the bulk melting temperature and α is a shape factor. More faceted the shape is, higher is α, and larger is the depression in the melting point. For spherical NPs, α=1 and for cubic NPs α is between 2.12 to 2.85. Based on the above equation and the value of α, spherical particles are thermodynamically more stable and as the particle size reduces, the melting point decreases less compared to other shapes. Since the AuSn NPs have faceted structures, particle size reduction can lead to a more significant decrease in the melting point. Shape factor (α) was calculated 4.35-5.32 for our experiment by assuming:

- Melting point (Au/Sn:1/1) between 187-193°C
- Particles 7-8 nm and melting point bulk =280°C

Polyacrylic acid (PAA) [melting point=14°C] and cetrimonium bromide (CTAB) [melting point =237-243°C] do not contribute to the melting point of ANPs. Furthermore, the appropriate capping agent in successive method can influence the size and shape of the particles, and the surface tension, therefore, playing a key role in the depression of the melting point.

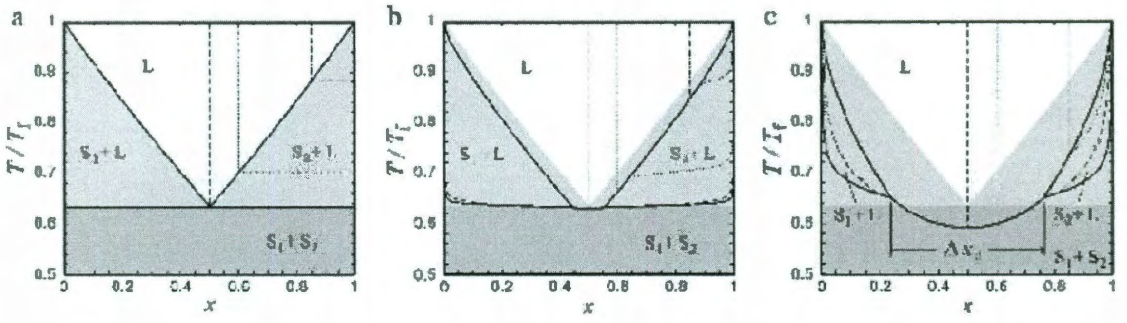

Figure 4.27: Computed alloy phase diagrams for different particle sizes: (a) D ⟶ (macroscopic limit), (b) D = 50 nm, and (c) D = 5 nm. Black lines: phase coexistence lines; dot, dash, and dash-dot lines: lines or equal solute fraction x_L in the liquid phase (in the single-phase liquid and in the two-phase solid-liquid region as well) for three arbitrarily chosen values of x_L. Shaded fields represent the phase regions of the macroscopic alloy[55].

It was discovered that several rules that generally apply to the creation of phase diagrams for microscopic systems were no longer valid for nanoscale alloy particles. For example, the eutectic point was replaced by a range of compositions in which the alloy melted discontinuously at small system size. Specifically, for 5 nm particles, Herlach et al[50] calculated that when the eutectic composition changed from 0.25 to 0.75, T/T_f changed from 0.6 to 0.66 (Figure 4.27 (b)). In the calculation of nanophase diagram for small particles[55,56], Herlach assumed:

- No mutual solubility of elements at solid state and ideal solution in liquid state
- Spherical shape for particles
- Constant pressure
- Two phase co-exist
- Surface energy varies nonlinear as function of a phase fraction.

As the particle size increased to about 50 nm, the range of compositions narrowed down to 0.4-0.6% and the melting temperature returned to a point (T/ T_f = ~0.64).

G. HÖhne et al[57], [58] reported the phase diagram of the benzyl/acetanilide binary system schematically along with the DSC curves of pure elements and five different compositions of solid solution including the eutectic point. Considering the DSC data for different compositions, the data presented in our study, ranging in composition (16-57% Sn), can be the superimposed version of the data obtained by HÖhne et al (Figure 4.27).

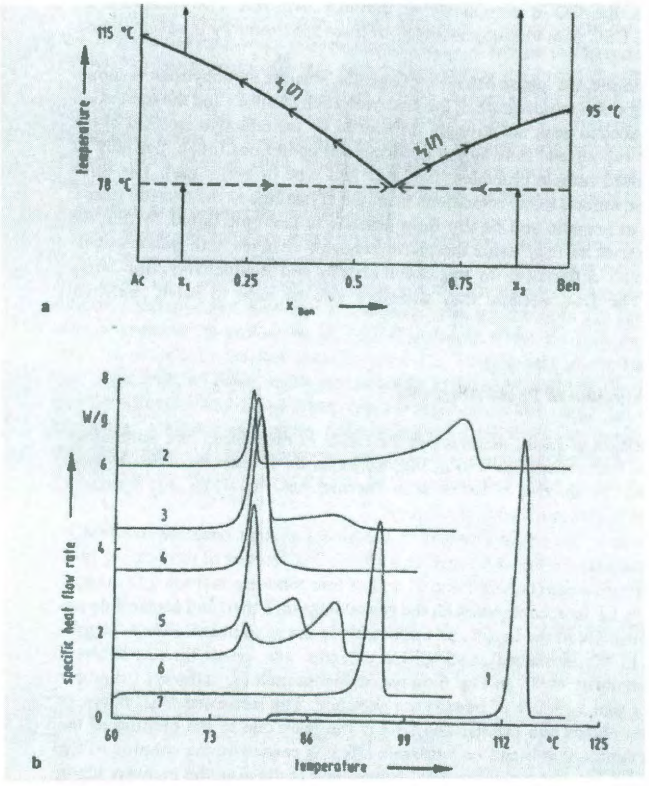

Figure 4. 27: The phase behavior of the system acetanilide (Ac) – benzyl (Ben) a) schematic phase diagram of the eutectic system, the arrows mark he course of the melting process for two mixtures with the mole fraction of x_1 and x_2.b) DSc curves of the pure components and of five mixtures 1: acetanilide (x_{Ben}=0), 2: x_{Ben}=0.1, 3: x_{Ben}=0.4, 4: x_{Ben}= 0.578 (eutectic), 5: x_{Ben}=0.75, 6: x_{Ben}=0.9, 7: benzil (x_{Ben}=1)[57].

A second DSC run was performed on AuSn ANPs (Figure 4.28) with the same scanning conditions (40-500°C) as in the first run. The melting point this time was 417 ◌̊C which was the same as the bulk value. The significantly lower melting temperatures of Au-Sn ANPs in the first DSC run, along with the 417° C (almost the melting point of bulk) in the second DSC run, provide a strong motivation for the application of Au-Sn ANPs as solders for the environmentally friendly high-temperature electronics.

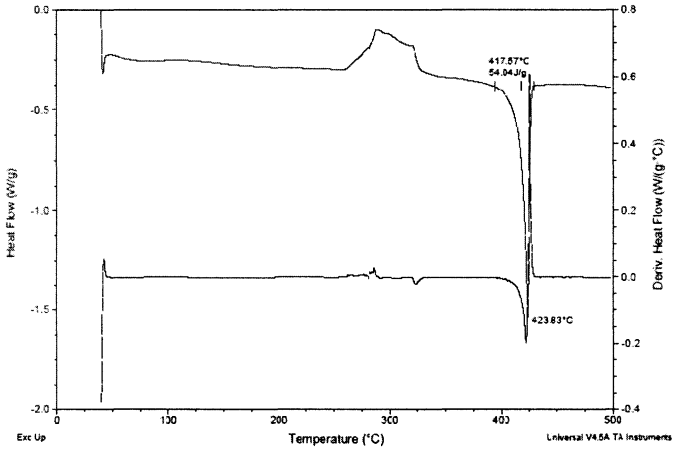

Figure4. 28: DSC of dried AuSn1:1ANPs in presence of PAA (at 80°C) shows a melting point of 417° C which is close to the bulk value (419° C) indicating the aggregation of Au-Sn ANPs after the first melting.

As mentioned in the experimental section, the co-reduction method has its own challenges for the synthesis Au-Sn alloy; therefore, the successive method can be a more reliable method. Also, it has been proved that alloying without ligand increases the amount of diffusion of two elements. Adding the ligands shortly after the alloying process prevents the system from growth and aggregation. Figure 4.29 shows that the Au-Sn ANPs (Au/Sn:1/1) in the presence of PAA, synthesized with successive method, has the lowest melting point. Also, Figure 4.30 shows that the melting point of two samples is

chosen based on the eutectic point of the Au-Sn system. With the increase in the amount of the Sn precursor, Sn NPs are formed along with Au-Sn ANPs and the melting point of Sn NPs is 160-170°C as reported by Jiang et al[59]. That is the reason for the increase in the melting point of Au-Sn ANPs (Au/Sn:1/19).

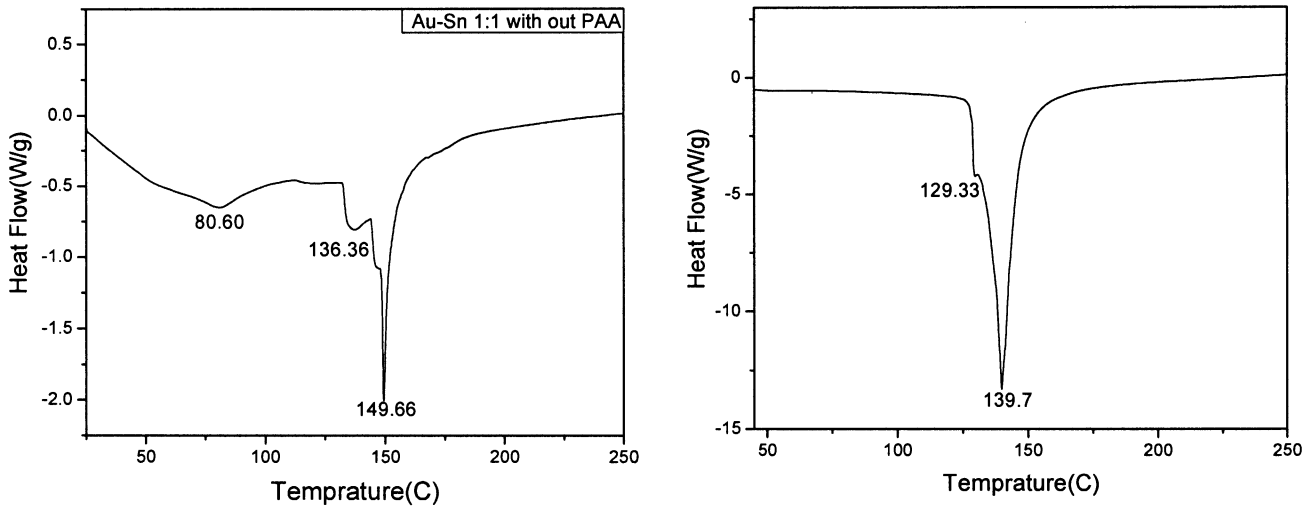

Figure 4.29: The DSC curve of Au-Sn ANPs (Au/Sn:1/1 with PAA and without PAA) synthesized by successive method.

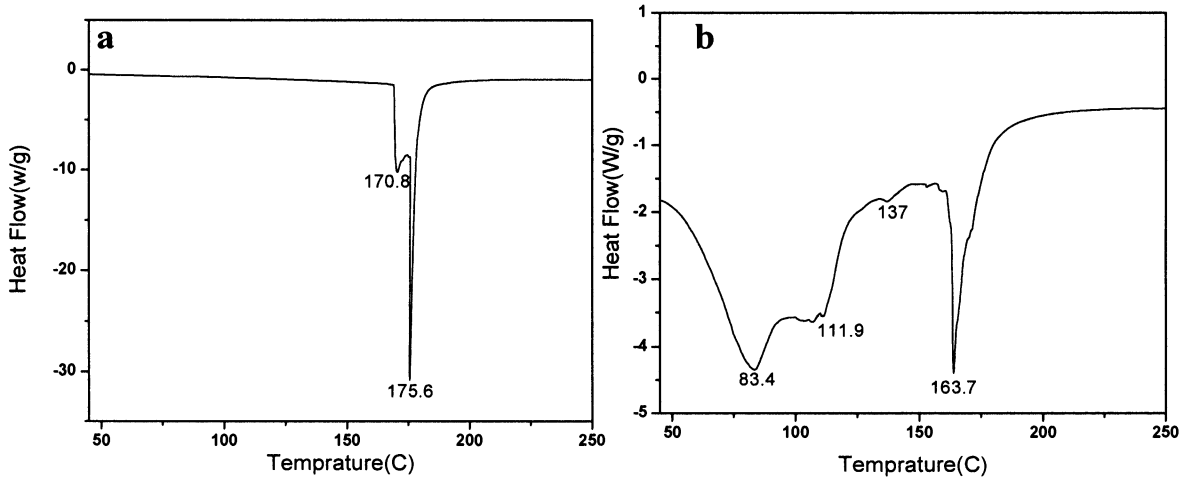

Figure 4.30: The DSC curve of Au-Sn ANPs ((a) Au/Sn:1/19 and (b)Au/Sn:4/1) in presence of CTAB which were synthesized by co-reduction method.

4.7 Conclusion

Au-Sn alloy nanoparticles (ANPs) are promising candidates for various applications such as lead-free electronics. Co-reduction method led to the formation of AuSn ANPs with significant reduction in melting temperature applicable for lead free high temperature electronics, but reproducibility is still a challenge. Also, it was found that in the absence of ligands, Sn, diffused more into the crystalline structure of Au therefore, the resultant alloy had higher Sn content. Furthermore, successive method for the synthesis of Au-Sn was found to be more reliable and repeatable, producing higher Sn content alloy with even lower melting point.

References

[1] H. Ardebili, M.G. Pecht, Encapsulation Technologies for Electronic Applications, Elsevier, 2009.
[2] H. Jiang, Ph.D. Thesis, Georgia Institute of Technology, Atlanta, GA, USA, April 2008.
[3] Y. Li, C.P. Wong, Recent advances of conductive adhesives as a lead-free alternative in electronic packaging: materials, processing, reliability and applications, Mat. Sci. and Eng. R, 51, 2006, 1-35.
[4] U. R. Kattner, Phase diagrams for lead-free solder alloys, JOM, Dec.2002, 45-51.
[5] J. Bath, Lead –Free soldering, Springer, 2007.
[6] I. Ohnuma, M. Miyashita, Phase equilibria and thermodynamic properties of Ag-Sn based Pb-free solder alloys, IEEE transactions on electronics packaging manufacturing, 26, 2003, 84-89.
[7] K. Minagawa, H. Kakisawa, Y. Osawa, S. Takamori, K. Halada, Production of Fine Spherical Lead-Free Solder Powders by Hybrid Atomization, Science and Technology of Advanced Materials, 6, 2005, 325–329.
[8] S.T.Kao, J.G. Duh, Effect of Cu Concentration of on Morphology of Sn-Ag-Cu by Mechanical Alloying. Journal of Electronic Materials, 33, 2004, 1445-1451.
[9] A. He, B. Djurfors, S. Akhlaghi, D.G. Ivey, Pulse plating of gold-tin alloys for microelectronic and optoelectronic applications [Online]. 2002. http://www.micralyne.com/newslyne/ausnpaper.pdf (accessed Dec 1, 2009) .
[10] S. Akhlaghi, D.G. Ivey, Effect of processing parameters on the electroplating of Au-Sn solders [Online]. 2003. http://www.micralyne.com/pdfs/AuSnSilverMedal_AESFpaper.pdf (accessed Dec 1, 2009).
[11] N. Morawej, D.G. Ivey, S. Akhlaghi, [Online]. 2006. http://www.micralyne.com/pdfs/GraduateStudentAward.pdf (accessed Dec 1, 2009).
[12] H. Okamoto, The Ni-Sn (Nickel-Tin) System, Journal of Phase Equilibria, 29, 2008, 297-298.
[13] T. Takahash, M. Tadauchi, Experimental investigation on Sn-Ni-Cu interaction at high temperature, J. Mat. Sci., 41, 2006, 281-283.
[14] H. Okamoto, The Cu-Sn (Copper-Tin) System, Journal of Phase Equilibria, 1, 87-89.
[15] Z. N. Ivoninskaya, A. R. Regel, Phase diagram of the Bi-Sn system in the liquid and solid states, Russian Physics Journal, 10, 1967, 32-34.
[16] Jungoo Lee, Joonho Lee, Phase diagrams of nanometer-sized particles in binary systems, JOM, march 2005, 56-59.
[17] H. Jiang, K.S. Moon, Synthesis of Ag-Cu alloy nanoparticles for lead-free interconnect materials, IEEE 2005.
[18] K.W. Moon, W.J. Boettnger, Experimental and thermodynamic assessment of Ag-Sn solder alloys, J. Electron Materials, 29, 2000, 1122-1134.
[19] R. S. Sidhu, S. V. Madge, On the Nature of the Interface between Ag_3Sn Intermetallics and Sn in Sn-3.5Ag Solder Alloys, J. Electron Materials, 36, 2007, 1615-1620.
[20] M. Ochiai, T. Akamatsu, Reliability of solder joint assembled with lead free solders, FUJITSU Sci. Tech. J., 38(1), 2002, 96-101.

[21] I. Karakaya, W.T. Thompson, The Ag-Sn (Silver-Tin) System, Bulletin of Alloy Phase Diagrams, 8, 1987, 343-347.
[22] P.T. Vianco, J.A. Rejent, Properties of Ternary Sn-Ag-Bi Solder Alloys: Part II—Wettability and Mechanical Properties Analyses, J. Electronic Materials, 28(10), 1999, 1138-1143.
[23] S. Yamamoto, A. Momota, Preparation of fine particles of tin–M (M: silver, bismuth) alloys with ammonia splashing method, Journal of Materials Processing Technology 137, 2003, 123–127.
[24] A. Verma, T.R. Anantharaman, Internal oxidation of rapidly solidified silver-tin-indium alloy powders, J. Mat. Sci., 27, 1992, 5623-5628.
[25] C.Y. Linb, U.S. Mohantya, Synthesis and characterization of Sn–3.5Ag–XZn alloy nanoparticles by the chemical reduction method, Journal of Alloys and Compounds, 472(1-2), 2009, 281-285.
[26] Li-Yin Hsiao, Jenq-Gong Duh, synthesis and characterization of lead-free solders with Sn-3.5 Ag-xCu(x=0.2,0.5, 1) alloy nanoparticles by the chemical method, J. Electrochemical Society, 152(9), (2005), J105-J109.
[27] A. Verma, T.R. Anantharaman, Internal oxidation of rapidly solidified silver-tin-indium alloy powders, J. Mat. Sci., 27, 1992, 5623-5628.
[28] Z. Xia, Z. Chen, Effect of Rare Earth Element Additions on the Microstructure and Mechanical Properties of Tin-Silver-Bismuth Solder, J. Electron Materials, 31, 2002, 564-567.
[29] M. Pei, J. Qu, Effect of Lanthanum Doping on the Microstructure of Tin-Silver Solder Alloys, J. Electron Materials, DOI: 10.1007/s11664-007-0335-x, 2007.
[30] J. Shen, Y.C. Liu, Strengthening effects of ZrO_2 nanoparticles on the microstructure and microhardness of Sn-3.5Ag lead-free solder, Mat. Sci. and Eng. A, 441, 2006, 135-141.
[31] Fei-Yi Hung, Hung-Mao Lin, A study of the thin film on the surface of Sn–3.5Ag/Sn–3.5Ag–2.0Cu lead-free alloy, 415, 2006, 85-92.
[32] Fei-Yi Hung, Hung-Mao Lin, A study of the thin film on the surface of Sn–3.5Ag/Sn–3.5Ag–2.0Cu lead-free alloy, 415, 2006, 85-92.
[33] T. H. Kim, Young-Ho Kim, Sn-Ag-Cu and Sn-Cu Solders: Interfacial Reactions with Platinum, JOM, June 2004.
[34] T. H. Kim, Young-Ho Kim, Sn-Ag-Cu and Sn-Cu Solders: Interfacial Reactions with Platinum, JOM, June 2004.
[35] F. Gao, S. Mukherjee, Synthesis, characterization, and thermal properties of nanoscale lead-Free solders on multisegmented metal nanowires, J. Phys. Chem. C, 113, 2009, 9546–9552.
[36] W. D. Callister, Materials science and engineering and introduction, Wiely, 2003.
[37] R. A. Swalin, Thermodynamics of solids, Wiely, 1972.
[38] G. Ghosh, Phase stability and cohesive properties of Au-Sn intermetallics: A first-principle study, J. Mat. Res., 23, 2008, 1398- 1416.
[39] H. Okamoto, The Au-Sn (Gold-Tin) System, Journal of Phase Equilibria, 14, 1993, 765-766.
[40] K. J. Lee, B. H. Jun, Environmentally friendly synthesis of organic-soluble silver NPs for printed electronics, Nanotechnology, 18, 2007, 1-5.

[41] F.Yunzhi, D. yokou, Shape-controlled synthesis of highly monodisperse and small size gold nanoparticles , Science in China Series B: Chemistry, 50, 2007, 494-500.
[42] K. Yu, Z. Wu, Q. Zhao, B. Li, Y. Xie, High-Temperature-Stable Au@SnO_2 Core/Shell Supported Catalyst for CO Oxidation. Phys. Chem. Lett. C., 2008, 112, 2244-2247.
[43] H. Mori, H.Yasuda, Alloy phase formation in nanometer-size particles. Materials Science and Engineering A, 2001, 312, 99- 103.
[44] H. Yasuda, K. Mitsuishi, H. Mori, Particle- size dependence of phase stability and amorphous like phase formation in nanometer-sized Au-Sn alloy nanoparticles. Physical Review B.,64, 2001, 094101-1–6.
[45] B.L.Abram, P. H. Holloway, Role of the surface in luminescence process, Chem. Rev., 104, 2004, 5783-5801.
[46] A. Henglein, M. Giersigahal, Radiolytic formation of colloidal Tin and Tin-Gold particles in aqueous solution, J. Phys. Chem., 1994, 98, 6931-6935.
[47] N. Dahal, V. Chikan, Synthesis of Water-Soluble Iron-Gold Alloy Nanoparticles. Chem. Mat. 2008, 20, 6389- 6395.
[48] N. Tian, Z. Y. Zhou, Synthesis of tetrahexahedral platinum nanocrystals with high-index facets and high electro-oxidation activity, Science, 316, 2007, 732-735.
[49] P. Bunzel, PhD Thesis, Saarland University, 2004.
[50] M. Herlach, Solidification and crystallization, Wiley, 2003.
[51] M. Herlach, Phase transformations in multicomponenet melts, Wiley, 2008.
[52] Y.X. Wang, Elastic and Electronic Properties of TcB_2 Superhard ReB_2: First Principle Calculation, Appl. Phys. Lett.,91, 2007, 101904-1-101904-3.
[53] S. M.Woodely, P.D. Battle, Computer Simulation Study of the Orthorhombic-Hexagonal Phase Change in Lanthanide- Magnate, Chem. Mat., 15, 2003,1669- 1675.
[54] G. Ghosh, Phase stability and cohesive properties of Au–Sn intermetallics: A first-principles study, J. Mater. Res., 23(5), 2008, 1398-1416.
[55] J. Weissmuller, P. Bunzel, Two –phase equilibrium in small alloy particles, Scripta Materials, 51, 2004, 813-818.
[56] G. Wilde, P. Bunzel, Phase equilibria and phase diagrams of nano-scale systems, J. Alloy and compounds, 434-435, 2007, 286-289.
[57] G. Hohne, W. Hemminger, Differential scanning Calorimetry; an introduction for practitioner, Springer, 1996.
[58] W. Hemminger, G. Hohne, Calorimetry,; Fundamentals and Practice, Verlag Chemie, 1984.
[59] H. Jiang, K. S. Moon, Size-dependent melting properties of tin nanoparticles Chemical Physics Letters, 429, 2006, 492-496.

Chapter 5

5.1 Introduction

Generally, properties of alloy nanoparticles (ANPs) (or bimetallic systems) strongly depend on their structure, chemical composition and atomic arrangements. In the nanometric scale, bimetallic clusters can form in different configurations such as core-shell[1], mixed (alloyed) structure, sub-cluster segregation and alloyed- shell structures depending on the properties of both elements and the synthesis methods. However, to the author's knowledge, the specific property (or properties such surface energy, atomic size and etc.) of elements that play a key role in the determination of the types of configurations of alloy nano-scale particles (ANPs) have not been discussed in literature. The type of configurations is generally not a theme relevance to microstructures and only the miscibility and immiscibility of elements are addressed using Hume Rothery rules. The Ag-Ni alloy is a system that has been rarely studied at bulk and less application has been reported for this system. In the present chapter, Ag-Ni ANPs were studied because the two elements are immiscible with each other (at the micro-scale) and monitoring the formation of Ag-Ni ANPs can lead to a better understanding and design of the alloying process at the nano-scale. Alloyed structure of Ag-Ni at nano-scale may show properties and characteristics which are different from the core-shell structure and may reveal novel properties for new technologies. In some metallic systems (ANPs) formation of core-shell structure is preferred under the equilibrium condition and the element with the larger atomic size, lower surface energy and better bonding to the surface ligand tends to segregate on the surface. Miscibility of two metals in nanostructures is more complicated than in bulk and here among other parameters, we discuss the effect of ligands on the

formation of ANPs. Ag-Ni ANPs reported to form a core-shell structure were confirmed with both theory and experiment.[2] Ni, which has an atomic radius smaller than that of Ag, tends to occupy the more sterically confined core, and Ag, which has lower surface energy (S_{Ag}=1.12, S_{Ni}=1.81 (J/m2))[3] tend to segregate . Still this question, remain, why does alloying of immiscible elements occur at nano-scale? The solid solubility of metallic elements increases significantly due to the enhancement of atomic diffusion up to magnetite of 10^8 times at the nano-scale which results in alloying even at room temperature. Therefore, alloying of immiscible elements such as Ag-Fe[4] and Ag-Ni[5] at nano-scale is possible.

As mentioned above, Ag and Ni are two elements which are completely immiscible in both liquid and solid states and therefore, to synthesize Ag-Ni ANPs either a strong reducing agent such as hydrazine or a source of energy (laser or γ radiation, heat treatment) is required. The nanostructure prepared by these methods usually contains the crystallites with different crystallographic orientations and/or chemical compositions which are far from thermodynamics equilibrium (but kinetically favored) depending on the mode of preparation and time- temperature history[6,7].

Here, the synthesis of immiscible Ag-Ni ANPs is reported, in particular, avoid the formation of core-shell particles which is more favored by thermodynamics at room temperature in the presence of sodium citrate and sodium borohydrate (mild capping agent and reducing agent). Formation of ANPs has been studied with and without ligand for better understanding of the alloying process and the role of capping agent leading to better design of the ANPs structures. First, a brief background of Ag-Ni alloy in both micro and nano-scale is provided:

Ag-Ni alloys are used in electrical contacts and switches. Chang et al has reported the application of thin film of Ag-Ni coating as protective coating on electrical terminals of separable electrical connector. This coating is made of a nanocomposite material with an average grain size of about 5 to 50 nanometers in which Ag is the matrix (soft part) and the harder part, Ni, is dispersed in the matrix. The volume fraction of Ni significantly influences the fretting wear resistance of the coating. Ag-Ni nanocomposite shows better wear resistance property, low contact resistance, thermal stability up to 150°C, and low friction coefficient[8]. Prior to this report Ag-Ni composite was used for electrical contacts, particularly intended for spark plug electrodes[9]. Ni- based alloys have attracted great attention due to their technologically important catalysis and magnetic properties. Some other Ni-based systems have been reported to improve the catalysis property of noble metals such as Au and Pt. Catalysis property of Ni-Au ANPs supported by SiO_2 and $MgAl_2O_4$ was studied by Monte Carlo simulations and experimentally verified using a combination of in situ X-ray absorption fine structure (XAFS), transmission electron microscopy (TEM), and in situ X-ray powder diffraction (XRD)[10]. Pt-Ni intermetallic alloy demonstrates enhanced elctrocatalytic activities for the oxygen reduction reaction, compared with that of Pt[11]. Heat treatment is another method to synthesize Ag-Ni ANPs by first, immersing fatty acid (stearic acid) films in Ag^+ and Ni^+ solution and then thermally evaporating the fatty acid. The disadvantage of this method is the formation of mixtures of nanoparticles of Ag, Ni and Ag-Ni ANPs and in addition, the ANPs are not stable above 100°C[12]. Ag-Ni ANPs were synthesized by reducing both metallic precursors by hydrazine with various molar ratios and embedded in epoxy for the investigation of electromagnetic waves absorption properties in 2-40 GHz[13]. Although

the core-shell structure is favored thermodynamically for Ag-Ni ANPs, recently Zhang et al[14] reported the synthesis of Ag-Ni ANPs at room temperature with a high dose gamma radiation (creating a kinetically favorable environment to form alloy structure). The Ag-Ni ANPs so prepared were stable up to 125°C for 6h and 100°C for 9h in vacuum, with no de-alloying observed.

Ingen et al. used pulsed laser irradiation and vapor quenching to deposit polycrystalline non equilibrium Ag_xNi_{1-x} solid solutions at room temperature. Ag and Ni are immiscible in liquid and solid state, hence instead of liquid quenching, vapor quenching was used to produce the alloy[15,16]. Ag- Ni metastable nanorods with 30-50 nm and 300-500 length have also been made by pulsed laser induced liquid/solid interfacial reaction[17]. Further, Poondi et al. synthesized metastable Ag- Ni alloy by wet chemical and laser- liquid- solid interaction technique where the final products contained Ag, Ni, NiO NPs and Ag-Ni ANPs[18]. Che Lee et al. recently reported formation of various molar ratios of Ag-Ni ANPs using the reduction of Ag nitrate and Ni nitrate in ethylene glycol with hydrazine in presence of polyethyleneimine (PEI), spontaneously. ANPs formed here were super paramagnetic with FCC structure and mean diameter of 6.3-7.2 nm[19].

5.2 Ag-Ni phase diagram

Table 5.1 shows the characteristic of both elements Ni and Ag. Based on Hume-Rothery[20] rule the atomic radius difference between Ag and Ni is 13.2% indicating that the two elements are immiscible. Phase diagram shows the immiscibility of elements in both liquid and solid state[21].

Table 5.1: Characteristics of Ni and Ag.

characteristic of elements	Atomic radius (nm)	Crystal structure	Electron configuration	Surface energy* (J/m^2)	Chemical potential (eV)
Ag	0.144	FCC	[Kr] $4d^{10}$ $5s^1$	1.12 ± 0.065	0.8
Ni	0.125	FCC	[Ar] $3d^9$ $4s^1$	1.81±0.18	-0.25

The Ag-Ni system is a monotectic system and also includes eutectic reactions at below temperature and compositions:

L1	1435°C	Ni (s) + Ag(l)	monotectic reaction (1)
L2	1435°C	Ni(s) + Ag(l)	monotectic reaction (2)
L	960°C	Ni(s) + Ag(s)	eutectic reaction (3)

The melting point of Ag and Ni are 962°C and 1455°C, respectively, which is close to eutectic and monotectic point. The position of the first monotectic reaction is placed at 3% Ag and the second one at 99.11% Ag. Based on calculations, the eutectic reaction took place at 99.822% Ag (99.67% Ag based on experiment) at 960°C which is close to the melting point of Ag.

The limit of solid solubility of Ni in Ag was determined through the measurement of the magnetization of equilibrated and quenched alloy. The below table is the measurements of G. Tammann and J. Ladet solubility of Ni in Ag[14].

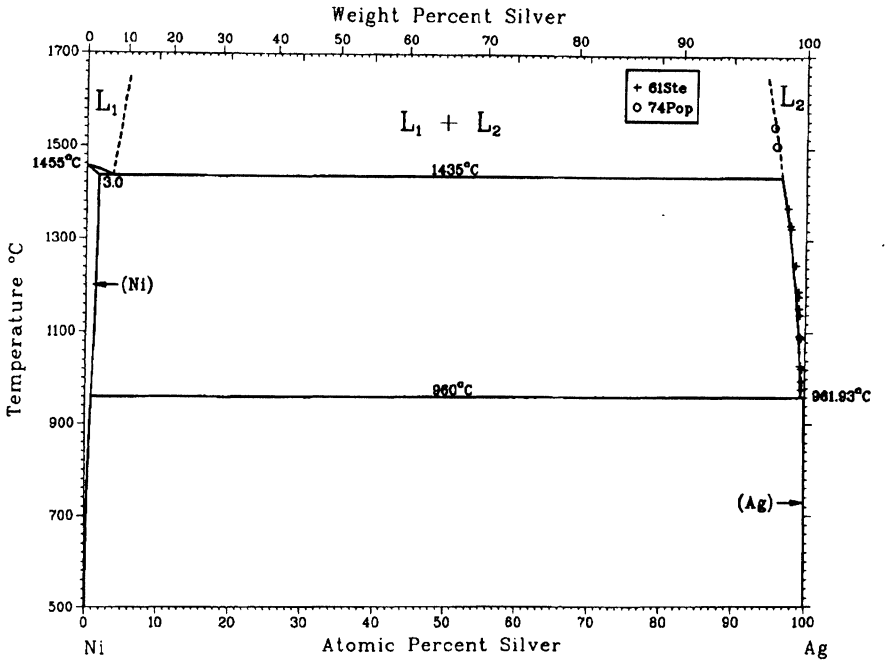

Figure 5.1: Phase diagram of Ag-Ni alloy[14].

Table 5.2: By increasing the temperature solubility of Ni in Ag crystalline structure increases and the maximum solubility of Ni in crystalline structure of Ag is up to 1% was determined by M. Singleton and P. Nash[14].

Reference	Composition, at.% Ag	Reaction °C
[30Tam]	99.813	922
	99.846	860
	99.879	785
	99.919	702
	99.941	640
	99.952	600
	99.967	510
	99.978	400
[76Lad]	99.790	912
	99.813	881
	99.831	865
	99.862	834
	99.890	808
	99.903	788
	99.916	767
	99.936	750
	99.924	748
	99.941	733
	99.937	724
	99.957	674
	99.974	631

5.3 Experimental Section

Ag-Ni ANPs are synthesized by a co-reduction method at room temperature. Silver nitrate ($AgNO_3$), nickel nitrate ($Ni(NO_3)_2$. $6H_2O$) as metallic precursors, sodium citrate ($Na_3C_6H_5O_7$), polyvinyl alcohol (PVA, $(C_2H_4O)_x$) as the ligands and sodium borohydrate ($NaBH_4$) as a reducing agent were used. 50 ml of 10^{-4} M aqueous solution of silver nitrate and 50 ml of 10^{-4} nickel (II) nitrate were mixed together and sodium citrate was added as a capping agent, and then sodium borohydrate was added to reduce nickel and silver nitrate spontaneously. Solution turned to yellow color by adding the reducing agent (Figure 5.2). One of the challenges in this method is the reduction of Ni and Ag together at room temperature under similar experimental condition, since standard reduction potential of Ni and Ag is not close enough ($E_0(Ni^{+2}/Ni)$ =-0.25V and $E_0(Ag^{+}/Ag)$= 0.8V) and in presence of sodium citrate mixture of the Ag NPs and Ag-Ni ANPs are formed. UV spectroscopy measurements of the solution were performed on a Perkin Elmer photometer operated at a resolution of 2 nm. The specimen for TEM was prepared by dropping the solution on holey carbon grid and dried in vacuum. To determine whether de-alloying happened in Ag-Ni ANPs, TEM grid was heated up to 125°C for 13h. Size, distribution, and morphology of ANPs were determined by JEOL 2100 (200 kV) field emission gun transmission electron microscope (JEM 2100F TEM) equipped with Gatan imaging filter. The instrument is equipped with Z-contrast capability in high annular dark-field (HAAF) mode and also with energy dispersive X-ray (EDX) analysis for elemental analysis.

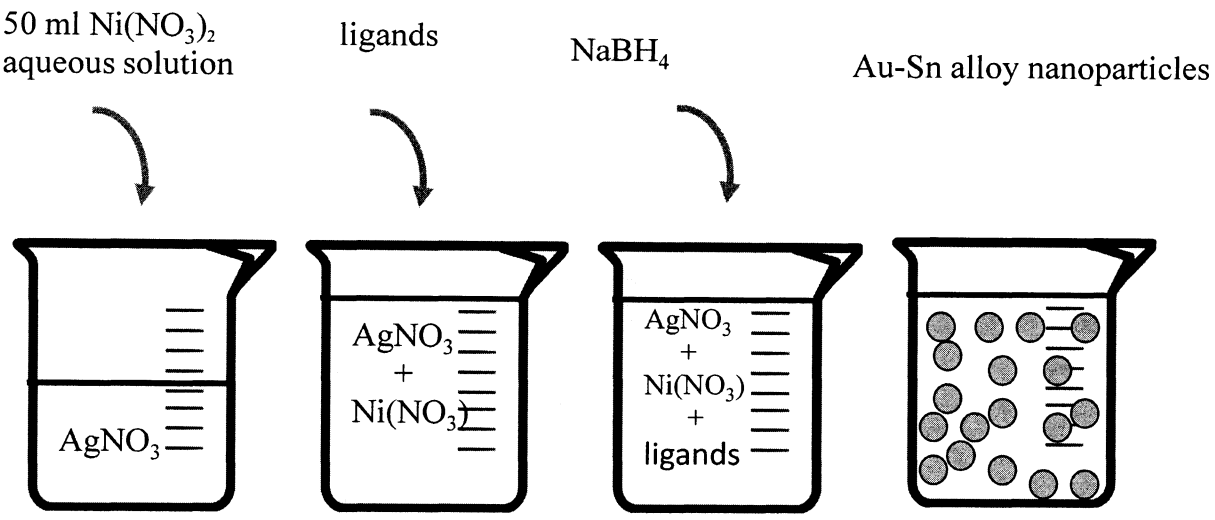

Figure 5.2: Experimental schematic for synthesize process of Ag-Ni ANPs with reduction method (co-reduction) at room temperature in the presence of sodium citrate. By using PVA the ANPs leads to the formation of grey color particles.

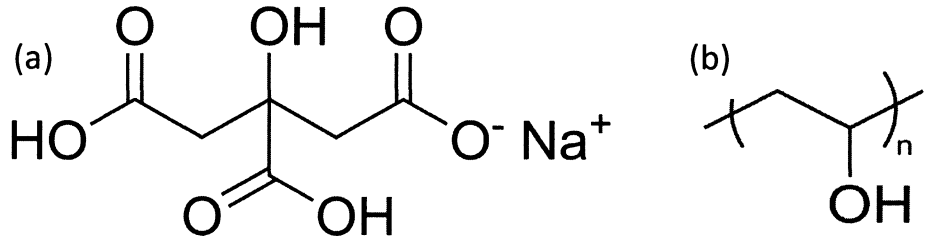

Figure 5.3: Schematic of ligands a) Sodium citrate b) Polyvinyl alcohol (PVA). ANPs synthesized in the presence of PVA contain more Ni %. Polyvinyl alcohol with the shorter chain will less perturb the alloying process and in this case, more Ag and Ni ion can be reduced together.

Stable Ag NPs were synthesized as control sample with the same experimental conditions used for the Ag-Ni ANPs. Figure 5.4 A) shows polydisperse Ag NPs and Figure 5.4 B) Ag-Ni ANPs with size ranges of 10-20nm. The co-reduction method usually random nucleation and growth leading to disordered structure and distorted crystal shape[22]. In

these figures, the morphologies of both particles are similar which are quite spherical with twinned and multi-twinned structures[23] and there is no significant change observed in the morphology of Ag and Ag-Ni ANPs.

Proper surfactant during the chemical reduction process might play a key role in controlling the size distribution of ANPs, but still controlling precisely the size distribution of ANPs is a challenge. Ni NPs cannot be synthesized under the same conditions; even with excess amount of sodium borohydrate, as the reduction of aqueous solution of Ni nitrate is not possible at room temperature. From above discussion one can conclude that Ag ion plays a role (maybe catalysis role[24]) in reduction process of Ni ions. Ni NPs were reported to be synthesize at elevated temperature in the range of 50-100°C mostly reduced by hydrazine[25,26,27], although Hou et al. reported using sodium borohydrate with trioctylphosphine oxide (TOPO) and hexadecylamine (HDA) to synthesis size controlled Ni NPs[28].

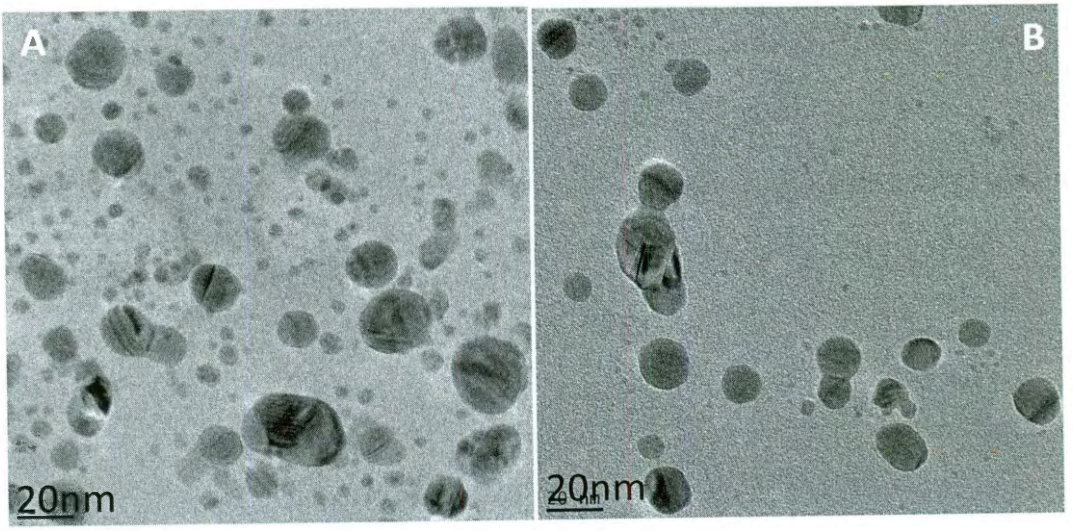

Figure 5.4: A) Ag-Ni ANPs B) Ag NPs, no difference in morphology of Ag-Ni ANPs and Ag NPs in the presence of sodium citrate and both have twins and multi twins in their structures.

5.4 Characterization of the Ag-Ni alloy nanoparticles (ANPs)

UV spectroscopy was performed shortly after the reaction was completed. Figure 5.5 shows that the surface plasmon resonance of the Ag-Ni ANPs is dampened, broadened and shifted toward higher wavelength at 404 nm compared to the surface plasmon resonance of Ag NPs at 382nm. Dampening and broadening are the result of decreasing particle size[29], and peak shift is mainly the result of the change in the composition (alloying), although Cottancin et al. reported a slight shift with decreasing the size for Ag NPs and larger shift for Au NPs[30]. Mie theory predicts a broad and weak surface plasmon band around 330nm for pure Ni when dielectric constant of the bulk alloy is considered for the calculation of the absorption band. Guardy et al. reported no plasmon band for Ni. These could be the reason why introducing Ni to Ag based solid solution could cause the broadening of peaks in the absorption spectra. After nearly 75 days, the spectra for Ag-Ni ANPs is slightly blue shifted and broadened, possibly because of the oxidation of Ag and Ni.

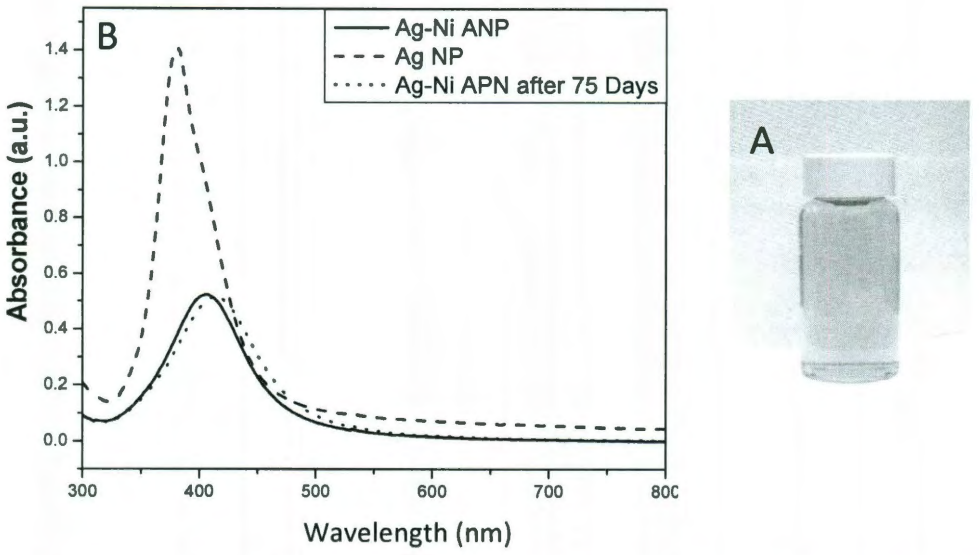

Figure 5.5: A) Image of Ag-Ni ANPs solution B) UV spectroscopy of Ag NPs and Ag-Ni ANPs shows that within the alloying process the absorption band has dampened, broadened and shifted. After 75 days abortion band of Ag-Ni ANPs shifted and broadened which could be caused by the oxidation of the alloy.

TEM was employed to determine structure, morphology, size distribution and composition of the Ag-Ni ANPs[31,32]. For better characterization of NPs the selection of proper technique (bright field or dark field) is important[33]. Gatan imaging filter (GIF) image (Figure 5.6) shows the distribution of both elements of Ag and Ni in individual particle. As we have discussed before core- shell structure $Ag_{shell}Ni_{core}$ is favored thermodynamically for this monotectic system. The reason is that large lattice mismatch, and lower surface energy of Ag leads this system to segregation which was predicted by theory and other experimental results; our observations for Ag-Ni APNs is surprising.

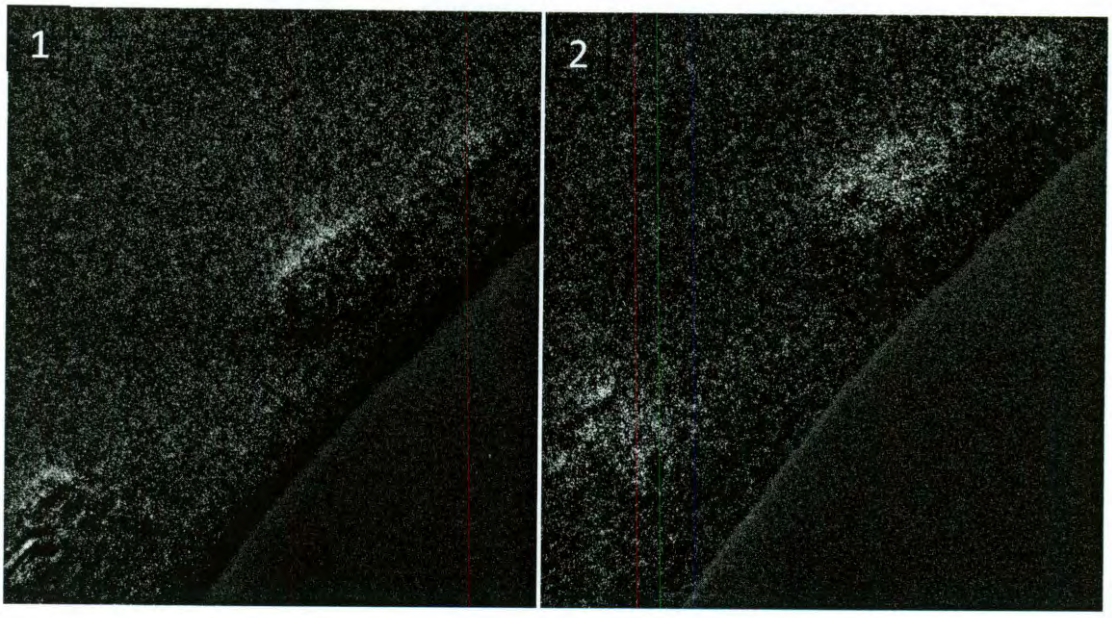

Figure 5.6: Gatan Image Filter (GIF) of Ag-Ni ANPs shows heterogeneous distribution of Ag and Ni. 1 and 2 shows the distribution of Ag and Ni, respectively.

High Angle Annular Dark Field (HAADF) is a powerful technique to study core-shell structures, defects, and twinned specimens, because of better contrast compared to other TEM techniques, and it is known as Z-contrast imaging. When the elements are far from each other in the table of element (large difference between Z values) the contrast in HAADF would be better. In this technique, parallel beam would be blocked and images are produced by only diffracted beam which is related to the dark region in the HAAD image. Figure 5.7 a) and b) HAADF and HRTEM image of Ag-Ni ANPs (in presence of sodium citrate) shows no core–shell structure and instead twins and multi-twinned structure of ANPs can be easily observed. On the nanometer scale, metals (most of them are facecentered cubic, or fcc) tend to nucleate and grow into twinned and multiple twinned particles (MTPs) and Ag, Ni and their alloy ($Ag_{0.5}Ni_{0.5}$) have FCC structures[34].

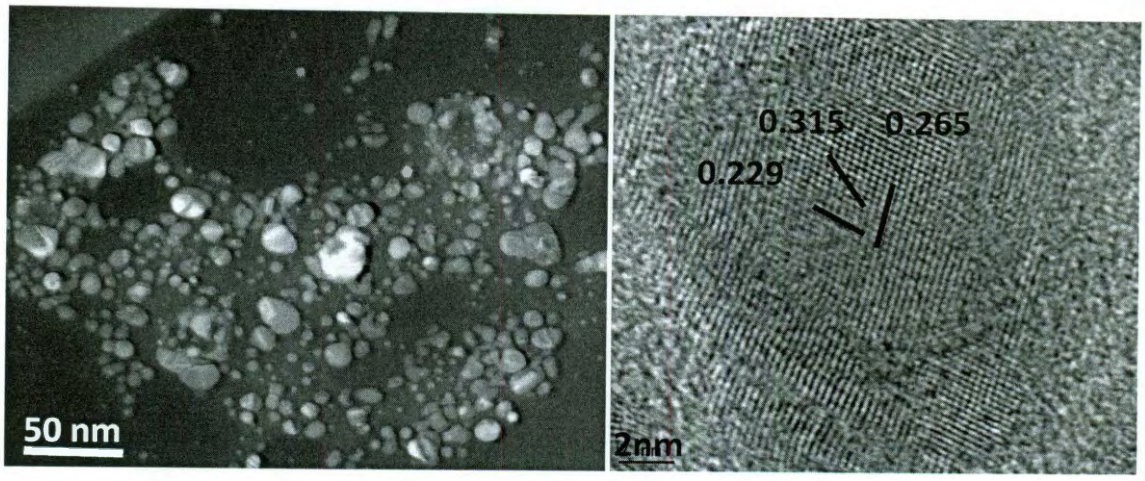

Figure5. 7: High angle annular dark field (HAADF) and high resolution transmission electron microscopy (HRTEM) images show Ag-Ni ANPs are not core–shell structures and instead twin and multi-twin structures were observed.

Figure 5.8 is the Energy Dispersive X-Ray Spectroscopy (EDS) from the individual Ag-Ni ANPs in the presence of sodium citrate confirming the existence of both elements. Particles capped with PVA show higher content of Ni. Our experimental result shows when the alloying process occurs without ligand, particles have a higher content of Ni in the individual particles, but particles are not stable and aggregate in less than 24 hours. When the surface of both elements are ligand free, Ni is able to diffuse more into the crystalline structure of Ag and provides a particle with high content of Ni, but still further study is required to optimize the system when is the proper time to add ligands that would let the alloying proceed sufficiently enough and then, the next step, adding ligands to stabilize the system.

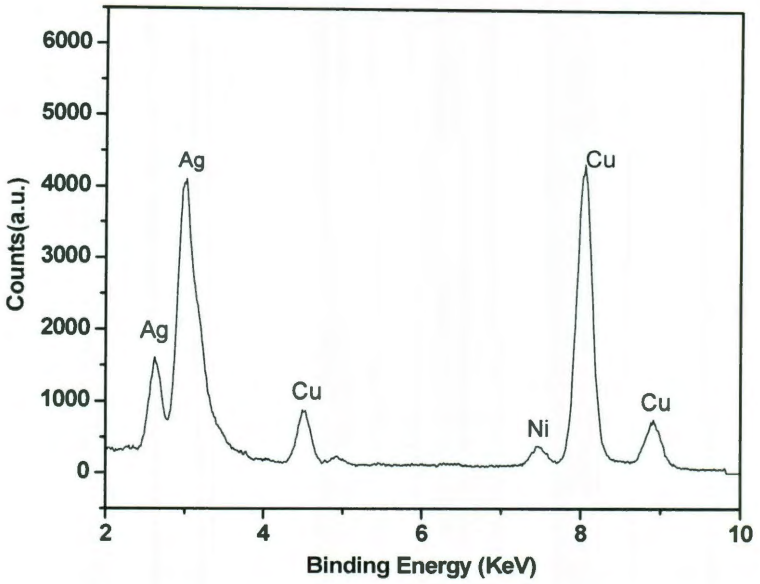

Figure5. 8: Energy Dispersive X-Ray Spectroscopy (EDS) from the individual Ag-Ni ANPs in the presence of sodium citrate (deposited on the holey carbon copper grid) confirming the existence of both elements.

Figure 5.9 a) The electron diffraction of mixture of Ag and Ag_2O_2 NPs and $Ag_{0.5}Ni_{0.5}$ ANPs after synthesis in the presence sodium citrate. b) The electron diffraction of heated Ag-Ni ANPs at 125° C for 13 hours in vacuum which confirms that ANPs are stable even after heating.

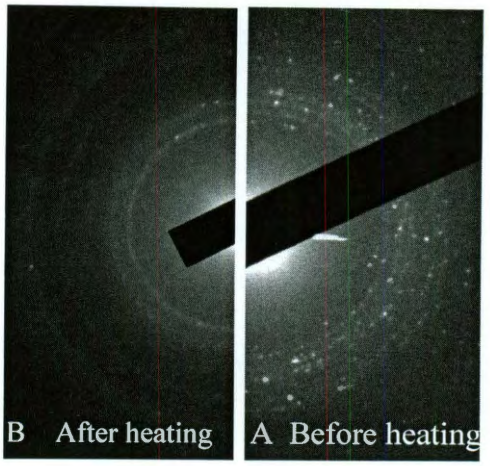

Figure 5.9: A) Electron Diffraction (ED) of mixture of Ag and Ag_2O_2 and $Ag_{0.5}Ni_{0.5}$ ANPs in presence of sodium citrate (d= 0.315, 0.293, 0.268, 0.246, 0.229, 0.215). B) After formation of Ag-Ni ANPs, sample was heated up to 125°C for up to 13 hours and $Ag_{0.5}Ni_{0.5}$ with a cubic structure were formed.

Annealed Ag-Ni ANPs at 125°C for 13 hours in vacuum has a cubic structure with a lattice constant of 3.83Å (pdf No. 04-002-1346). Figure5.9 b) shows the existence of Ag, Ag_2O_2 and $Ag_{0.5}Ni_{0.5}$ ANPs in the sample and many peaks exist in the electron diffraction of sample. Same sample were characterized with XRD (Figure 5.10). Only three peaks were observed in the XRD pattern which is belong to Ag (2θ =38.09, 44.33, pdf: 04-002-1346) and Ag_2O_2 (2θ =34.18, pdf: 00-051-0945). XRD pattern does not show the formation of $Ag_{0.5}Ni_{0.5}$ ANPs can be because the yield of alloying process is low and also, limitation of XRD technique that as I mentioned in chapter 3 (less peaks are observable in XRD pattern).

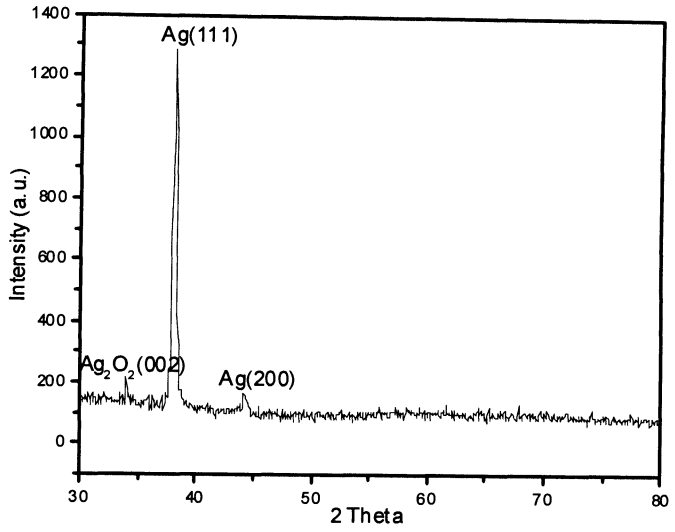

Figure 5.10: XRD pattern of Ag-Ni ANPs prepared from same batch as sample prepared for TEM in Figure 5.9 A. XRD shows only 3 peaks, but TEM shows many more rings, confirms that TEM is still more reliable method for characterization of ANPs. XRD pattern reveals the formation of Ag (pdf No. 04-003-1472) with cubic structure and Ag_2O_2 (pdf No.00-051-0945) with monoclinic structure.

Lattice spacing and lattice constant of Ag and Ni are compared with $Ag_{0.5}Ni_{0.5}$ structure in Table 5.3. Crystalline structure of Ag undergoes contract during the alloying process base on Bragg law ($\lambda = 2d \sin 2\theta$) when 2θ of Ag shifted towards the larger values.

Table 5.3: The lattice spacing and lattice constant of Ag and Ni compared with $Ag_{0.5}Ni_{0.5}$ structure

plane	$2\theta_{Ag}$	$2\theta_{Ni}$	$2\theta_{Ag0.5Ni0.5}$	d_{Ag}(Å)	d_{Ni}(Å)	$d_{Ag0.5Ni0.5}$(Å)
(111)	38.78	44.83	40.77	2.32	2.02	2.21
(200)	44.14	52.22	47.43	2.05	1.75	1.91
(220)	64.67	76.80	69.33	1.44	1.24	1.35
(311)	78.30	93.21	83.67	1.22	1.06	1.15

Vegard's law predicts that the crystal lattice of alloys (for elements with the same structure) has linear relation with the composition of the alloy at constant temperature, and based on that the lattice spacing of $Ag_{0.5}Ni_{0.5}$ for (111) plane is predicted to be 0.220nm. This result is in agreement with reported experiment of Ingen, who deposited polycrystalline Ag_XNi_{1-X} solid solution film with laser ablation. When the composition of 100 nm film reached $Ag_{26}Ni_{74}$ the lattice constant calculated was 3.6916 Å suggesting that introducing more Ni to the Ag structure leads to more structural contraction, contrary to the positive deviation reported by Liu et al for crystalline structure of Ag-Ni nanorod using the pulsed- laser method.

Figure 5.11 shows that by heating the Ag-Ni ANPs for up to 13h at 125°C larger particles are formed with the aggregation of small NPs due to the degradation of capping agent from the surface of NPs at 125°C. Shape and size of these aggregated particles depend on the temperature and bonding between individual particles. The driving force for the coalescence of aggregated particles is minimization of surface energy at interfaces, grain boundaries and defects[35]. In the STEM mode, focused electron beam is used to map Ag and Ni to determine the chemical elemental distribution in ANPs. Mapping shows the homogenous distribution of both Ag and Ni, and this indicates that the heating up to 125°C for 13 h has led to the diffusion and homogenization of the elements in ANPs.

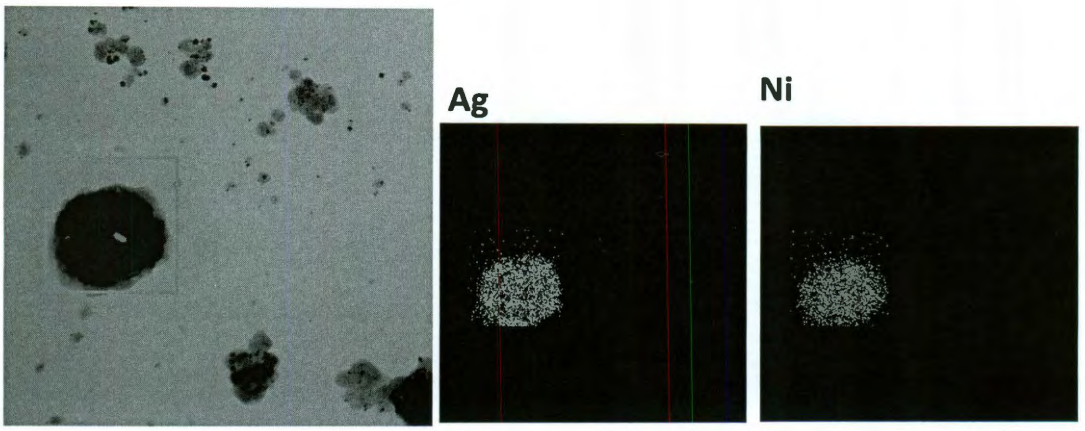

Figure 5.11: Mapping of Ag-Ni ANPs in STEM mode shows the homogenous distribution of Ag and Ni in each particle after annealing at 125°C for 13 h.

5.5 Conclusion

In summary, stable Ag- Ni ANPs are successfully synthesized with diameters in the range of 10-20 nm by the co-reduction method at room temperature. Gatan Image Filter (GIF) indicates that both Ag and Ni exist in the individual particles. HRTEM and HAADF-STEM suggest that ANPs produced by this method do not have core-shell structure. In the alloying process ligands play an important role: ligands with shorter length may less perturb the alloying process and in this case, Ni diffuses more in the crystal structure of Ag. Polyvinyl alcohol (PVA) (with shorter length) leads the alloy system to the formation of particles with higher content of Ni. In the presence of sodium citrate, mixture of Ag, Ag_2O_2 NPs and Ag-Ni ANPs is formed and without ligands, the yield of the system is improved up to 100%, but still this challenge remains: what is the optimum time to add ligands after co-reduction of both Ag and Ni. Ag-Ni ANPs were annealed at 125°C to study the stability of ANPs and the system led to aggregated structures and electron diffraction from these particles confirms the formation of $Ag_{0.5}Ni_{0.5}$ APNs with cubic structure.

References

[1] N. Sounderya, Y. Zhang, Use of core-shell structured nanoparticles for biomedical applications, Recent Patents on Biomedical Engineering, 1, 2008, 34-42.
[2] A. Agüero, J.M. Albella, Surface-Sandwich Segregation Phenomena in Bimetallic Ag-Ni and Pd-Ni Nanoparticles: A Molecular Dynamics Study, Defect and Diffusion Forum, 289 – 292, 2009, 657-664.
[3] R. H. Swalin, Thermodynamics of solids, Wiley, 1979, chap. 10, p. 231.
[4] M. P. Andrews, S. C. O'Brien, Gas-Phase "Molecular Alloys" of Bulk Immiscible Elements: Fe, Ag, J. Phys. Chem., 96, 1992, 8233-8241.
[5] N. Bahlawane, P. A. Premkumar, Nickel and Nickel-Based Nanoalloy Thin Films from Alcohol-Assisted Chemical Vapor Deposition, Chem. Mater., 22, 2010, 92–100.
[6] H. Gleiter, Nanostructured materials: basic concept and microstrucre, Acta Mater., 48, 2001, 1-29.
[7] H. Gletier, nano-structured materials: state of the art and perspective, Nano-structured Materials, 6, 1995, 3-14.
[8] Y. T. Cheng, R. Hills, Silver- Nickel nanocomposite coating for terminal separable electrical connectors, Unite State Patent, 5679471, Oct. 21, 1997.
[9] O. Loffler, W. Niessner, Silver- Nickel composite materials for electrical contacts and electrodes, Unite State Patent 5500304, Feb.23, 1995.
[10] A. M. Molenbroek, J. K. Nørskov, Structure and Reactivity of Ni-Au Nanoparticle Catalysts, J. Phys. Chem. B, 105, 2001, 5450-5458.
[11] Y. Yamauchi, S. Sadasivan, Synthesis and characterization of mesoporous Pt–Ni (HI–Pt/Ni) alloy particles prepared from lyotropic liquid crystalline media, J. Mater. Chem., 16, 2006, 2229–2234.
[12] A. Kumar, C. Damle, Applied Physics Letters, 79, 2001, 3314.
[13] C. C. Lee, Y.Y. Cheng, Synthesis and electromagnetic wave absorption property of Ni–Ag alloy nanoparticles, Journal of Alloys and Compounds, 480, 2009, 674–680.
[14] Z. Zhang, T. M. Nenoff, Room temperature synthesis of thermally immiscible Ag-Ni nanoalloy, 113(4), 2009, 1155-1159.
[15] R.P. Ingen, R.H. Fastenau, Physical Review Letters, 72, 1994, 3116.
[16] R.P. Ingen, R.H. Fastenau, R. H.; J. Appl. Phys., 76, 1994, 1871.
[17] Q.X. Liu, C.X. Wang, Chemical Physics Letters, 382, 2003, 1.
[18] D. Poondi, J. Singh, J. Materials Science, 35, 2000, 2467.
[19] C. Che Lee, Y. Yi Cheng, Y.; J. Alloy and compound, 480, 2009, 647
[20] R. Abbschain, L. Abbschain, physical Metallurgy principles, Cengage learning, 2009, 267-268.
[21] M. Singleton, P. Nash, Bulletin of Alloy Phase Diagrams, 8 (2), 1987, 119-120.
[22] M. Schinner, M. Ballauff, Single nanocrystals of platinum prepared by partial dissolution of Au-Pt nanoalloys, Science, 323, 2009, 617.
[23] S. C. Tjong, H. Chen, Material Science and Engineering R, 45, 2004,1.
[24] D. Kamenski, N. V. Kulkova, A study of chloride moderated silver catalyst, React. Kinet. Catal. Lett., 7(4), 1997, 481-485.
[25] D. H. Chen, S.H. Wu, Chem. Mat., 12, 2000, 1354.

[26] D. H.Chen, C.H. Hshieh, J. Mat. Chem., 12, 2002, 2412.
[27] P.K. Khanna, P.V. More, Effect of reducing agent on the synthesis of nickel nanoparticles Materials letter, 63(16), 2009, 1384-1386.
[28] Y. Hou, H. Kondoh, Applied Surface Science, 241, 2005, 218.
[29] M. Gaurdry, E. Cottencin, J. Physical Review B, 67, 2003, 155409.
[30] E. Cottancin, G. Celep, Theor. Chem. Acc., 116, 2006, 514.
[31] D.B. William, C.B. Carter, 'Transmission electron microscopy IV', Springer, 1996.
[32] T. Goringe, 'Transmission electron microscope of materials', Wiely Interscience, 1979.
[33] W.D. Pyrz,D.J. Buttrey, Langmuir, 24, 2008, 11350.
[34] Y. Sun, Y. Xia, Shape-Controlled Synthesis of Gold and Silver Nanoparticles, Science, 298, 2002, 2176-2179.
[35] S. Iijima, P.M. Ajayan, J. Appl. Phys, 70, 1991, 5138.

Chapter 6

Discussion, Conclusion and Future Works:

The properties of alloy nanoparticles (ANPs) are strongly dependent on their structures and types of configurations which can be influenced by intrinsic elemental properties (i.e. atomic size, surface energy and etc.) and process driven characteristics of alloy constituents (i.e. cluster size, shape, composition, and etc.). However, specific characteristic that plays a key role in the types of structure ANPs has not yet been fully explored and discussed in the past studies.

Physical, chemical and combined physical-chemical methods similar to those used to synthesize monometallic systems can be used to generate ANPs, but the successful and controlled formation of alloys versus segregated or isolated monometallic structures remains as a challenge. The other challenge is in the characterization of ANPs. Fifty years after Feynman's famous speech, great progress has been made towards the invention of novel instruments such as the scanning tunneling (STEM) and atomic force microscopy (AFM) to manipulate nanostructures, but the full elucidation of the structure-composition-morphology relationships in nanostrcutures like the ANPs and their evolution with temperature are still far from trivial. In the current thesis, the main focus has been on the synthesis and characterization of two component alloy nanoparticles (ANPs).

Au-Sn alloy NPs were synthesized with the chemical reduction methods as lead free solders which are particularly suitable for high temperature electronics, offering superior thermal and mechanical properties. Co-reduction method led to the formation of Au-Sn

ANPs with significant reduction in melting temperature. Also it was found that in the absence of ligands, which are used to cap the nanoparticles to control aggregation, component Sn diffused more into the crystalline structure of Au; therefore the resultant alloy had higher Sn content. Furthermore, a two step successive reduction for the synthesis of Au-Sn was found to be more reliable and reproducible, giving higher Sn content alloys with even lower melting points.

In addition, in this thesis thermally immiscible Ag-Ni ANPs were synthesized at room temperature and their structural stability was studied. In the alloying process, ligands play an important role: ligands with shorter lengths may lead to less perturbation in the alloying process and thus Ni diffuses more in the crystal structure of Ag. Polyvinyl alcohol (PVA) (with shorter length) leads the alloy system to the formation of particles with higher content of Ni. In the presence of sodium citrate, mixture of Ag, Ag_2O_2 NPs and Ag-Ni ANPs is formed and without ligands, the yield of the system is improved up to 100%, but the system remains unstable. An interesting question that should be addressed in the future is what should be the optimum time when the ligands can be added after the co-reduction of both Ag and Ni to prevent them from aggregating. Ag-Ni ANPs were also annealed at 125°C to study the stability of ANPs and the system led to aggregated structures and electron diffraction from these particles confirms the formation of $Ag_{0.5}Ni_{0.5}$ APNs with cubic structure.

Nanoscale phase diagrams are less studied due to several factors that are difficult to determine and take into account, for example the surface energy (compared to the free energy of the system, it is negligible for bulk), temperature, size and shape of ANPs. Development of phase these diagrams can lead to better design of nanostructures. The

alloying process at the nanoscale is quite different from bulk and parameters such as atomic size and crystal structure have less effect on the formation of alloyed nanostructures. The alloying process at nanosclae is generally a kinetically driven mechanism due to significant increase in the diffusion coefficient of components. The alloying process itself at the nanoscale may be monitored by in situ TEM studies at high temperatures, similar to the bulk, and based on that one can develop alloying mechanisms as a function of temperature etc. This is however challenging as the exact compositions (number of atoms and chemical nature) are difficult to precisely determine when particle sizes are small. Chemical methods are scalable and other parameters such as the interaction of ANPs with the solvent and surfactant need to be investigated, because of their effect on surface energy.